1-1-2015

Rapid Scan Electron Paramagnetic Resonance (EPR) and Digital EPR Development

Zhelin Yu
University of Denver

RAPID SCAN ELECTRON PARAMAGNETIC RESONANCE (EPR) AND DIGITAL EPR DEVELOPMENT

_____

A Dissertation

Presented to

the Faculty of Natural Sciences and Mathematics

University of Denver

_____

In Partial Fulfillment

Of the Requirements for the Degree

Doctor of Philosophy

_____

by

Zhelin Yu

August 2015

Advisor: Sandra S. Eaton

Author: Zhelin Yu
Title: RAPID SCAN ELECTRON PARAMAGNETIC RESONANCE (EPR) AND DIGITAL EPR DEVELOPMENT
Advisor: Sandra S. Eaton
Degree Date: August 2015

ABSTRACT

Rapid scan electron paramagnetic resonance (EPR) was developed in the Eaton laboratory at the University of Denver. Applications of rapid scan to wider spectra, such as for immobilized nitroxides, spin-labeled proteins, irradiated tooth and fingernail samples were demonstrated in this dissertation. The scan width has been increased from 55 G to 160 G. The signal to noise (*S/N*) improvement for slowly tumbling spin-labeled protein samples that is provided by rapid scan EPR will be highly advantageous for biophysical studies. With substantial improvement in *S/N* by rapid scan, the dose estimation for irradiated tooth enamels became more reliable than the traditional continuous wave (CW) EPR.

An alternate approach of rapid scan, called field-stepped direct detection EPR, was developed to reconstruct wider EPR signals. A Mn^{2+} containing crystal was measured by field-stepped direct detection EPR, which had a spectrum more than 6000 G wide. Since the field-stepped direct detection extends the advantages of rapid scan to much wider scan ranges, this methodology has a great potential to replace the traditional CW EPR.

With recent advances in digital electronics, a digital rapid scan spectrometer was built based on an arbitrary waveform generator (AWG), which can excite spins and detect EPR signals with a fully digital system. A near-baseband detection method was used to

acquire the in-phase and quadrature signals in one physical channel. The signal was analyzed digitally to generate ideally orthogonal quadrature signals.

A multiharmonic algorithm was developed that employed harmonics of the modulation frequencies acquired in the spectrometer transient mode. It was applied for signals with complicated lineshapes, and can simplify the selection of modulation amplitude.

A digital saturation recovery system based on an AWG was built at X-band (9.6 GHz). To demonstrate performance of the system, the spin-lattice relaxation time of a fused quartz rod was measured at room temperature with fully digital excitation and detection.

ACKNOWLEDGMENTS

I would like to thank my advisors, Professors Gareth and Sandra Eaton for their help and guidance in pursuing my doctorate in their lab. They are great mentors, who show me what true scientists are. It is a privilege to learn from their research and attitude to science.

The digital rapid scan and multiharmonic EPR described in this dissertation was in collaboration with Dr. Mark Tseitlin, a former research faculty member in the Eaton laboratory at University of Denver and now a faculty member in West Virginia University. His support throughout this process has been vital and is greatly appreciated.

The engineers in the Eaton laboratory, Richard Quine and Dr. George Rinard, deserve special thanks for their help with rapid scan EPR and digital EPR developments.

I would also like to thank Dr. Hanan Elajaili and Tengzhi Liu for their help in the relaxation measurements of immobilized nitroxide and measurements of irradiated teeth. I also had a great experience in collaboration with them in the field-stepped direct detection project.

Finally I would like to thank my family and friends for all their support and understanding throughout my graduate career. In particular, I need to thank my girlfriend, Jiangyue Miao. Without her support, none of this would have been possible.

The National Institutes of Health (NIH) and National Science Foundation (NIH) provided funding to Professors Gareth and Sandra Eaton for the work described in this dissertation. A fellowship from the Dean office of Natural Sciences and Mathematics school at University of Denver was provided to support my first year in graduate school.

TABLE OF CONTENTS

LIST OF TABLES

LIST OF FIGURES

LIST OF ABBREVATION

ΔB_{pp}	peak-to-peak linewidth
AWG	arbitrary waveform generator
B_0	main magnetic field
B_1	amplitude of applied magnetic field from microwave source
BDPA	1:1 α,γ-bisdi-phenylene-β-phenylallyl radical:benzene
CW	continuous waveform
dB	decibel
D.C.	direct current
EPR	electron paramagnetic resonance
FID	free induction decay
G	Gauss, magnetic field unit, 1 G =10^{-4} T=0.1 mT
I.D.	inner diameter
IF	intermediate frequency
LiPc	lithium phthalocyanine
LPF	low pass filter
MIS	mechanical-induced signal
NMR	nuclear magnetic resonance
^{15}N-mHCTPO	4-hydro-3-carbamoyl-2,2,5,5-tetra-perdeuteromethyl-pyrrolin-1-^{15}N-oxyl-d_{12}
^{14}N-PDT	perdeuterated 4-oxo-2,2,6,6-tetramethyl-piperidinyl-N-oxyl
^{15}N-PDT	perdeuterated 4-oxo-2,2,6,6-tetramethylpiperidinyl-^{15}N-oxyl

O.D.	outer diameter
OX63	Tris[8-carboxyl-2,2,6,6-benzo(1,2-d:5-d)-bis(1,3)dithiole-4-yl] methyl sodium salt
Q	quality factor of resonator
RIS	radiation-induced signal
RMS	root mean square
S/N	signal-to-noise ratio
SAP	superabsorbent polymer
SPU	signal processing unit
T_1	spin-lattice relaxation time
T_2	spin-spin relaxation time
T_2^*	time constant of damping of FID
tempone	4-oxo-2,2,6,6-tetramethylpiperidinyl-N-oxyl

CHAPTER 1

INTRODUCTION

1.1 Electron paramagnetic resonance

1.1.1 Principle of Electron paramagnetic resonance

Electron paramagnetic resonance (EPR) is a spectroscopic method for studies of paramagnetic species, such as organic free radicals, transition metal complexes that have unpaired electrons, and paramagnetic species in biological materials. EPR is also called electron spin resonance (ESR) or electron magnetic resonance (EMR). EPR measures the absorption of electromagnetic radiation by a sample with unpaired electron spins. The first observation of an electron paramagnetic resonance signal by Zavoisky in 1944 was a radio frequency absorption spectrum obtained from a $CuCl_2 \cdot 2H_2O$ sample (Zavoisky 1944, Zavoisky 1946)

For the case of a sample with one unpaired electron, the electron spin states can have the quantum numbers, m_s, equal to either +1/2 or -1/2. According to the Boltzmann distribution at room temperature, slightly more spins are in the -1/2 spin state (low energy state). The energy difference between the spin states, which is known as the Zeeman splitting (Weil and Bolton 2007), is proportional to the external magnetic field (B_0),

$$\Delta E = g\beta B_0 \tag{1.1}$$

where g is the g-factor of the electron, and β is the Bohr magneton. The dependence of the Zeeman splitting on the external magnetic field is shown in Fig. 1.1.

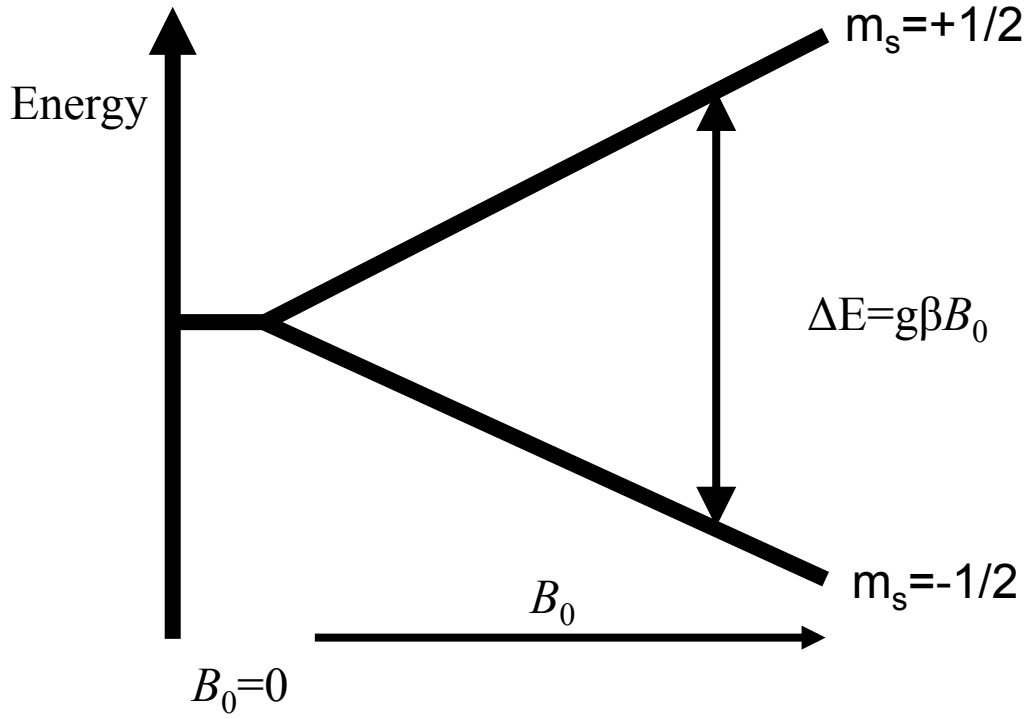

Fig. 1.1 Zeeman splitting of the energy levels of an unpaired electron in a magnetic field.

The energy separation, ΔE, is linearly proportional to the magnetic field, B_0. Continuous wave (CW) EPR is usually performed by sweeping the magnetic field at a constant microwave frequency, ν. The transitions will occur between the Zeeman levels under the following condition,

$$h\nu = g\beta B_0 \qquad (1.2)$$

where Planck constant, $h = 6.626 \times 10^{-34}$ J·s, $\beta = 9.274\times10^{-24} J\cdot T^{-1}$, for a free electron in vacuum, $g_e = 2.0023$.

1.1.2 CW EPR

The most common CW EPR spectrometers use from 9.0 to 10 GHz microwaves (in the X-band), for which the free-electron resonance occurs at about 3200 to 3500 G. In a CW EPR experiment, the microwave frequency is kept constant and the magnetic field is scanned through the resonance field region. The EPR signal is obtained by measuring the net absorption (absorption – emission) of microwave energy by the sample. Since the net absorption of energy by the sample would change the microwave energy of the standing wave pattern in the resonator, it modifies the match between the resonator and the waveguide and changes the amount of microwave energy reflected back from the resonator to the detector (Eaton, Eaton et al. 2010).

1.1.2.1 Field modulation and phase sensitive detection

The field modulation and phase sensitive detection were developed to improve the poor signal to noise ratio (*S/N*) and background instabilities. In a CW EPR spectrometer, the microwaves are generated by a source and split into two arms, one goes to the sample in the resonator (signal arm) and the other performs as a reference (reference arm). Modulation coils in the resonator generate the field modulation. The microwaves in the signal arm go to the resonator and are reflected back along with the modulated signal. The signal arm and the reference arm are mixed and only the components of modulated signal that have a particular phase relative to the reference arm are detected by the phase sensitive detector.

The detected linewidth in the EPR spectrum is quite sensitive to the field modulation amplitude. When the field modulation amplitude is more than about 20% of the peak to peak linewidth (ΔB_{pp}) of the EPR signal, it will significantly broaden and distort the lineshape (Eaton, Eaton et al. 2010). In order to obtain accurate EPR lineshape without linewidth broadening in CW EPR, the modulation amplitude for the CW EPR in this dissertation is always selected as 20 % of ΔB_{pp} of the narrowest line in a spectrum.

1.1.2.2 Microwave power selection and power saturation in CW EPR

The applied microwave power in CW EPR is another important parameter that determines the *S/N* of CW spectra and the EPR lineshape (Weil and Bolton 2007, Eaton, Eaton et al. 2010). Since most EPR signals could be saturated with available power in a commercial spectrometer, the progressive power study that measures the EPR signal at different power levels is needed. The microwave magnet field, B_1, is propotional to the square root of microwave power. In principle, if there is no power saturation, the EPR signal will increase linearly with B_1. The efficiency of the resonator to actually convert microwave power to B_1 is an important factor and can vary widely between different resonator designs. In order to have a non-distorted EPR lineshape with the strongest signal, the optimized power selection is the maximum B_1 in the linear region of the power saturation plot. An example is shown in Fig.1.2.

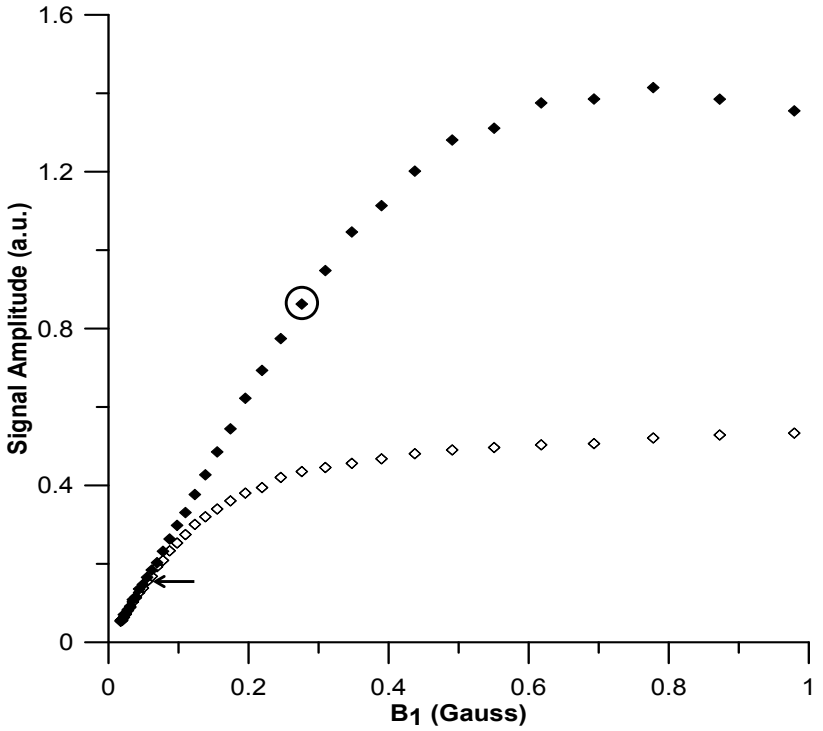

Fig.1.2 Power saturation plot of an irradiated tooth enamel sample obtained by conventional CW (◇) or rapid scan (◆). The selected powers the CW and rapid scan spectra are indicated with an arrow or circle, respectively. Spectra and data reproduced from the original journal article (Yu, Romanyukha et al. 2015).

1.1.3 Concepts of electron spin relaxation time

Since the relaxation time in EPR is not the focus of this dissertation, the concepts of the spin relaxation time are only discussed briefly and more details can be found in references (Hustedt and Beth 2000, Schweiger and Jeschke 2001, Weil and Bolton 2007, Eaton, Eaton et al. 2010) The relaxation process is the return of a perturbed system back to the equilibrium status. The relaxation time is the time constant of the relaxation. When the spin system is heated up by the absorption of microwave in the magnetic field, the

population in energy states split by Zeeman effect is no longer following Boltzmann distribution. The time constant as the spin system returns to the thermal equilibrium is called spin-lattice relaxation time, T_1. If there is a net transverse magnetization of spin introduced by the absorption of microwave in a magnetic field, the time constant for return to equilibrium is called the spin-spin relaxation time, T_2. The time constant, which is associated with all broadening mechanisms that contribute to the linewidth, is T_2^*. It can be measured as the time constant of the damping of the free induction decay (FID) of the spin system response to a microwave pulse.

1.2 Rapid scan EPR

1.2.1 Principle of rapid scan EPR

Rapid Scan EPR is analogous to the prior work in NMR. Bloembergen, Purcell, and Pound first observed a transient NMR effect after the magnetic field passed through resonance (Bloembergen, Purcell et al. 1948). The first observation of transient effects in EPR was by Beeler (Beeler, Roux et al. 1955, Beeler, Roux et al. 1956). The rapid scan NMR was developed in the 1970s (Dadok and Sprecher 1974, Gupta, Ferretti et al. 1974). The transient response from linear rapid scan NMR can be deconvolved to recover the slow scan absorption spectrum.

In rapid scan EPR, the magnetic field is scanned through the signal in times that are short relative to the electron spin relaxation times (Eaton, Quine et al. 2014). The directly detected quadrature signal is obtained using a double-balanced mixer with the reference at the resonance frequency. By contrast, conventional CW EPR uses phase

sensitive detection at the modulation frequency (Eaton, Quine et al. 2014). Deconvolution of the rapid scan signal gives the absorption spectrum. Rapid scan EPR has been shown to yield improved *S/N* per unit time relative to CW EPR for rapidly-tumbling nitroxides in fluid solution (Mitchell, Quine et al. 2012), spin-trapped superoxide (Mitchell, Rosen et al. 2013), the E' center in irradiated fused quartz (Mitchell, Quine et al. 2011), amorphous hydrogenated silicon (Mitchell, Tseitlin et al. 2013), N@C_{60} diluted in C_{60} (Mitchell, Tseitlin et al. 2013), and the neutral single substitutional nitrogen centers (N_S^0) in diamond (Mitchell, Tseitlin et al. 2013).

1.2.2 The advantages of rapid scan EPR

The improved *S/N* for rapid scan relative to CW spectra comes from three factors: (i) differences in signal amplitudes due to excitation of a small portion of the spectrum in the CW experiment vs excitation of the entire spectrum in rapid scan, (ii) the ability to use higher B_1 without power saturating the signal, and (iii) the differences in the noise spectral densities in CW and rapid scan spectra (Weger 1960, Eaton, Quine et al. 2014). The details of the application of rapid scan EPR will be discussed in Chapter 2 and 3.

1.2.3 The status of rapid scan EPR at the time I started to work on my dissertation project

The milestone of the beginning of rapid scan EPR technology is back to 2004 (Stoner, Szymanski et al. 2004). With years of hard work by members in the Eaton lab, rapid scan EPR has been used on varied samples at 250 MHz and X-band EPR (Joshi, Ballard et al. 2005, Mitchell, Quine et al. 2012, Mitchell, Rosen et al. 2013, Mitchell,

Tseitlin et al. 2013). The deconvolution procedures to recover the slow scan spectra from the transient data were established for both linear scans (Joshi, Ballard et al. 2005) and sinusoidal scans (Tseitlin, Rinard et al. 2011). The hardware developments to improve the performance of rapid scan technology were applied to rapid scan coils, coil drivers and resonators (Joshi, Eaton et al. 2005, Quine 2008, Quine, Czechowski et al. 2009, Quine, Rinard et al. 2010, Rinard, Quine et al. 2010, Quine, Mitchell et al. 2012). The signal analysis methodologies such as background removal procedures were developed and applied to improve the reliability of rapid scan EPR (Tseitlin, Rinard et al. 2011, Tseitlin, Mitchell et al. 2012, Tseitlin, Eaton et al. 2013).

However, there were still some limitations of rapid scan EPR at the time I started working on my dissertation project. (i) A limited field scan range of rapid scan EPR, 55 G was the largest scan width of rapid scan EPR at X-band reported in published references (Mitchell, Quine et al. 2012, Mitchell, Rosen et al. 2013). For CW EPR at X-band, the spectrum can be scanned more than 6000 G. Therefore, for samples like immobilized nitroxides, spin-labeled proteins, transition metal complex, and other biomaterials, which need to scan more than 55 G magnetic field, the rapid scan could not satisfy the requirement of such experiments. (ii) The rapid scan background introduced by eddy current and mechanic resonance is hard to remove when the higher harmonics components dominate the background. For EPR imaging, the background might be a problem for measurements of low spin concentration samples (Biller, Tseitlin et al. 2014). (iii) It is challenging to make two quadrature channels balanced perfectly for the sinusoidal deconvolution procedure (Tseitlin, Rinard et al. 2011) of rapid scan.

1.2.4 My contribution to the rapid scan EPR and digital EPR

To expand the application of rapid scan EPR, a wider field scan range is needed. In close collaboration with two engineers, George Rinard and Richard Quine in the Eaton lab, a set of scan coils was constructed from 200 turns of Litz wire and the coil constant was 37.7 G/A, which is sufficient to generate scans up to 155 G wide with scan frequencies up to 13.4 kHz (Yu, Quine et al. 2014). By mounting the coils on the magnet, rather than on the resonator, the oscillatory background signal induced by the rapid scans was reduced significantly (Yu, Quine et al. 2014, Yu, Romanyukha et al. 2015). Samples with broad EPR signals, like immobilized PDT nitroxides, spin-labeled T4 lysozyme, and irradiated tooth enamels and fingernails, could be measured by rapid scan and showed significant improvements comparing to traditional CW EPR (Yu, Quine et al. 2014, Yu, Romanyukha et al. 2015). The rapid scan EPR imaging has been done by other members of the Eaton group using the modified scan coils (up to 84 G scan width) for the full spectrum imaging of a spin-trapped hydroxyl radicals (Biller, Tseitlin et al. 2015).

However, improved scan coils do not allow rapid scan measurement of the signals that are broader than 200 G. Field-stepped direct detection EPR, an alternate approach based on rapid scan technology, was developed to solve this problem. With the field-stepped direct detection method, the largest scan width achieved in real life experiments is 6200 G at X-band, which is similar to the wide sweeps available in CW EPR at X-band (Yu, Liu et al. 2015). Since the scan width is relatively small for each segment, the background signal in field-stepped direct detection is smaller than in rapid scan can be

corrected and removed by polynomial baseline correction. This method extends the advantages of rapid scan to much wider sweeps than are feasible for a single scan and give rapid scan the potential to replace the traditional CW technique.

Recent advances in digital electrics make it possible to build EPR spectrometers with digital source and detection, which can provide greater flexibility in experimental design and operating frequency than current generation spectrometers. A prototype digital EPR spectrometer (Tseitlin, Yu et al. 2014) was developed by the author in close collaboration with Mark Tseitlin. Both real and imaginary rapid scan EPR signals are reconstructed from a single physical channel to produce an ideal quadrature signal.

The dissertation is discussed with the following topics. Chapter 2 is the application of rapid scan EPR in immobilized nitroxide radicals and spin-labeled protein. Chapter 3 is the application of rapid scan EPR in solid-state dosimetry. The radiation-induced signals of tooth enamels and fingernails are discussed and compared with CW EPR. Chapter 4 is field-stepped direct detection EPR, which is the alternate approach of rapid scan to extend the advantages of rapid scan to much wider scan. Chapter 5 is digitally generated excitation and near-baseband quadrature detection of rapid scan EPR signals. The application of an arbitrary waveform generator (AWG) in EPR is discussed. A prototype spectrometer was built to utilize an AWG for digital signal excitation and detection. Chapter 6 is multiharmonic EPR for extend samples with both narrow and broad lines. An extended application of multiharmonic EPR originally developed by Mark Tseitlin (Tseitlin, Eaton et al. 2011) is discussed to show the capability of the multiharmonic algorithm for signals with more complicated lineshapes. Chapter 7 is the

development of digital saturation recovery spectrometer. A recently developed prototype AWG-based digital saturation recovery spectrometer is discussed. Chapter 8 is the summary of my dissertation and comments on the future work.

CHAPTER 2

RAPID SCAN EPR OF IMMOBILIZED NITROXIDE

2.1 Introduction

In rapid-scan EPR the magnetic field is scanned through resonance in a time that is short relative to the electron spin relaxation times (Eaton, Quine et al. 2014). The directly detected quadrature signal is obtained using a double-balanced mixer with the reference at the resonance frequency. By contrast, conventional CW EPR uses phase sensitive detection at the modulation frequency (Eaton, Quine et al. 2014). Deconvolution of the rapid-scan signal gives the absorption spectrum. Rapid-scan EPR has been shown to yield improved *S/N* per unit time relative to CW EPR. With the exception of the piece-wise acquisition of the Hyde lab (Hyde, Bennett et al. 2013), the widest rapid-scan spectra prior to the work reported in our paper (Yu, Quine et al. 2014) were the 55 G scans of spin-trapped superoxide at X-band (Mitchell, Rosen et al. 2013). Among organic radicals, one very important case is immobilized nitroxide spin labels. The results demonstrate that the technology developed in the Eaton laboratory for rapid scans can be extended to perform 155 G wide sinusoidal scans, which are wide enough to encompass the full spectrum of an immobilized nitroxide (Yu, Quine et al. 2014).

Rapid scans were obtained for ^{14}N-perdeuterated tempone (^{14}N-PDT) and ^{15}N-PDT in sucrose octaacetate and for T4 lysozyme spin labeled at positions 61 and 135 with iodoacetamide spiro cyclohexyl nitroxide **2** in a trehalose glass (Scheme 2.1). The *S/N* for the rapid-scan spectra of the immobilized nitroxides is about an order of magnitude greater than for CW spectra of the same samples.

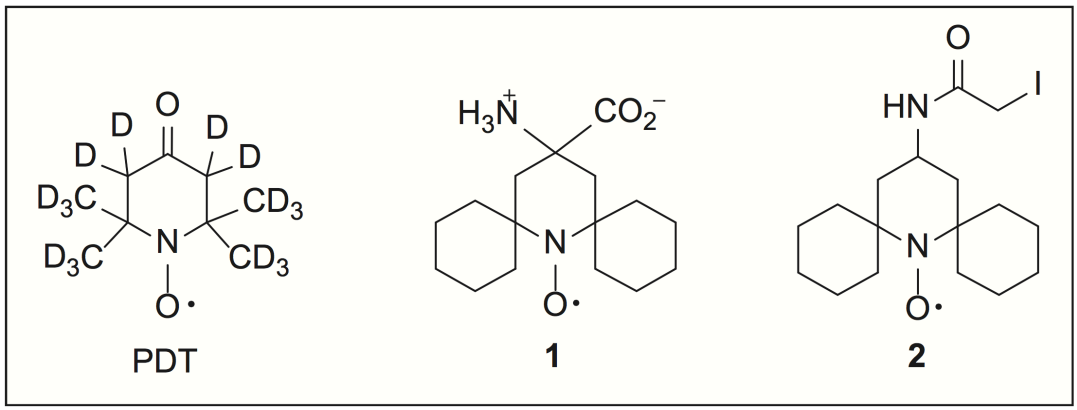

Scheme 2.1 Structure of ^{14}N-perdeuterated tempone (^{14}N-PDT), spirocyclohexyl amino acid nitroxide **1**, and iodoacetamide spiro-cyclohexyl nitroxide **2**

2.2 Methods

2.2.1 Sample preparation

Nitroxides ^{14}N-PDT (perdeuterated 4-oxo-2,2,6,6-tetramethyl-piperidinyl-N-oxyl) and ^{15}N-PDT (perdeuterated 4-oxo-2,2,6,6-tetramethylpiperidinyl-^{15}N-oxyl) were purchased from CDN isotopes (Quebec, Canada), and used as received. Solid ^{14}N-PDT or ^{15}N-PDT and sucrose octaacetate were mixed in ratios that would result in 0.50 mM or 0.050 mM solutions, respectively. The solids were ground gently in a mortar and pestle to mix the two components. The solid mixtures were placed in 4 mm O.D. quartz EPR

tubes, evacuated for 6 h to remove oxygen, heated gently above the melting point, and cooled to form glasses (Sato, Kathirvelu et al. 2007). Tubes were flame sealed. The concentrations of PDT in the samples were determined by comparison of the double integrated intensities with that for a standard sample of 0.56 mM tempone (4-oxo-2,2,6,6-tetramethylpiperidinyl-N-oxyl) in toluene. The final concentrations of radical in the samples were 0.15 mM ^{14}N-PDT and 0.018 mM ^{15}N-PDT, and the numbers of spins in these samples were 2.3×10^{15} and 2.8×10^{14}, respectively. These concentrations are lower than in the initial mixtures due to losses during the evacuation and heating steps. Spirocyclohexyl amino acid nitroxide **1** was prepared at University of Nebraska as previously reported (Rajca, Kathirvelu et al. 2010) and dissolved in 1:1 water:glycerol for relaxation time measurements. Iodoacetamide spirocyclohexyl spin label **2** was prepared at the University of Nebraska. The preparation of the spin-labeled T4 lysozyme was performed at Vanderbilt University (Meyer, Swanson et al. 2015) and the sample immobilized in trehalose was prepared by Virginia Meyer (Meyer, Swanson et al. 2015). The solution of spin-labeled protein and a 10-fold excess of hen egg white lysozyme was mixed with 0.2 M trehalose in water, then spread on a watch glass and allowed to air dry in the dark for 48 h before drying in vacuum for 6 h. There were 1.4×10^{16} spins in the T4 lysozyme sample.

Electron spin relaxation times for the samples studied in this chapter were measured by Hanan Elajaili and reported in her dissertation and in the published paper (Yu, Quine et al. 2014).

2.2.2 EPR spectroscopy

CW and rapid-scan spectra were recorded on a Bruker E500T using a Bruker Flexline ER4118X-MD5 dielectric resonator, which excites spins over a sample height of about 1 cm (Mitchell, Quine et al. 2012, Mitchell, Tseitlin et al. 2013). Sample heights of about 4 mm were used to ensure uniform B_1 and scan field along the sample. The resonator Q is ~9000 for these nonlossy samples. The rapid-scan signals were recorded with a Bruker SpecJetII fast digitizer. The quadrature detection channels were calibrated with a small sample of the solid BDPA (1:1 α,γ-bisdi-phenylene-β-phenylallyl:benzene) radical. Deconvolution and background removal procedures require that the phase difference between the two quadrature channels is close to 90°. Kronig-Kramers transformation of one channel and comparison with the other showed that the phase difference deviated from 90° by 7°. The phase difference between the two channels was corrected to 90° in the post-processing of the rapid-scan signals. The sinusoidal scans were generated with the recently described scan driver (Quine, Mitchell et al. 2012). The scan coils were constructed from 200 turns of Litz wire (255 strands of AWG44 wire). The coils have about 7.6 cm average diameters and were placed about 4 cm apart. The coil constant was 37.7 G/A, which is sufficient to generate scans up to 155 G wide with scan frequencies up to 13.4 kHz (Quine, Mitchell et al. 2012). Mounting the coils on the magnet, rather than on the resonator, reduces the oscillatory background signal induced by the rapid scans. The placement of highly conducting aluminum plates on the poles of the Bruker 10" magnet reduces resistive losses in the magnet pole faces that arise from induced currents. The dielectric resonator decreases eddy currents induced by the rapidly

changing magnetic fields relative to resonators with larger amounts of metal. Data were acquired in blocks of 2–3 sinusoidal cycles. Scans are labeled with the rate in the center of the scan, which is $\pi f_S B_m$ G s^{-1} where f_S is the scan frequency and B_m is the scan width.

To select the incident microwave powers for the CW and rapid scan experiments, power saturation curves were examined (Fig. 2.1). The amplitudes of CW spectra and rapid scan signals were measured as a function of microwave power. The incident powers were converted to B_1 using the known resonator efficiency of about 3.8 $G/W^{1/2}$ at Q of 9000 (Mitchell, Tseitlin et al. 2013). For signal-to-noise calculations rapid scan signals were deconvolved into EPR absorption spectra and processed as described in (Tseitlin, Rinard et al. 2011, Tseitlin, Mitchell et al. 2012). Figs. 2.2–2.4 compare CW and rapid scan spectra measured at powers optimized for each measurement.

The power selection was done using the following criterion. A linear least-squares fit through the point 0,0 and the signal amplitudes at the lowest 5 or 6 microwave powers was extrapolated to higher B_1. The B_1 selected for data acquisition was the point at which the experimental signal amplitude was about 5% lower than the amplitude predicted by linear extrapolation of the non-saturated signal amplitude. The modulation frequency for the CW spectra was 100 kHz. The modulation amplitudes: ^{14}N-PDT in sucrose octaacetate (0.63 G), ^{15}N-PDT in sucrose octaacetate (0.9 G), ^{14}N-spin label on T4 lysozyme (1.8 G), were about 20% of ΔB_{pp}. These combinations of parameters result in less than 2% line broadening relative to spectra obtained at lower modulation amplitude and smaller B_1.

The scan modulation frequencies for the rapid scan signals were limited by the constraints of the coil driver. At these scan frequencies the signal bandwidths were less than the resonator bandwidth (Eaton, Quine et al. 2014) so resonator bandwidth did not contribute to spectral broadening.

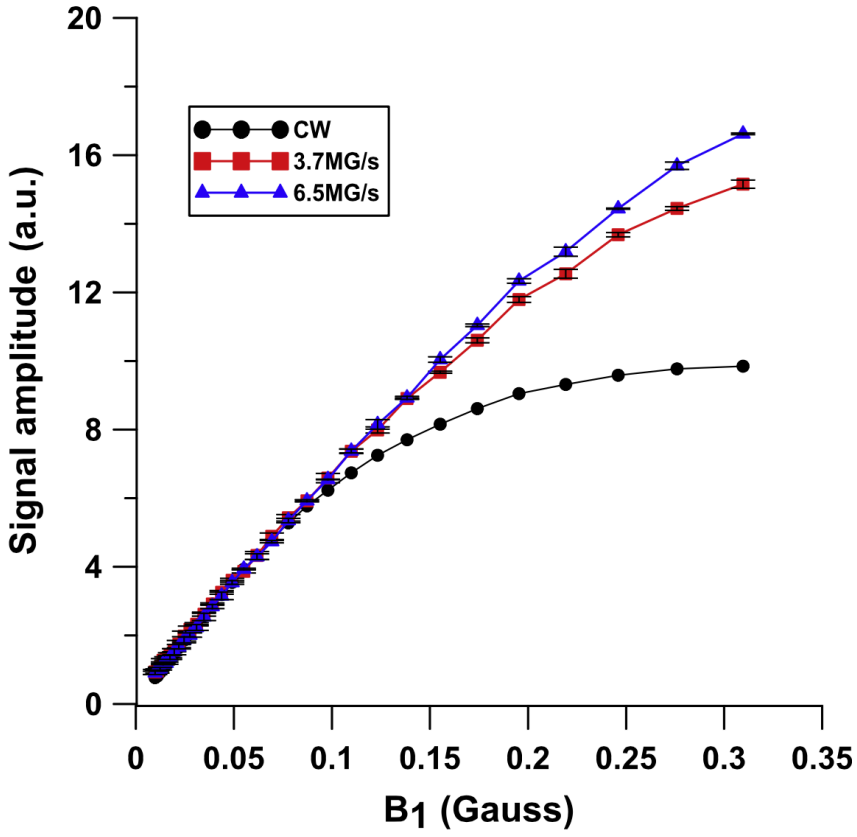

Fig. 2.1 Power saturation curves at the peak of the absorption (rapid scan) and first derivative (CW) spectra of 0.15 mM ^{14}N-PDT in sucrose octaacetate at 293 K. The scan widths were 155 G and rapid-scan frequencies were 7.7 or 13.4 kHz. The amplitude of the CW spectra is scaled to match that obtained for the rapid scans at low B_1. Plot and data reproduced from the original journal article (Yu, Quine et al. 2014).

The data acquisition times were about 10 s. The estimates of 10 s acquisition times were based on the following calculations, which are consistent with the relatively small overhead in the software. For CW spectra the acquisition time is the conversion time per point multiplied by the number of field steps. For rapid scans the acquisition time is ($1/f_S$) multiplied by the product of number of scan cycles combined in the deconvolution software and the number of scans averaged.

2.2.3 Signal processing

The rapid-scan signals were deconvolved and background corrected (Tseitlin, Rinard et al. 2011, Tseitlin, Mitchell et al. 2012). The resulting spectra are the sum of up-field and down-field scans for the absorption and dispersion signals. The experimental dispersion spectra were converted into absorption spectra for summation with the experimental absorption spectra (Tseitlin, Quine et al. 2010). A post-processing Gaussian filter was applied to both CW and rapid-scan spectra. The cut-off frequency for the low-pass filter was selected to cause no more than 2% broadening of the full width at half maximum of the absorption spectra or the ΔB_{pp} linewidth for first-derivative spectra. The bandwidth of the first derivative spectrum is larger than for the absorption spectrum of the same signal (Tseitlin, Eaton et al. 2012). The first derivative spectrum was therefore calculated by numerical differentiation of the deconvolved rapid-scan spectrum before low-pass filtering, with subsequent application of low-pass filtering. *S/N* is the peak-to-peak signal amplitude (for CW) or signal amplitude (for rapid scan) divided by RMS noise in baseline regions of the spectrum.

2.3 Results and discussion

Sucrose octaacetate and trehalose form glasses at ambient temperatures. The EPR lineshapes for ^{14}N-PDT in sucrose octaacetate (Fig. 2.2), ^{15}N-PDT in sucrose octaacetate (Fig. 2.3), and for T4 lysozyme spin labeled with **2** in trehalose (Fig. 2.4) are consistent with immobilized nitroxides with $\tau_R > 10^4$ ps (Freed 1976). The spectra shown in Figs. 2.2-2.4 were obtained with ~10 s acquisition time, except for the CW spectrum of ^{15}N-PDT in sucrose acetate which was obtained with 5 min acquisition because of the low *S/N*.

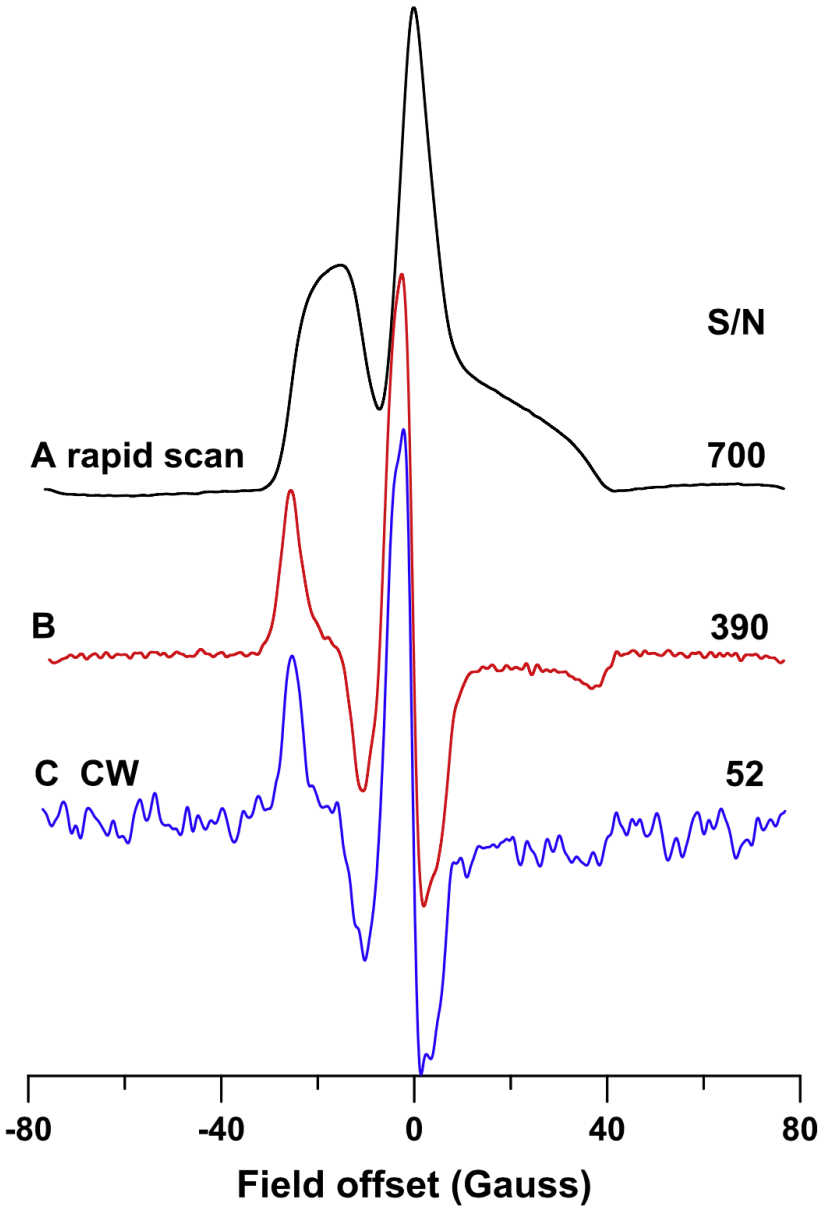

Fig. 2.2 CW and rapid-scan spectra of 0.15 mM ^{14}N-PDT in sucrose octaacetate at 293 K obtained with 10 s acquisition time. (A) Absorption spectrum obtained by rapid scan with the parameters listed in Table 2.1, (B) first derivative spectrum obtained from (A) by numerical differentiation, and (C) field-modulated CW spectrum obtained with 100 kHz and 0.63 G modulation amplitude, which is 20% of ΔB_{pp} = 3.2 G. Spectra and data reproduced from the original journal article (Yu, Quine et al. 2014).

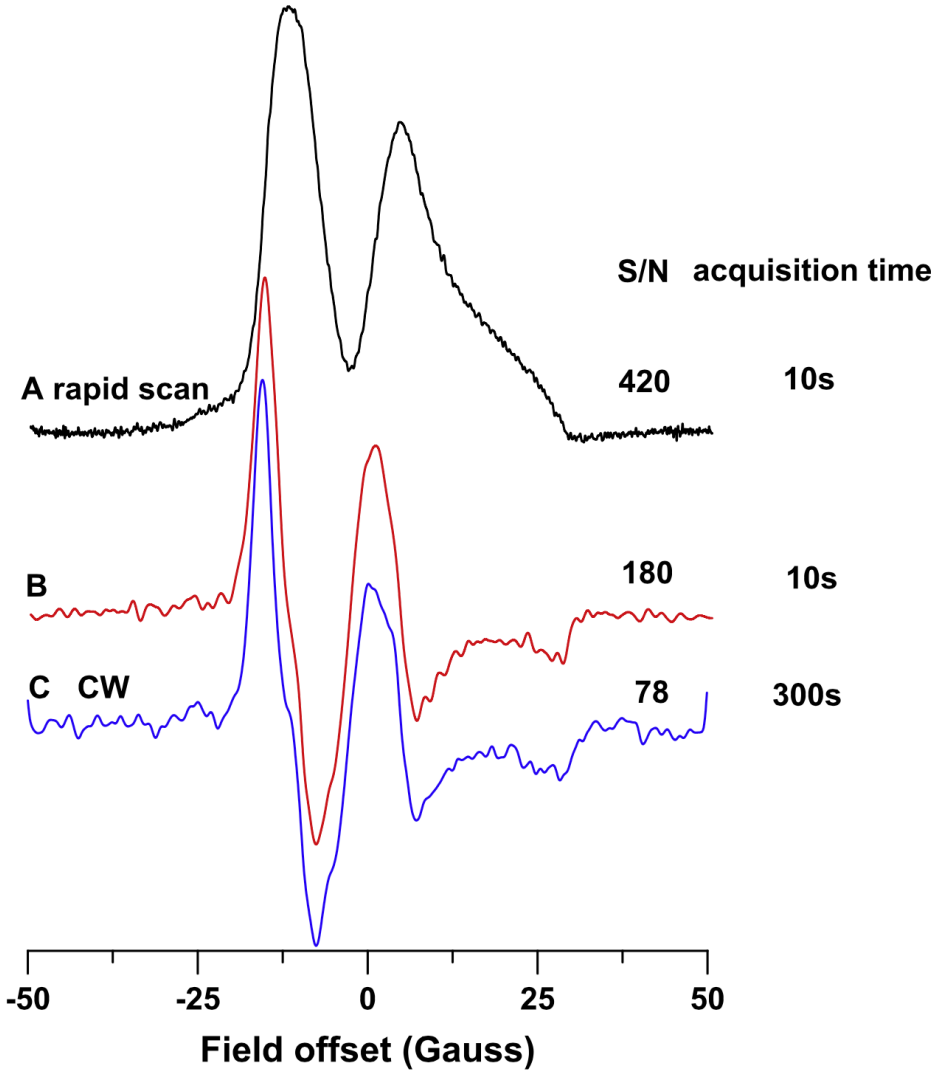

Fig. 2.3 CW and rapid-scan spectra of 0.018 mM ^{15}N-PDT in sucrose octaacetate at 293 K. (A) Absorption spectrum obtained by rapid scan with the parameters listed in Table 2.1, (B) first derivative obtained from (A) by numerical differentiation, and (C) field-modulated CW spectrum obtained with 100 kHz modulation frequency and 0.9 G modulation amplitude, which is 20% of ΔB_{pp} = 7.23 G. The data acquisition times were 10 s for (A) and 5 min for (C). Spectra and data reproduced from the original journal article (Yu, Quine et al. 2014).

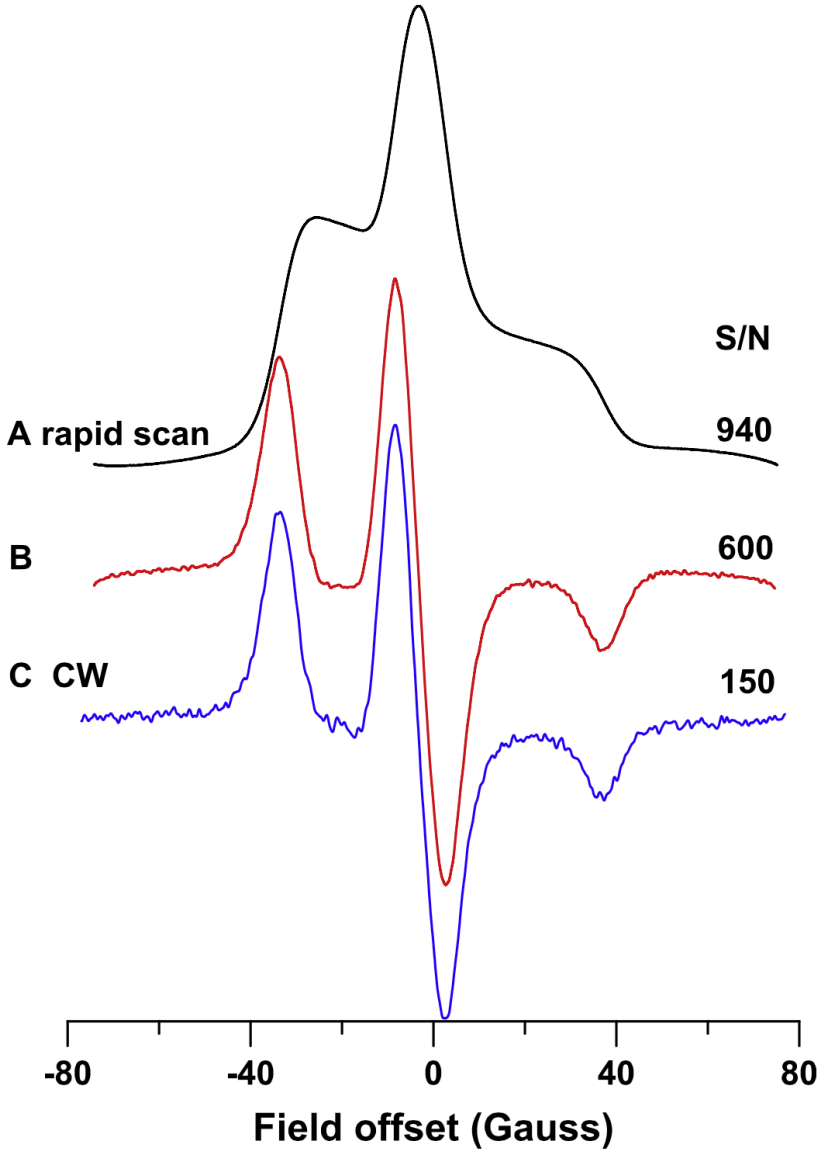

Fig. 2.4 CW and rapid-scan spectra at 293 K of spin label **2** attached to T4 lysozyme obtained with 10 s acquisition times. (A) Absorption spectrum obtained by rapid-scan with the parameters listed in Table 2.1, (B) first derivative obtained from (A) by numerical differentiation, (C) field-modulated CW spectrum obtained with 100 kHz modulation frequency and 1.8G modulation amplitude which is 20% of ΔB_{pp} = 10.6 G. Spectra and data reproduced from the original journal article (Yu, Quine et al. 2014).

2.3.1 Comparison of CW and rapid-scan spectra

The power saturation curves for ^{14}N-PDT (Fig. 2.1) in sucrose octaacetate are typical of the samples studied. The region in which signal amplitude increases linearly with B_1 extends to higher B_1 for the rapid-scan experiments than for CW, which permits use of higher microwave power without saturating the signal. This phenomenon has been observed previously in rapid scans of the E' center in irradiated fused quartz (Mitchell, Quine et al. 2011), nitroxides in fluid solution (Mitchell, Quine et al. 2012), amorphous hydrogenated silicon (Mitchell, Tseitlin et al. 2013), N@C_{60} diluted in C_{60} (Mitchell, Tseitlin et al. 2013), and the neutral single substitutional nitrogen centers (N^0_s) in diamond (Mitchell, Tseitlin et al. 2013). In a rapid scan experiment the spin system is on resonance for a time that is shorter than in conventional CW, so higher B_1 can be used without saturation. The use of higher power (Table 2.1) and resulting increase in signal amplitude is a significant contributor to the improved *S/N* for rapid-scan spectroscopy (Eaton, Quine et al. 2014).

Table 2.1 X-band CW and rapid-scan EPR for ~10 s acquisition time. Table and data reproduced from the original journal article (Yu, Quine et al. 2014).

Sample	Scan frequ-ency (kHz)	Sweep width (G)	Scan rate (MG/s)	B_1 for CW (mG)	B_1 for rapid scan (mG)	*S/N* of CW	*S/N* of rapid scan[a]	*S/N* ratio[b]
0.15 mM ^{14}N-PDT in sucrose octaacetate	13.4	155	6.5	24	49	52	700 (390)	13 (7.5)
0.018 mM ^{15}N-PDT in sucrose octaacetate	20.9	100	6.6	22	39	14[c]	420 (180)	30 (13)
2 on T4 lysozyme	13.4	155	6.5	25	77	150	940 (600)	6 (4)

The bold values designate the structures in the Scheme 2.1

[a] The S/N for the absorption spectrum is shown, followed by the S/N for the first derivative

[b] Ratio of S/N for rapid scan absorption spectrum to that for CW, followed by ratio for first derivatives.

[c] The S/N for 5 min data acquisition time was 78. To correct to a 10 s acquisition time the S/N was divided by the square root of (300 s/10 s).

The *S/N* for the rapid-scan absorption spectra is 6-30 times that for the CW first derivative spectrum (Table 2.1), which is a substantial advantage for weak signals. The *S/N* for the first derivative calculated from the rapid scan absorption spectrum has lower *S/N* than the original absorption spectra. This is due in part to the higher bandwidth of first derivatives, which limits the filtering that can be performed without broadening the spectrum (Tseitlin, Eaton et al. 2012). The improved *S/N* for rapid-scan relative to CW spectra comes from three factors: (i) differences in signal amplitudes due to excitation of a small portion of the spectrum in the CW experiment vs. excitation of the entire

spectrum in rapid scan, (ii) the ability to use higher B_1 without power saturating the signal (Fig. 2.1), and (iii) the differences in the noise spectral densities in CW and rapid-scan spectra (Eaton, Quine et al. 2014). The improvement in *S/N* for rapid scan relative to CW was not as large for the spin-labeled T4 lysozyme sample as for the PDT samples. For the T4 lysozyme the linewidth is large due to the high spin concentration, which permitted use of a higher modulation amplitude and therefore detection of a larger fraction of the signal amplitude than in the CW spectra of the PDT samples, which decreased the relative advantage of rapid scan. In addition, the large linewidths for the T4 lysozyme sample corresponds to a smaller signal bandwidth than for the narrow linewidths of the PDT signals. A higher scan rate for the T4 lysozyme sample would have been consistent with the resonator bandwidth and could have provided further improvement in *S/N*, but was not possible with the current hardware.

2.4 Summary

X-band electron paramagnetic resonance spectra of immobilized nitroxides were obtained by rapid scan at 293 K. Scan widths were 155 G with 13.4 kHz scan frequency for ^{14}N-perdeuterated tempone and for T4 lysozyme doubly spin labeled with an iodoacetamide spirocyclohexyl nitroxide and 100 G with 20.9 kHz scan frequency for ^{15}N-perdeuterated tempone. These wide scans were made possible by modifications to the rapid-scan driver, scan coils made of Litz wire, and the placement of highly conducting aluminum plates on the poles of a Bruker 10" magnet to reduce resistive losses in the magnet pole faces. For the same data acquisition time, the *S/N* for the rapid-scan

absorption spectra was about an order of magnitude higher than for CW first-derivative spectra recorded with modulation amplitudes that do not broaden the lineshapes. The *S/N* improvement for slowly tumbling spin-labeled protein samples that is provided by rapid scan EPR (Fig. 2.4) will be highly advantageous for biophysical studies.

CHAPTER 3

RAPID SCAN EPR OF SOLID STATE DOSIMETRY

3.1. Introduction

To properly handle an emergency medical response or to do radiation epidemiological studies a long time after a radiological event, it is critically important to determine the radiological doses that were received by individuals. Most people do not wear radiation dosimeters; therefore, their radiation doses can be measured only by biodosimetry techniques. An overview of applicability under different scenarios can be found in references (Alexander, Swartz et al. 2007, Simon, Bailiff et al. 2007). Generation of free radicals is a primary effect of radiation exposure and occurs immediately upon radiation. EPR is one of a very few techniques capable of directly measuring free radicals induced by radiation. The signal is not affected by stress, wounds, or medical treatment. These advantages give EPR a unique position as compared to other biodosimetry techniques that require significant time (up to several days) after a radiation event to become applicable. Two types of tissue are known to be suitable for EPR dosimetry: calcified (teeth and bones) and keratin-based (nails and hair) tissue. Tooth enamel has the best EPR dosimetric properties because of the high stability of the radiation-induced signal (RIS). Radiation produces a characteristic long-lasting EPR signal in tooth enamel that has different g values and electron spin relaxation times

than the native signal (Fattibene and Callens 2010). This signal, which is stable for many years, is the basis for retrospective accident dosimetry based on teeth (Fattibene and Callens 2010). During the past decade, EPR dosimetry in teeth has made considerable progress toward becoming a routine dosimetric method for radiation epidemiological studies. An interlaboratory comparison indicated that there are two challenges to the accuracy of dosimetry (i) improving the *S/N* and (ii) reproducibility of sample positioning (Romanyukha and Trompier 2011). The focus of this chapter is on improving *S/N*.

The improvement in *S/N* that can be obtained by rapid scan was demonstrated for the RIS in tooth enamel at X-band (Yu, Romanyukha et al. 2015). Preliminary results are also shown for the RIS in fingernails.

3.2. Methods

3.2.1 Sample Preparation

Sample preparation was done by Alexander Romanyukha at the US Naval Dosimetry Center. Tooth enamel samples were prepared from six human molars collected from the U.S. population (extracted for medical reasons and collected under conditions of anonymity). Tooth enamel was separated from dentin using a low-speed water-cooled dental drill. The pooled tooth enamel from all samples was then washed with distilled water and dried at 40 °C under vacuum for 14 h. The enamel pieces were then crushed with a mortar and pestle and carefully mixed. The tooth enamel powder with 0.12 - 0.50 mm grain size was segregated for the measurements using sieves. The pooled sample obtained by this procedure was split into portions and irradiated to doses

of 0.5 and 10 Gy. Irradiation of tooth enamel samples was done using a calibrated ^{137}Cs source. Tooth enamel samples (60 mg) at each irradiation level were placed in 4 mm O.D. quartz EPR tubes. A 60 mg sample of tooth enamel powder with smaller grain size (<0.12 mm) was placed in an EPR tube to record the 'native' (0 Gy dose) EPR signal. The other sample of tooth enamel with grain size <0.12 mm was used for irradiation to 1 Gy.

The fingernails were prepared by Alexander Romanyukha at the US Naval Dosimetry Center, who collected his own fingernails for the radiation. The fingernails were irradiated using a calibrated ^{137}Cs source. The sample was treated with warm water to eliminate the mechanical-induced signals (MIS) (Trompier, Romanyukha et al. 2014). A 16 mg sample of 10 Gy irradiated fingernails was placed in a 4 mm O.D. quartz EPR tube for the CW and rapid scan comparison. 10 Gy irradiation provides a strong EPR signal.

3.2.2. Sample Irradiation

A ^{137}Cs irradiator (Atomic Energy of Canada Limited Gammacell 40) with an approximate dose rate of 1 Gy/min was used for irradiation of the tooth enamel and fingernail samples. The irradiator dose rate was verified by using US Navy TLD (thermo luminescence dosimeters) as described in (Reyes 2008). The US Navy dosimetry system DT-702/PD is traceable to the NIST ^{137}Cs source and it is in full compliance with the requirements of the American National Standard for dosimetry ANSI HPS N13.11-2009. For detailed descriptions of DT-702/PD references see (Cassata, Moscovitch et al. 2002,

2009, Romanyukha, King et al. 2012). Reyes estimated that the bias between the Navy TLD dosimeters and the ^{137}Cs irradiator was 6% (Reyes 2008).

3.2.3 EPR Spectroscopy

A Bruker E500T spectrometer was used to record CW and rapid scan spectra with a Bruker Flexline ER4118X-MD5 dielectric resonator, which can excite spins over a sample height of 1 cm. Since sample heights were about 6 mm, uniform B_1 and scan field were ensured along the full length of the samples. The Q of the resonator is ~9000 for these nonlossy samples. A Bruker SpecJet II fast digitizer was used to record rapid scan spectra. The phase difference between the quadrature detection channels was calibrated with a small sample of solid BDPA radical (Yu, Quine et al. 2014). The deviation between the Kronig-Kramers transformation of the absorption signal and the observed dispersion signal showed that a phase correction of 7^o was required. This correction was applied in the post-processing of the rapid scan signals.

The sinusoidal scans were generated with the recently described scan driver (Quine, Mitchell et al. 2012). The scan coils were constructed from 200 turns of Litz wire (255 strands of AWG44 wire). The coils have about 7.6 cm average diameters and were placed about 4 cm apart. The coil constant was 37.7 G/A, which is sufficient to generate scans up to 60 G wide with scan frequencies up to 35 kHz. Mounting the coils on the magnet, rather than on the resonator, reduces the oscillatory background signal induced by the rapid scans. The placement of highly conducting aluminum plates on the poles of the Bruker 10" magnet reduces resistive losses in the magnet pole faces that arise

from induced currents. The dielectric resonator decreases eddy currents induced by the rapidly changing magnetic fields relative to resonators with larger amounts of metal. Data were acquired in blocks of 5-6 sinusoidal cycles. For a sinusoidal scan the rate varies through the spectrum and is $\pi f_s B_m$ G/s at the center for the scan. For the spectra used in this study this rate was 6.6 MG/s, where f_s is the scan frequency (35 kHz) and B_m is the scan width (60 G).

To select the incident microwave powers for the CW and rapid scan experiments, power saturation curves were examined for the tooth enamel sample irradiated with 10 Gy (Fig. 3.1). At this dose the EPR spectrum for the irradiated teeth samples is dominated by the RIS that is assigned to $CO_2^{\cdot-}$ (Fattibene and Callens 2010). The amplitudes of peaks in CW spectra and rapid scan signals were measured as a function of microwave power. The incident powers were converted to B_1 using the known resonator efficiency of 3.8 $G/W^{1/2}$ at Q of 9000 (Mitchell, Tseitlin et al. 2013). The power selection was done using the following criterion. A linear least-squares fit through the point 0,0 and the signal amplitudes at the lowest 5 or 6 microwave powers was extrapolated to higher B_1. The B_1 selected for data acquisition was the point at which the experimental signal amplitude was about 5% lower than the amplitude predicted by linear extrapolation of the non-saturated signal amplitude. The modulation frequency for the CW spectra was 100 kHz. The modulation amplitudes (0.76 G) were about 20% of ΔB_{pp} of the RIS in tooth enamel. These parameters result in less than 2% line broadening relative to spectra obtained at lower modulation amplitude and smaller B_1. The data acquisition times were about 34 min. The estimates of 34 min acquisition times were based on the following

calculations, which are consistent with the relatively small overhead in the software. For CW spectra the acquisition time is the conversion time per point multiplied by the number of field steps. For rapid scans the acquisition time is ($1/f_S$) multiplied by the product of number of scan cycles combined in the deconvolution software and the number of scans averaged.

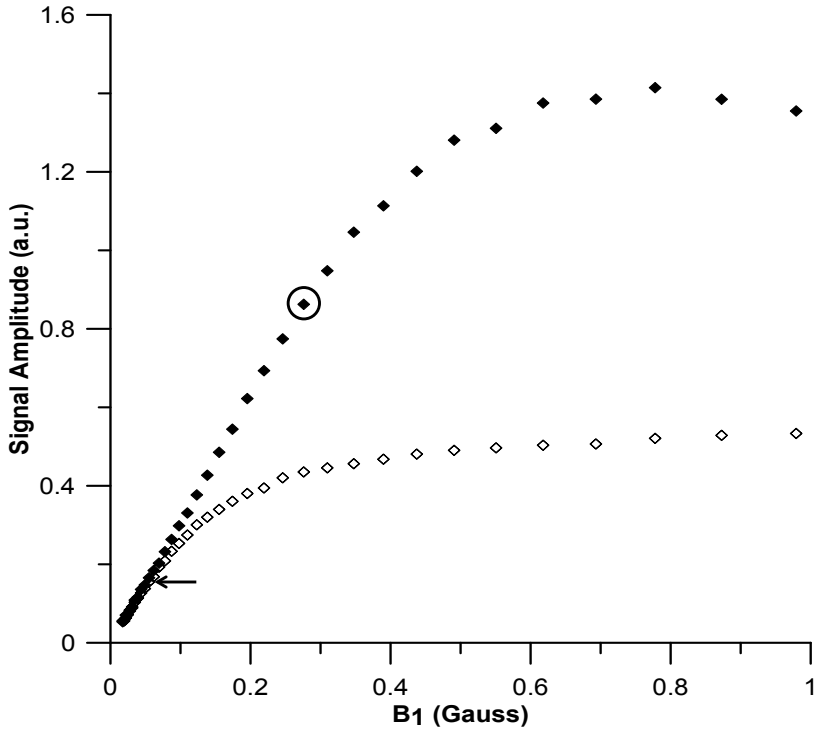

Fig. 3.1 Power saturation curves for the RIS in tooth enamel irradiated to 10 Gy obtained by conventional CW (◇) or rapid scan (◆). The powers selected for recording the CW and rapid scan spectra in Fig. 3.3 are indicated with an arrow or circle, respectively. Spectra and data reproduced from the original journal article (Yu, Romanyukha et al. 2015).

To select the incident microwave powers for the comparison between CW and rapid scan experiments, power saturation curves were examined for the fingernails irradiated with 10 Gy (Fig. 3.2). The B_1 selected for data acquisition was the point at which the experimental signal amplitude was about 5% lower than the amplitude predicted by linear extrapolation of the non-saturated signal amplitude. The modulation frequency for the CW spectra was 100 kHz. The modulation amplitudes (2.0 G) were about 20% of ΔB_{pp} of the RIS in fingernails. The data acquisition times were about 15 min.

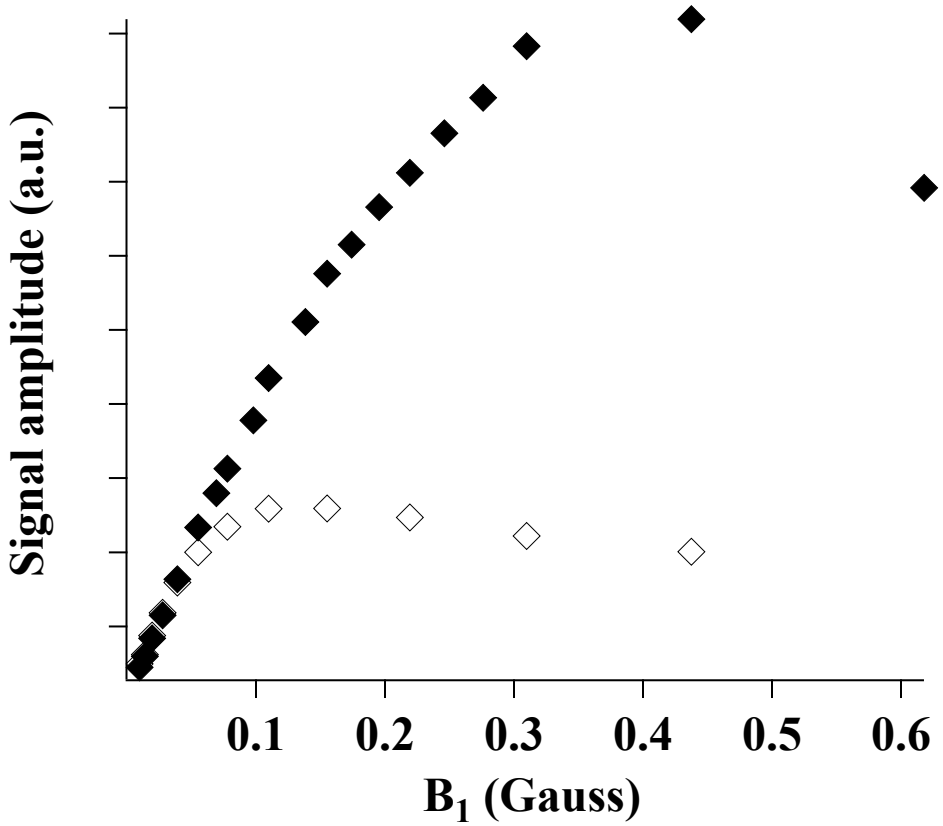

Fig. 3.2 Power saturation curves for the RIS in fingernails irradiated to 10 Gy obtained by conventional CW (◇) or rapid scan (◆). (Unpublished work)

3.2.4 Signal processing

The rapid scan signals were deconvolved, background removed, and baseline corrected (Tseitlin, Rinard et al. 2011, Tseitlin, Mitchell et al. 2012). In the deconvolution procedure the signals from the two quadrature channels for up-field and down-field scans are combined (Tseitlin, Quine et al. 2010). A post-processing Gaussian filter was applied to both CW and rapid scan spectra. The bandwidth of the first derivative spectrum is larger than for the absorption spectrum of the same signal. The first derivative spectrum was therefore calculated by numerical differentiation of the deconvolved rapid scan spectrum before low-pass filtering, with subsequent application of low-pass filtering. *S/N* is the peak-to-peak signal amplitude for CW or signal amplitude for rapid scan divided by RMS noise in baseline regions of the spectrum.

Spectra of irradiated teeth were simulated as the sum of contributions from the native and radiation-induced signals using EasySpin 5.0 (Stoll and Schweiger 2006). The solid state EPR simulation function 'pepper' and Nelder-Mead simplex hybrid method were used and parameters were adjusted iteratively to give the best fit to the spectra of the 10 Gy sample obtained by CW or rapid scan. To permit use of the same fitting model for CW and rapid scan, the first derivatives of the rapid scan absorption spectra were analyzed. These parameters were then used to simulate the spectra of the 1 Gy sample to show the reproducibility in the low dose region.

3.3 Results

3.3.1 Comparison of CW and rapid scan spectra of 10 Gy irradiated tooth enamel

Fig. 3.3 compares CW and rapid scan spectra for a tooth enamel sample irradiated to 10 Gy. The spectra are in good agreement with prior reports (Bugay, Bartchuk et al. 1999, Fattibene and Callens 2010). The peaks observed at about 3439 and 3431 G with a microwave frequency 9.62 GHz correspond to the reported g values of $g_{\perp}$ = 2.002 and $g_{||}$ = 1.997 for the dose-dependent signal (Bugay, Bartchuk et al. 1999, Fattibene and Callens 2010). The native signal has longer electron spin relaxation times and saturates more readily than the RIS (Ignatiev, Romanyukha et al. 1996, Sato, Filas et al. 2007). The B_1 selected for the CW and rapid scan experiments selectively enhances the RIS relative to the native signal (Ignatiev, Romanyukha et al. 1996). The weak peak from the native signal observed at about 3425 G (Fig. 3.3) is consistent with literature reports of g = 2.0045 and a linewidth of 7 to 8 G (Fattibene and Callens 2010). The *S/N* for the rapid scan spectrum is about 10 times higher than for the CW spectrum recorded with the same data acquisition time (Fig. 3.3).

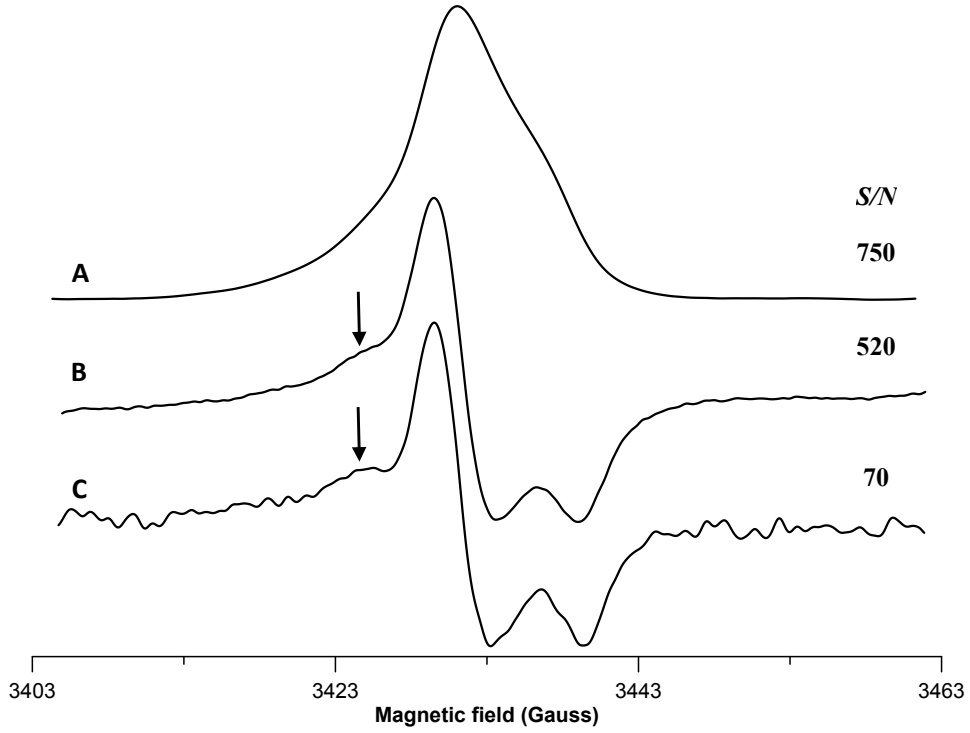

Fig. 3.3 EPR spectra of 60 mg of tooth enamel irradiated to 10 Gy obtained with 34 min acquisition time at 9.62 GHz. A) Absorption spectrum obtained by rapid scan with B_1 = 276 mG. B) First derivative of spectrum in A. C) Conventional CW spectrum obtained with 0.76 G modulation amplitude and B_1 = 55 mG. The microwave B_1 for the two methods was selected to give comparable degrees of power saturation of the RIS. The arrows mark the peak due to the native signal. Spectra and data reproduced from the original journal article (Yu, Romanyukha et al. 2015).

3.3.2 RIS in tooth enamel samples with lower radiation dose

One of the main objectives of this work was to investigate the ability of the rapid scan technique to improve *S/N* and thereby improve resolution of radiation-induced and native signals in irradiated tooth enamel samples. Therefore it was important to study samples with different (variable) contributions of these two signals to the EPR spectrum of the tooth enamel samples. To vary the relative intensities of the native and radiation-induced signals, different radiation doses (e.g. 0, 0.5, 1, and 10 Gy) were examined. The relative intensity of the native and radiation-induced signals depends also on the sample grain size (Fattibene and Callens 2010). That is why the 0 and 1 Gy samples were chosen to have a smaller grain size (<0.12 mm) than the 0.5 and 10 Gy samples (0.12-0.50 mm). Known differences in the grain size for samples with 0.5, 1, and 10 Gy radiation can be responsible for up to 60% difference in radiation sensitivity for samples irradiated to 1 Gy vs. 0.5 and 10 Gy. Fattibene and Callens (Fattibene and Callens 2010) described several effects of grain size on the EPR signals in tooth enamel. (i) The dose conversion may depend on grain size. (ii) Defect stability may depend on grain size. (iii) The surface may be a larger factor for smaller grain size. (iv) Samples with different grain size may result in differences in the EPR resonator filling factor.

Spectra of tooth enamel irradiated to 1 Gy and a native sample are shown in Fig. 3.4. For the native sample or radiation doses of 0.5 or 1 Gy the conventional CW spectra obtained with 34 min data acquisition time were extremely noisy. To acquire data with adequate *S/N* for analysis would have required very long signal averaging time. Thus only the rapid scan spectra are shown in Fig. 3.4 and 3.5. The smaller grain size in the

native (0 Gy) sample increases the intensity/gram of the native signal so 60% of the amplitude of the native signal was subtracted from the spectra of samples irradiated with doses of 1 or 0.5 Gy. The resulting difference spectrum for the 1 Gy sample has the lineshape expected for the dose-dependent signal, which is seen more clearly in the first-derivative than in the absorption spectrum. The *S/N* is good enough to estimate the dose. The peak-to-peak amplitude of the first-derivative signal is 16% of that observed for the 10 Gy sample, which indicates a dose of 1.6 Gy. As discussed above, the known difference in the grain size for samples with 0.5, 1, and 10 Gy can be responsible for the difference in radiation sensitivity for samples irradiated to 1 Gy vs 0.5 and 10 Gy.

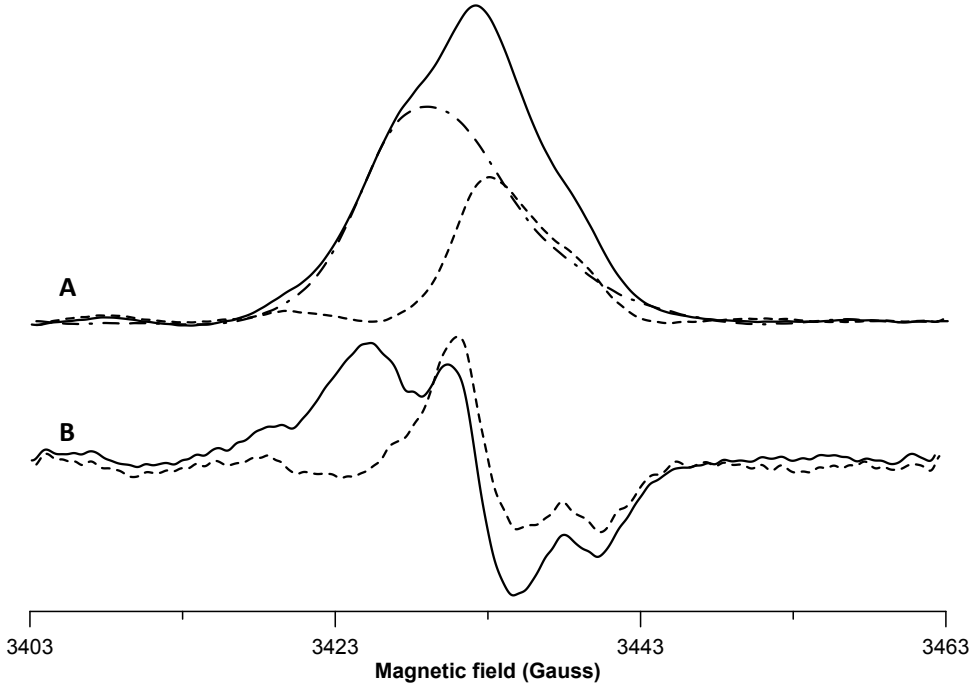

Fig. 3.4 Rapid scan EPR spectra of 60 mg irradiated tooth enamel obtained with B_1 = 276 mG and 34 min acquisition time. A) Absorption spectra of sample irradiated to 1 Gy (——), native signal (— · — ·), and difference between spectra irradiated to 1 Gy and native signal (— —). B) First derivatives of spectra in part A for sample irradiated to 1 Gy (——) and the difference spectrum (— —). Spectra and data reproduced from the original journal article (Yu, Romanyukha et al. 2015).

The spectrum for the 0.5 Gy sample and the result obtained by subtraction of the native signal are shown in Fig. 3.5. Although the *S/N* for the difference spectrum is low, the features due to the dose-dependent signal are still clearly discernible with a peak-to-peak amplitude of the first derivative spectrum about 5% of that for the 10 Gy sample, which is in good agreement with the reported dose of 0.5 Gy (Yu, Romanyukha et al. 2015).

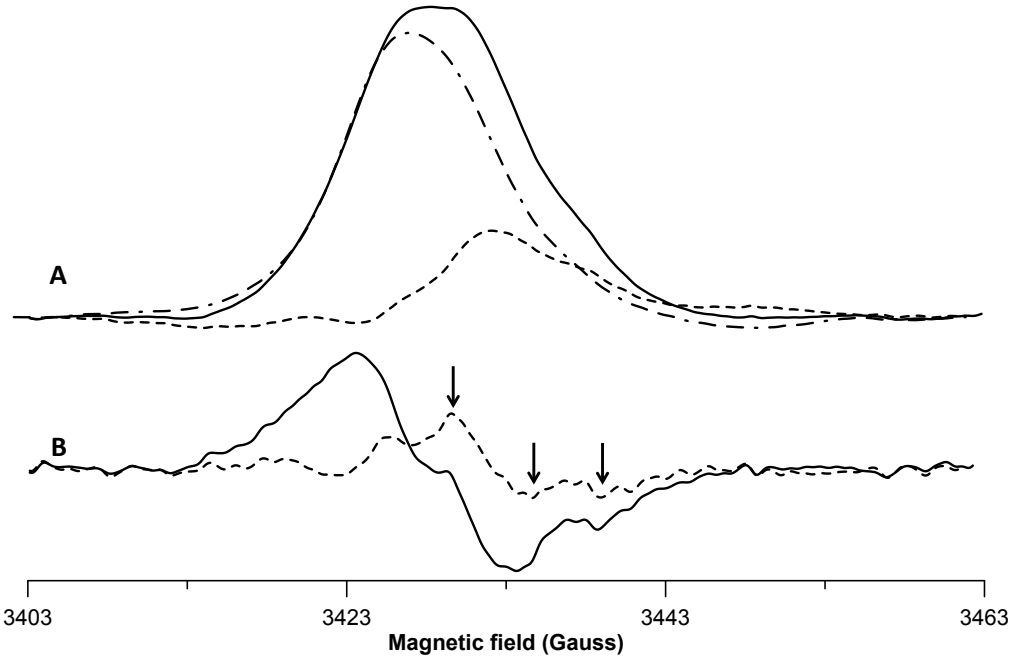

Fig. 3.5 Rapid scan EPR spectra of irradiated tooth enamel obtained with B_1 = 276 mG and 34 min acquisition time. A) Absorption spectra of sample irradiated to 0.5 Gy (———), native sample (——· ——·), and difference between spectra irradiated to 0.5 Gy and native sample (— — —). B) First derivatives of spectra in part A for sample irradiated to 0.5 Gy (———) and the difference spectrum (— — —). The arrows highlight features of the RIS. Spectra and data reproduced from the original journal article (Yu, Romanyukha et al. 2015).

For the 1 Gy sample three replicate EPR spectra were recorded by CW and three by rapid scan (Table 3.1). The coefficient of variance of the calculated dose based on simulation of the first-derivative spectra as the sum of native and radiation-induced signals was 3.9% for CW and 0.4% for rapid scan. Thus the improved *S/N* results in substantially improved precision in the calculated dose.

Table 3.1 Reproducibility of the RIS by CW EPR and rapid scan EPR of 1 Gy tooth enamel sample, Table and data reproduced from the original journal article (Yu, Romanyukha et al. 2015).

The reproducibility of RIS of CW spectra		
Spectrum	*S/N* of the original spectrum	CV of RIS
A	19	3.9%
B	17	
C	17	
The reproducibility of RIS of rapid scan first derivative spectra		
Spectrum	*S/N* of the original spectrum	CV of RIS
A	46	0.4%
B	48	
C	46	

3.3.3 Spectra simulations and replicates for dose estimation

The replicates and simulations shown in this section document the improved precision of dose estimation that results from the improved S/N, using data for the 1 Gy sample. The resulting g values (Table 3.2, 3.3) are in good agreement with the literature (Fattibene and Callens 2010). Since mT is the magnetic field unit in EasySpin, the following spectra and data were showed in mT.

3.3.3.1 Simulation of CW and rapid scan EPR spectra for the 10 Gy sample

The simulation of the CW spectrum of the 10 Gy sample (Fig. 3.2C) is shown in Fig. 3.6. The simulation of the first derivative of the rapid scan spectrum of the 10 Gy sample (Fig. 3.2B) is shown in Fig. 3.7.

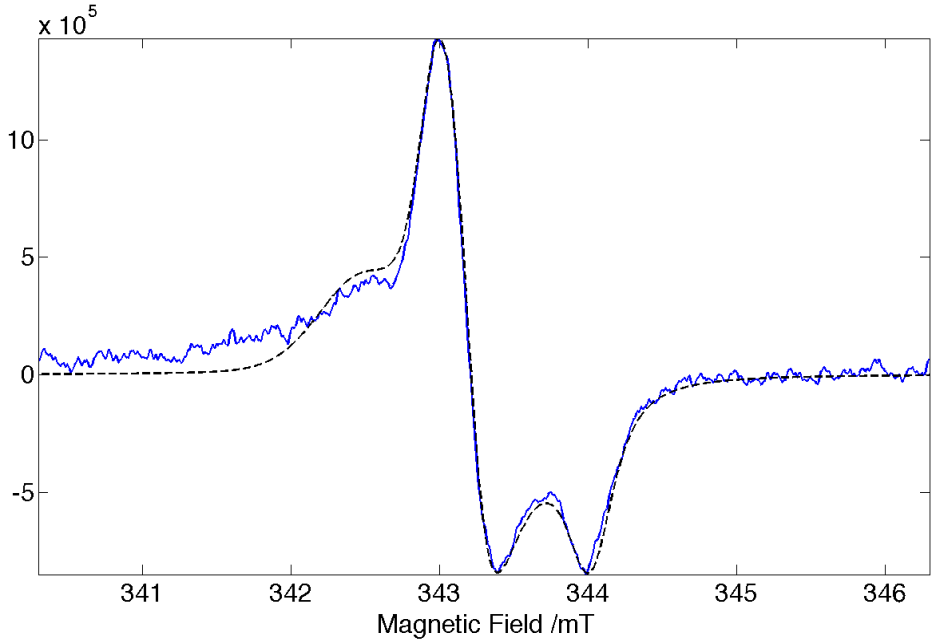

Fig. 3.6 Simulation (dashed black line) of the CW EPR spectrum (solid blue line) of the 10 Gy tooth enamel sample calculated using the parameters listed in Table 3.2. Spectra and data reproduced from the original journal article (Yu, Romanyukha et al. 2015).

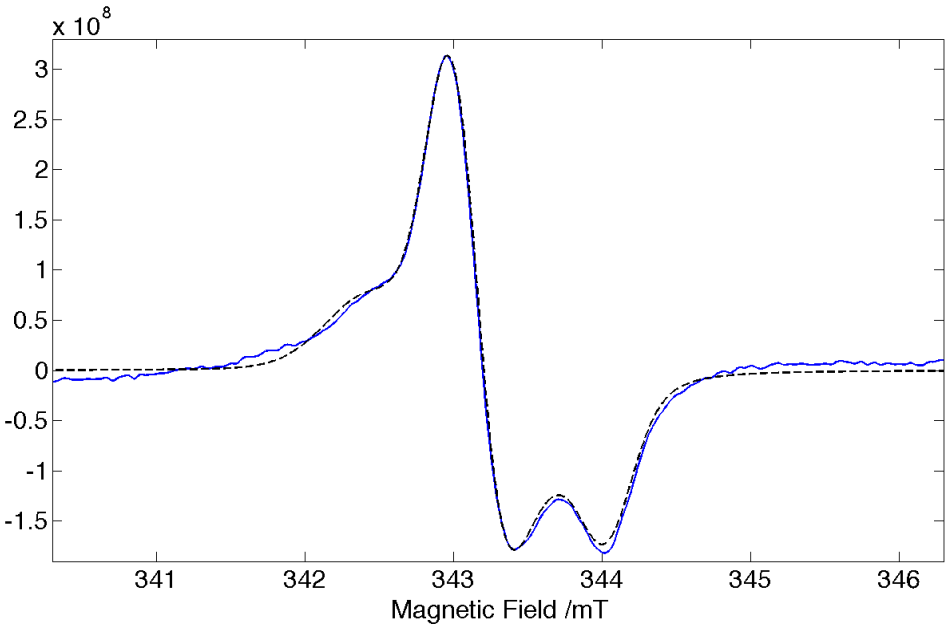

Fig. 3.7 Simulation (dashed black line) of the rapid scan first derivative EPR spectrum (solid blue line) of the 10 Gy tooth enamel sample calculated using the parameters listed in Table 3.2. Spectra and data reproduced from the original journal article (Yu, Romanyukha et al. 2015).

Table 3.2 EasySpin simulation parameters for CW and rapid scan spectra of 10 Gy tooth enamel sample. Table and data reproduced from the original journal article (Yu, Romanyukha et al. 2015).

Spectrum	Native signal		Irradiated signal				
	g	Gaussian broadening /mT	g_x	g_y	g_z	Gaussian broadening /mT	Lorentzian broadening /mT
CW	2.0048	0.67	2.0034	2.0021	1.9974	0.13	0.18
RS	2.0048	0.67	2.0032	2.0020	1.9970	0.28	0.12

3.3.3.2 Three replicates of CW and rapid scan EPR spectra for the 1 Gy sample

The CW spectra for which the *S/N* were reported in Fig. 3.3 were recorded with a modulation amplitude of 0.76 G to avoid broadening of the lines. Three replicates of the CW spectra of the 1 Gy sample (Fig. 3.8) were recorded with 2 G modulation amplitude, which is about 65% of the peak-to-peak linewidth. The higher modulation amplitude was used to improve *S/N* for the spectra in Fig. 3.8 to make the results for the CW spectra as favorable as possible. The microwave B_1 (55 mG) and data acquisition time (34 min) are the same as was used in Fig. 3.3. The fitting parameters are summarized in Table 3.3.

Three replicates of the rapid scan spectra of the 1 Gy sample (Fig. 3.9) were obtained with B_1 = 276 mG, a scan frequency of 35 kHz, and 34 min acquisition time. The fitting parameters are summarized in Table 3.3.

Table 3.3 EasySpin simulation parameters for CW and rapid scan spectra of 1 Gy tooth enamel sample. Table and data reproduced from the original journal article (Yu, Romanyukha et al. 2015).

CW results						
Spectrum	Native signal		Irradiated signal			
	g	Gaussian broadening /mT	g_x	g_y	g_z	Gaussian broadening /mT
A	2.0042	0.95	2.0032	2.0023	1.9972	0.22
B	2.0042	0.95	2.0033	2.0023	1.9973	0.15
C	2.0042	0.95	2.0034	2.0020	1.9973	0.15
Rapid scan EPR results						
Spectrum	Native signal		Irradiated signal			
	g	Gaussian broadening /mT	g_x	g_y	g_z	Gaussian broadening /mT
A	2.0048	0.67	2.0035	2.0016	1.9970	0.18
B	2.0048	0.66	2.0035	2.0016	1.9970	0.19
C	2.0048	0.67	2.0035	2.0016	1.9970	0.17

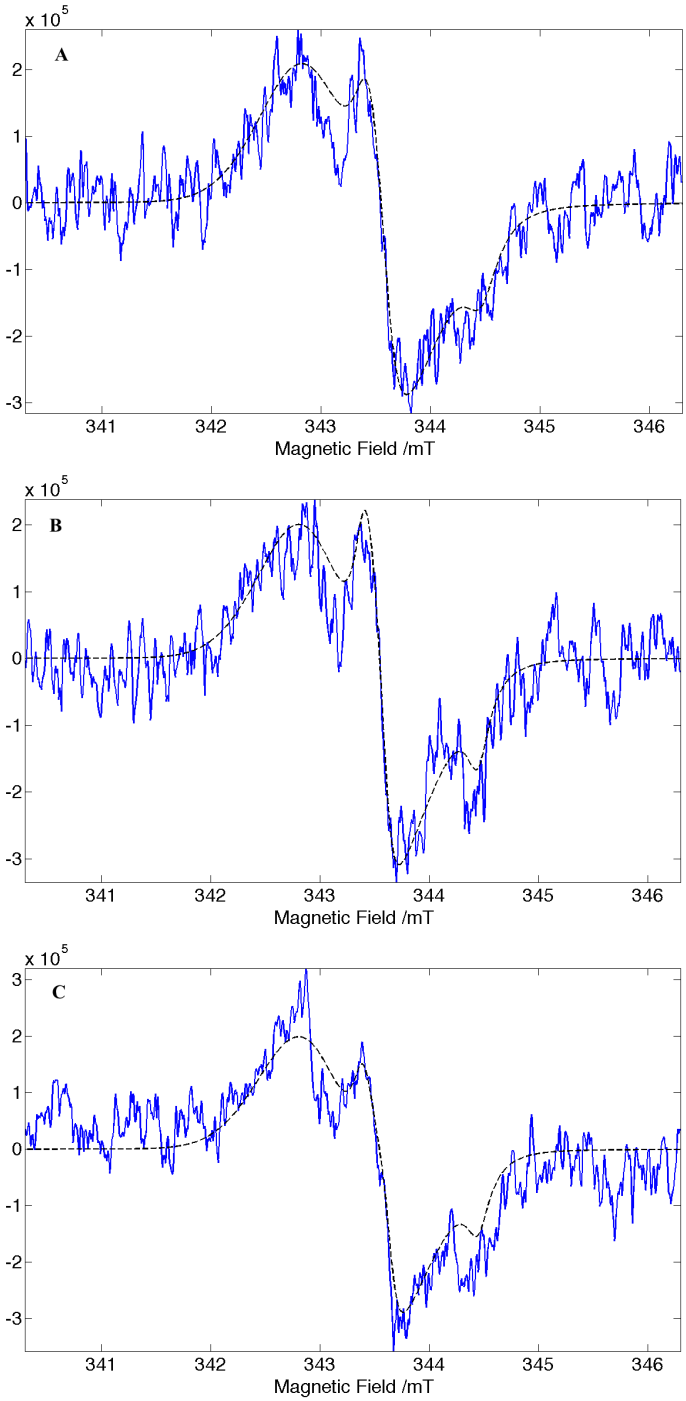

Fig. 3.8. Simulations (dashed black lines) for three replicates of the CW spectrum (solid blue lines) for the 1 Gy sample. Spectra and data reproduced from the original journal article (Yu, Romanyukha et al. 2015).

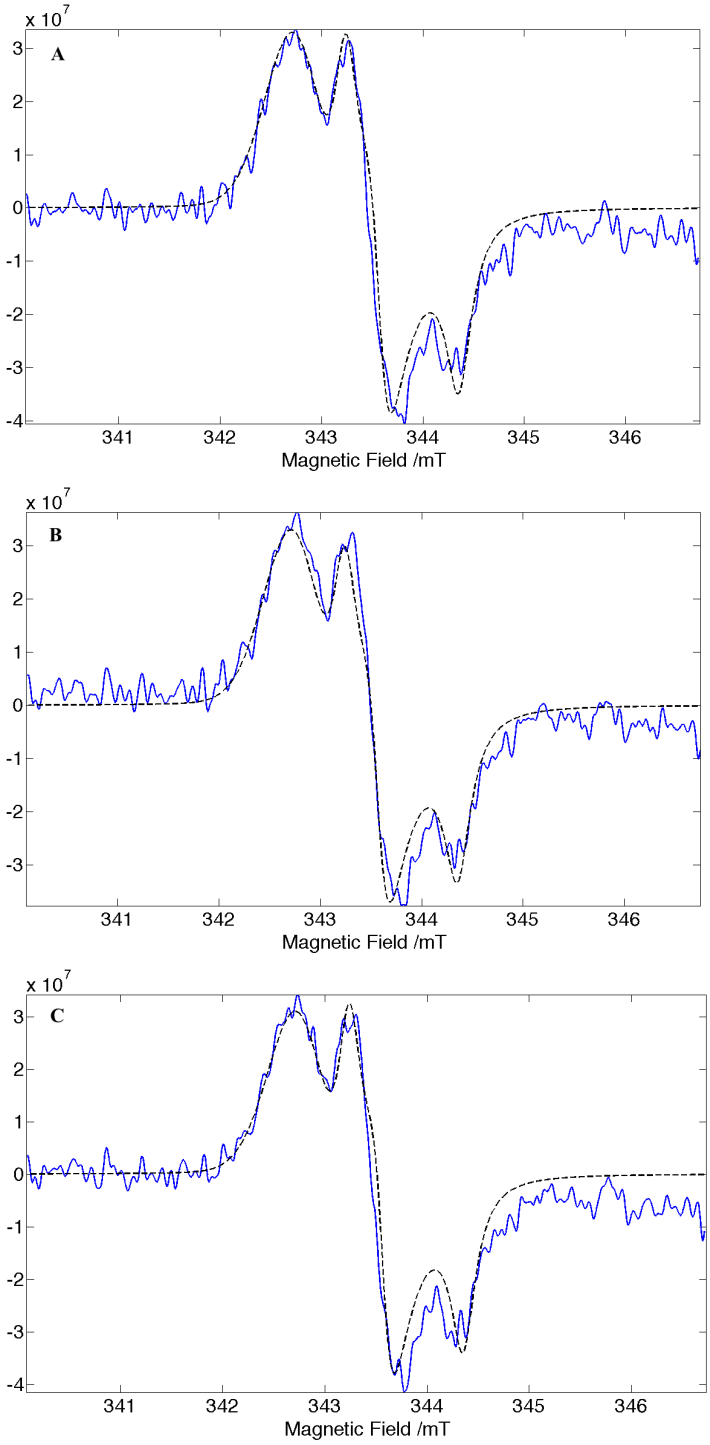

Fig. 3.9. Simulations (dashed black lines) for three replicates of the rapid scan first derivative spectrum (solid blue lines) for the 1 Gy sample. Spectra and data reproduced from the original journal article (Yu, Romanyukha et al. 2015).

3.3.3.3 The reproducibility of radiation-induced EPR signals (RIS) measured by CW and rapid scan EPR

The amplitudes of the RIS signals obtained by simulation of the three replicate spectra recorded by CW and rapid scan EPR are shown in Table 3.1. The values of *S/N* reported in the table were calculated as the amplitude of the RIS signal divided by the standard deviation of the noise. The coefficient of variance (CV) for the 3 replicates was calculated as the standard deviation of the amplitudes for the RIS signal divided by the average signal amplitude. The higher *S/N* for the rapid scan data translates into about an order of magnitude smaller CV and thus almost an order of magnitude improved precision of the calculated dose. The dose for the 1 Gy sample was calculated as 1.6 Gy based on the ratio of the amplitude of the RIS signal for this sample to that for the 10 Gy sample.

3.3.4 Comparison of CW and rapid scan spectra of 10 Gy irradiated fingernails

Fig. 3.10 compares CW and rapid scan spectra for a fingernail sample irradiated to 10 Gy. The spectra are in good agreement with prior reports (Romanyukha, Trompier et al. 2014, Trompier, Romanyukha et al. 2014). The *S/N* for the rapid scan spectrum is substantially higher than for the CW spectrum recorded with the same data acquisition time (Fig. 3.10).

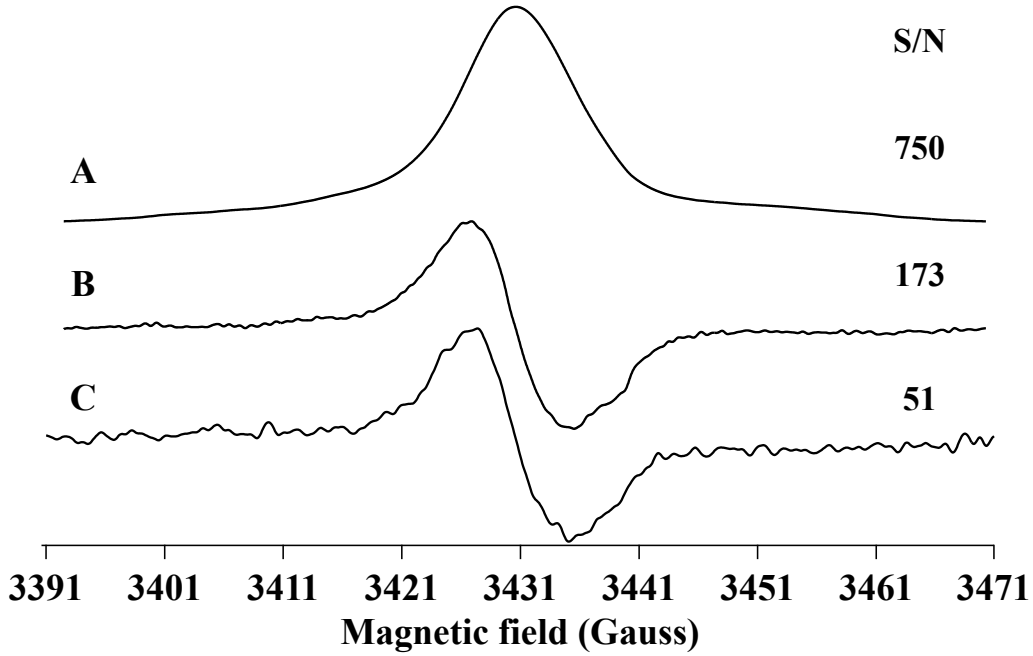

Fig. 3.10 EPR spectra of 16 mg of fingernails irradiated to 10 Gy obtained with 15 min acquisition time at 9.62 GHz. A) Absorption spectrum obtained by rapid scan with B_1 = 78 mG. B) First derivative of spectrum in A. C) Conventional CW spectrum obtained with 2 G modulation amplitude and B_1 = 31 mG. The microwave B_1 for the two methods was selected to give comparable degrees of power saturation of the RIS.

3.4. Discussion

For the same data acquisition time and conservative data acquisition parameters the *S/N* for rapid scan EPR of irradiated tooth samples or fingnernail samples is substantially higher than for conventional CW spectra. The X-band rapid scan spectra provide *S/N* for irradiated tooth enamel samples that are sufficient to clearly characterize the dose-dependent signal at a dose of 0.5 Gy. The *S/N* of each method could be

increased by using less conservative parameters. For example, one could allow somewhat more line shape distortion and use higher modulation amplitude in the CW spectra (Table 3.1). Up to a modulation amplitude of about half the line width, *S/N* will increase nearly linearly with increased modulation amplitude. Similarly, higher microwave power could be used for both CW and rapid scan spectra. The 5% deviation from linearity was an arbitrary criterion, to ensure accurate lineshapes that aid in separating the two overlapping signals. Rapid scan could be obtained at a higher scan rate, which would allow higher power without increase in saturation, but at some point the resonator bandwidth would start to over-filter the signal and distort the line shape (Eaton, Quine et al. 2014). Higher resonator Q could be used, but for rapid scan the filter effect of the Q could be a problem, as just described, and in CW EPR higher Q could result in higher noise (Eaton, Eaton et al. 2010).

The difference spectrum for the 0.5 Gy sample (Fig. 3.5) was based on a single spectrum for the native signal. With replicate measurements for the native sample it should be possible to characterize radiation doses significantly lower than 0.5 Gy.

EPR in tooth enamel has been successfully applied in many radiation epidemiological studies (Fattibene and Callens 2010), but it is difficult to apply in case of emergency because extracted teeth are not readily available in this situation. Recent instrument developments have made it possible to do in vivo EPR dose measurements in teeth (Swartz, Burke et al. 2007), but there is a problem with low *S/N* for the dose of concern, which is 1 - 2 Gy (Swartz, Burke et al. 2007). The rapid scan technique could be an approach to improving *S/N* for in vivo EPR dosimetry.

EPR in fingernails was applied for real life dose level estimation (Romanyukha, Trompier et al. 2014). Since the fingernails are easy to collect after the radiation emergency than tooth enamel samples, the fingernail dosimetry can provide a fast and reliable radiation dose measurements for victims of a radiation accident. However, the RISs of fingernails are very complicated (Trompier, Romanyukha et al. 2014). The mechanical-induced signals (MIS) might also superpose on the RIS when the samples are collected differently, which increases the difficulty of the application of the fingernail dosimetry.

3.5 Summary

Rapid scan EPR spectra at X-band for tooth enamel samples irradiated with 0.5, 1, and 10 Gy doses had substantially improved signal-to-noise relative to conventional CW EPR. The RIS in 60 mg of a sample irradiated with a dose of 0.5 Gy was readily characterized in spectra recorded with 34 min data acquisition times. The coefficient of variance of the calculated dose for a sample with 1 Gy radiation based on simulation of the first-derivative spectra for three replicates as the sum of native and radiation-induced signals was 3.9% for CW and 0.4% for rapid scan. The preliminary results from the rapid scan EPR for 16 mg fingernails irradiated to 10 Gy are shown a substantial improvement of *S/N*, which would help the dose estimation in the fingernail dosimetry.

CHAPTER 4

FIELD-STEPPED DIRECT DETECTION EPR

4.1 Introduction

The widest scan that had been previously demonstrated for rapid scan EPR was a 155 G sinusoidal scan (Yu, Quine et al. 2014). As the scan width increases, the voltage requirement increases dramatically and the background signal induced by the rapidly changing field increases. An alternate approach is needed to achieve wider scans. This author and co-workers have now developed field-stepped direct detection EPR (Yu, Liu et al. 2015), which is based on the rapid scan technology, to generate much wider scans. To test the performance of the method, samples were examined with a variety of linewidths and lineshapes. The narrowest linewidth (ΔB_{pp} = 22 mG) was for degassed lithium phthalocyanine (LiPc), which exhibited rapid-scan oscillations in the signal and required deconvolution to obtain the slow-scan absorption spectrum. Samples with resolved g- and A anisotropy include Cu^{2+} doped in Ni(diethyldithiocarbamate)$_2$ (Ni(Et$_2$dtc)$_2$), Cu^{2+} doped in Zn tetratolylporphyrin (ZnTTP), PDT in sucrose octaacetate, vanadyl ion doped in Zn p-COOH-tetratolylporphyin (ZnTTP-COOH), and Mn^{2+} impurity in CaO. The spectrum of a crystal of Mn^{2+} doped in Mg(acetylacetonate)$_2$(H$_2$O)$_2$ (Mg(acac)$_2$(H$_2$O)$_2$) has well-resolved hyperfine lines and low-intensity forbidden transitions over a sweep width of 6200 G.

4.2 Approach

To encompass a wide spectrum, multiple triangular scans were acquired with extensive overlap of the field ranges (Fig. 4.1). In the following description, specific values are given to facilitate understanding, but there is substantial flexibility in choice of parameters. For example to encompass a 150 G scan, 151 scans with widths of 11.5 G were recorded with 1 G offsets between the centers of the scans. Since linearity of a triangular scan is better in the center than at the extremes of the scan, only the central 80% segments of the scans were selected for inclusion in the combined data set. Thus for the example of 11.5 G scans, the central 9.2 G segments were used. The 1 G offset between centers of scans gives an 8.2 G region of overlap of each scan with the previous and following scans. The information from the up- and down-scans and from multiple cycles of the triangular scans is combined. In the direct-detected spectra the y axis values are relative to a DC offset that is different for each scan. To combine successive scans the offset was calculated as the difference between the means of the y-axis values in the overlapping 8.2 G regions. The large spectral overlaps provide accurate determination of the offsets. This offset correction was applied before averaging values from successive scans and combining into the spectral array. Since the scan rate of a triangular scan is constant across the spectrum, linear deconvolution can then be applied to obtain the slow-scan absorption spectrum. An example of MATLAB program is shown in Appendix A.

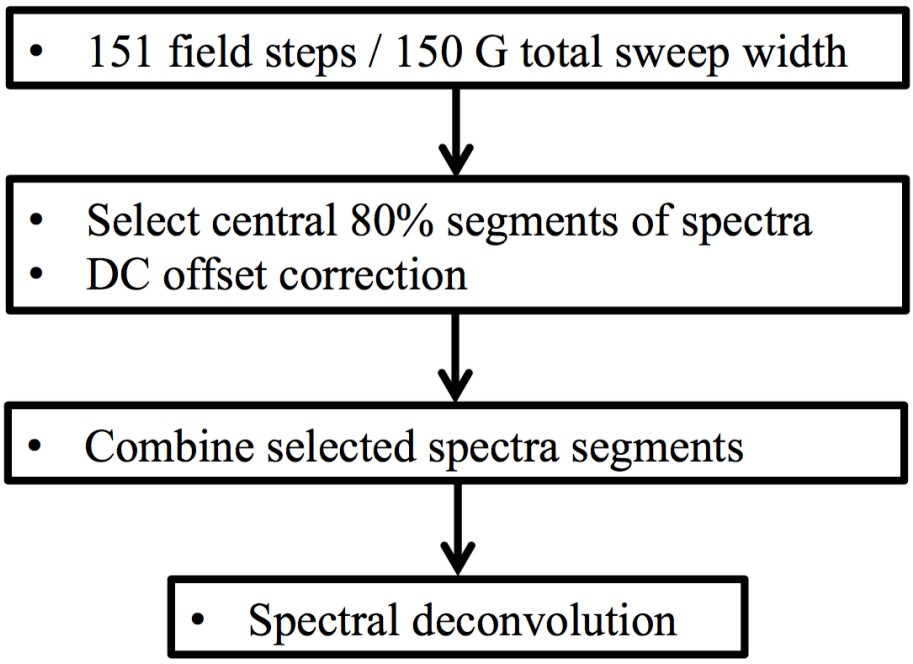

Fig. 4.1 Block diagram of post processing procedure for spectral reconstruction in field-stepped direct detection, using typical parameters. For example, data could be acquired at 151 field positions in 1.0 G increments over 150 G. Each scan is 11.5 G wide and the linear scan frequency is 5.12 kHz, which corresponds to a scan rate of 118 kG/s. From each of the scans the central 80 % is selected. The DC offset between scans is calculated by comparing signal intensity at the comparable fields in overlapping segments of successive scans and this correction is applied prior to combining the spectra. Diagram reproduced from the original journal article (Yu, Liu et al. 2015).

4.3 Methods

4.3.1 Samples

LiPc prepared electrochemically was provided by Prof. Swartz, Dartmouth College (Turek, Andre et al. 1987, Grinberg, Smirnov et al. 2005). A small crystal was placed in a capillary tube. The tube was evacuated overnight on a high vacuum line and then flame sealed. The capillary tube containing LiPc was placed in a 4 mm O.D. quartz tube beside a second capillary tube filled with water to a height of 1 cm to lower the Q of the resonator to about 1000. The bandwidth of the rapid scan signal for this sample is so large that a lowered Q is required to decrease broadening of the signal.

The preparation of Cu^{2+} doped in $Ni(Et_2dtc)_2$ was described in (Du, Eaton et al. 1995). The preparation of Cu^{2+} doped in ZnTTP and of VO^{2+} doped in ZnTTP-COOH were described in (Du, Eaton et al. 1996). The sample of nitroxide PDT in sucrose octaacetate was prepared as previously reported (Yu, Tseitlin et al. 2015). Calcium oxide was purchased from Sigma-Aldrich (product number 248568, St. Louis, MO). Mn^{2+} is an impurity in the reagent CaO powder. The sample was handled under nitrogen gas and placed in a 4 mm O.D. quartz tube. The tube was evacuated on a high vacuum system for about 6 hr, then flame sealed. $Mg(acac)_2(H_2O)_2$ was prepared and characterized as described in (Charles, Holter et al. 1960, Such and Lehmann 1987). The crystal doped with Mn^{2+} was grown from acetonitrile. Sample heights were 6 - 7 mm, to ensure uniform B_1 and scan field along the full lengths of the samples.

4.3.2 EPR spectroscopy

A Bruker E500T spectrometer was used to record CW and field-stepped direct detection spectra with a Bruker Flexline ER4118X-MD5 dielectric resonator, which can excite spins over a sample height of about 1 cm. The Q of the resonator is ~9000 for nonlossy samples (Mitchell, Tseitlin et al. 2013). A Bruker SpecJet II fast digitizer was used. The 10 ns timebase was selected for LiPc and for Mn^{2+} in $Mg(acac)_2(H_2O)_2$ and the 40 ns timebase was used for the other samples. The phase difference between the quadrature detection channels was calibrated with a small sample of solid BDPA (1:1 α,γ-bisdiphenylene-β-phenylallyl: benzene) radical (Tseitlin, Mitchell et al. 2012). The deviation between the Kronig-Kramers transformation of the absorption signal and the observed dispersion signal showed that a phase correction of 7^o was required. The amplitude difference between quadrature detection channels was calibrated with a small degassed sample of solid LiPc. There was a 7% amplitude difference between the I and Q channels. The corrections were applied in the post-processing of the field-stepped direct detection signals.

The linear scans were generated with the previously described scan driver (Quine, Czechowski et al. 2009). The scan coils were constructed from 60 turns of Litz wire (255 strands of AWG44 wire). The coils have about 8 cm average diameter, were placed about 4 cm apart, and have a coil constant of 17.3 G/A. Mounting the coils on the magnet, rather than on the resonator, reduces the oscillatory background signal induced by the rapid scans (Yu, Quine et al. 2014). The placement of highly conducting aluminum plates on the poles of the Bruker 10" magnet reduces resistive losses in the magnet pole faces

that arise from induced currents (Eaton, Quine et al. 2014). The dielectric resonator decreases eddy currents induced by the rapidly-changing magnetic fields relative to resonators with larger amounts of metal. The scan frequency of 5.12 kHz was selected because the background signal induced by the rapidly varying field is relatively small at this scan frequency. Since the linearity is high over more than 90% of the scan at 5.12 kHz, the use of only the central 80% is conservative. Data were acquired in blocks of 3 cycles at each field step. For the spectra used in this study, the scan rate is 118 kG/s, which is $2\times f\text{s}\times B_\text{m}$ G/s where fs is the scan frequency and B_m is the scan width.

The incident powers were converted to B_1 using the known resonator efficiency of 3.8 $\text{G/W}^{1/2}$ at Q of 9000 and the dependence of efficiency on √Q when Q is decreased (Mitchell, Quine et al. 2012). The power selection was relatively conservative to prevent distortion of the lineshape by power saturation at higher B_1. The modulation frequency for the CW spectra of LiPc was 10 kHz and the modulation frequencies for other samples were 100 kHz. The modulation amplitudes were selected to be about 20% of ΔB_pp for the narrowest feature in each spectrum. These parameters result in less than 2% line broadening relative to spectra obtained at lower modulation amplitude and smaller B_1. The large numbers of points acquired in the field axis of the field-stepped spectra were decreased by averaging about 100 points, to improve *S/N* and have a field resolution comparable to the CW spectra. First-derivatives of the field-stepped direct detection spectra were obtained by numerical differentiation followed by a Gaussian filter selected to give less than 5% broadening. The same Gaussian filter was applied to the CW spectra.

For CW spectra the acquisition time is the conversion time per point multiplied by the number of field steps and the number of scans, which is approximately equal to the elapsed time because there is little overhead in the software. For field-stepped direct detection, the calculated acquisition time is $1/f_s$ multiplied by the product of number of scan cycles combined in the software, the number of scans averaged and the number of field steps. The lapsed time is longer than the calculated time because of overhead in the software. For Cu^{2+} in $Ni(Et_2dtc)_2$, Cu^{2+} in ZnTTP, PDT in sucrose octaacetate, VO^{2+} in Zn(TTP-COOH) and Mn^{2+} in CaO, the data acquisition times were 15 min for both CW and field-stepped direct detection.

4.4 Results

Spectra showing the application of the field-stepped method for LiPc are shown in Fig. 4.2. The CW spectrum of degassed LiPc has a peak-to-peak linewidth of 22 mG and therefore provides a stringent test of the field-stepped approach with respect to lineshape fidelity and the deconvolution of rapid scan effects. High resolution of the field axis for the final spectrum is needed, so data were acquired at 201 center fields with 0.01 G increments. For the LiPc sample, the 11.5 G scans were much wider than required to construct the final 2.0 G spectrum, but the wider scans were selected to push the experiment into the rapid scan regime, and thereby test the effectiveness of the linear deconvolution procedure for the combined data (Joshi, Ballard et al. 2005). A 5.12 kHz scan frequency with 10 ns sampling in the Specjet II digitizer permits acquisition of three full cycles of the triangular scan within the available 64k memory. This results in 9766

points per half cycle, which corresponds to 1.2 mG/point. When spectra are combined, the selection of corresponding fields for which y-axis values should be averaged is limited by the field resolution of the initial data. To obtain adequate definition of the rapid scan oscillations (Joshi, Ballard et al. 2005, Joshi, Eaton et al. 2005), the initial data were linearly interpolated by a factor of 10, to give 0.12 mG/point resolution. If the oscillations are not well defined and accurately combined, the signal in the deconvolved spectrum is broadened. Interpolation was not needed for samples discussed below in which rapid scan oscillations were not observed. Plots of the central 80% of the 1^{st}, 101^{st}, and 201^{st} scans are shown in Fig. 4.2A. After the offsets of the central field are taken into account, the spectra aligned as shown in Fig. 4.2B. The combination of all 201 scans results in the spectrum shown in Fig. 4.2C. The absorption spectrum after linear deconvolution of the rapid scan effects (Joshi, Ballard et al. 2005) is shown in Fig. 4.2D and Fig. 4.3A. The first derivative of the spectrum in Fig. 4.3A, obtained by numerical differentiation (Fig. 4.3B) is in good agreement with the CW spectrum. The agreement between the CW lineshape and the lineshape obtained by deconvolution of a single scan is substantially better than with the lineshape obtained by combining multiple scans. The slight broadening (about 3 mG) of the field-stepped spectrum is attributed to field instabilities or trigger jitter in the digitizer.

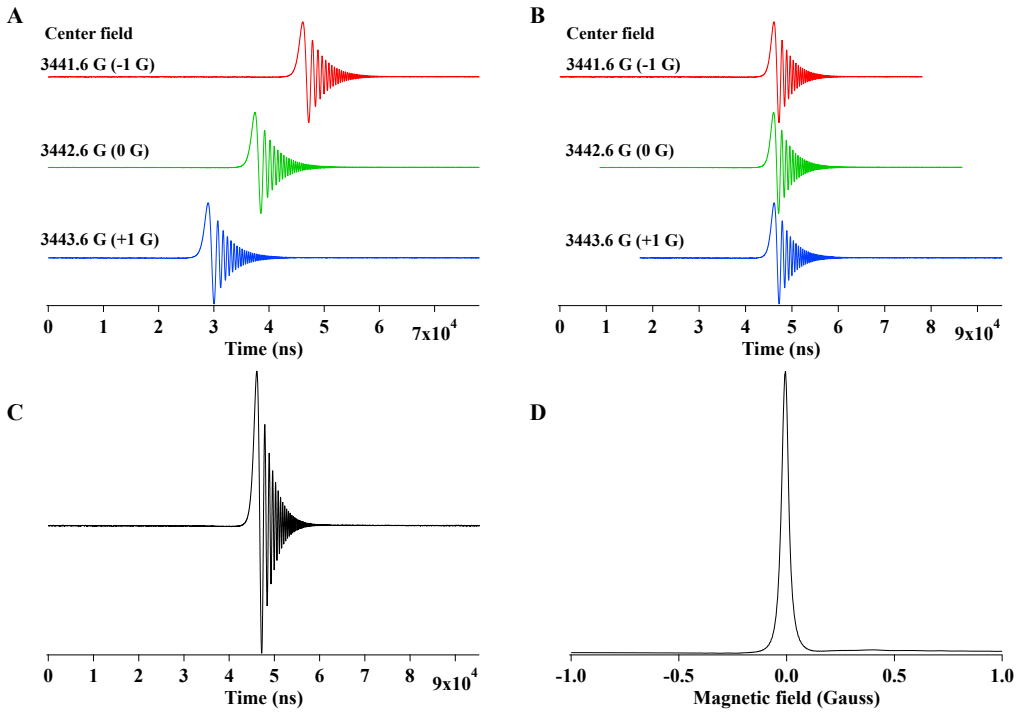

Fig. 4.2 Example of the spectral reconstruction procedure for LiPc. A) Spectrum numbers 1, 101, and 201 from the set of 201 spectral steps, showing the central 80%. B) Alignment of these three scans after shifting in time to correct for the stepping of the field. C) LiPc spectrum obtained by combining contributions from all 201 spectra, after correction for DC offset. For the LiPc spectra rapid scan oscillations were observed in the signal. D) The slow-scan absorption spectrum was reconstructed by deconvolution. Spectra and data reproduced from the original journal article (Yu, Liu et al. 2015).

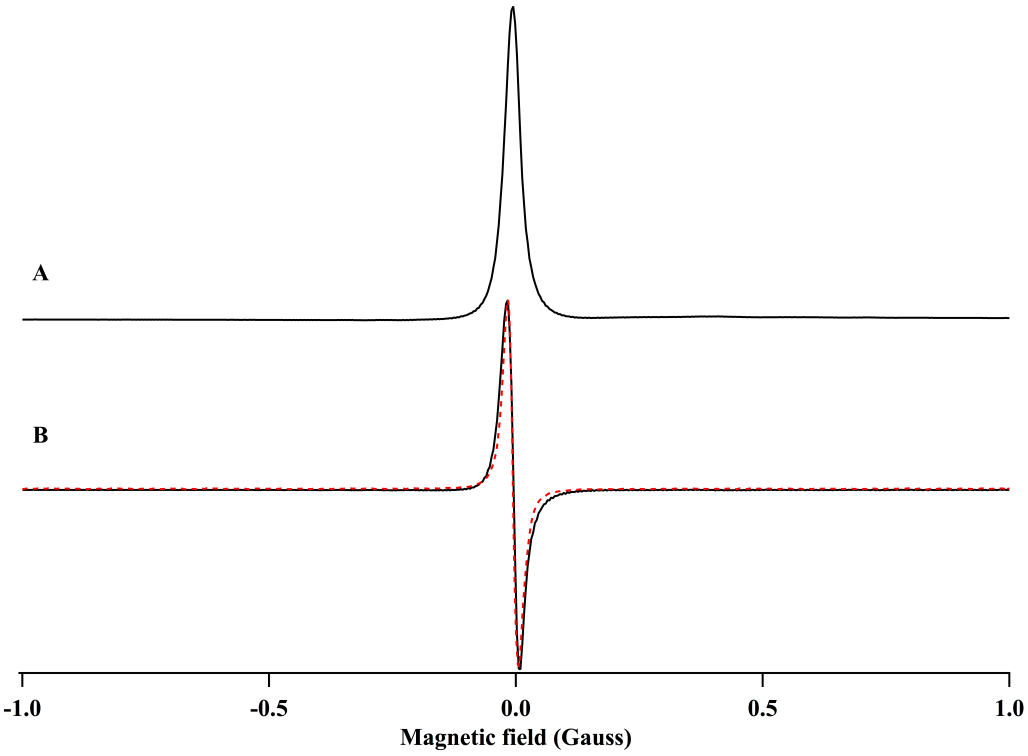

Fig. 4.3 A) Spectrum of LiPc obtained by field-stepped direct detection. B) The first derivative of the spectrum in part A (black, solid) overlaid on the CW spectrum (red, dashed) obtained with a modulation amplitude of 3.6 mG and 2 mG field resolution. The B_1 was 3.3 mG for both spectra. Spectra and data reproduced from the original journal article (Yu, Liu et al. 2015).

EPR spectra of immobilized type 1 Cu^{2+} complexes such as Cu^{2+} in $Ni(Et_2dtc)_2$ exhibit well-resolved g- and A-anisotropy and test the accuracy of the methodology for lineshapes that are broader than individual segments (Fig. 4.4). The field-stepped spectrum was obtained with 701 steps over 700 G (Fig. 4.4A). Five of these segments for a small region of the spectrum are shown in Fig. 4.4D. Although data are acquired with a time axis, the data in Fig. 4.4B – 4.4D are plotted with an x axis in magnetic field units that takes account of the increments in magnetic field for successive segments. Since the DC offset for each segment is arbitrary, the amplitude of the EPR signal at the same magnetic field position is different for each segment. The DC offset correction was calculated as the difference between the means of the y-axis values in the overlapping 8.2 G regions. After correction for the DC offset, the excellent superposition of segments in overlapping regions is shown in Fig. 4.4C. Averaging of the contributions from all segments that contribute to this region of the spectrum produces the result that is shown in Fig. 4.4B.

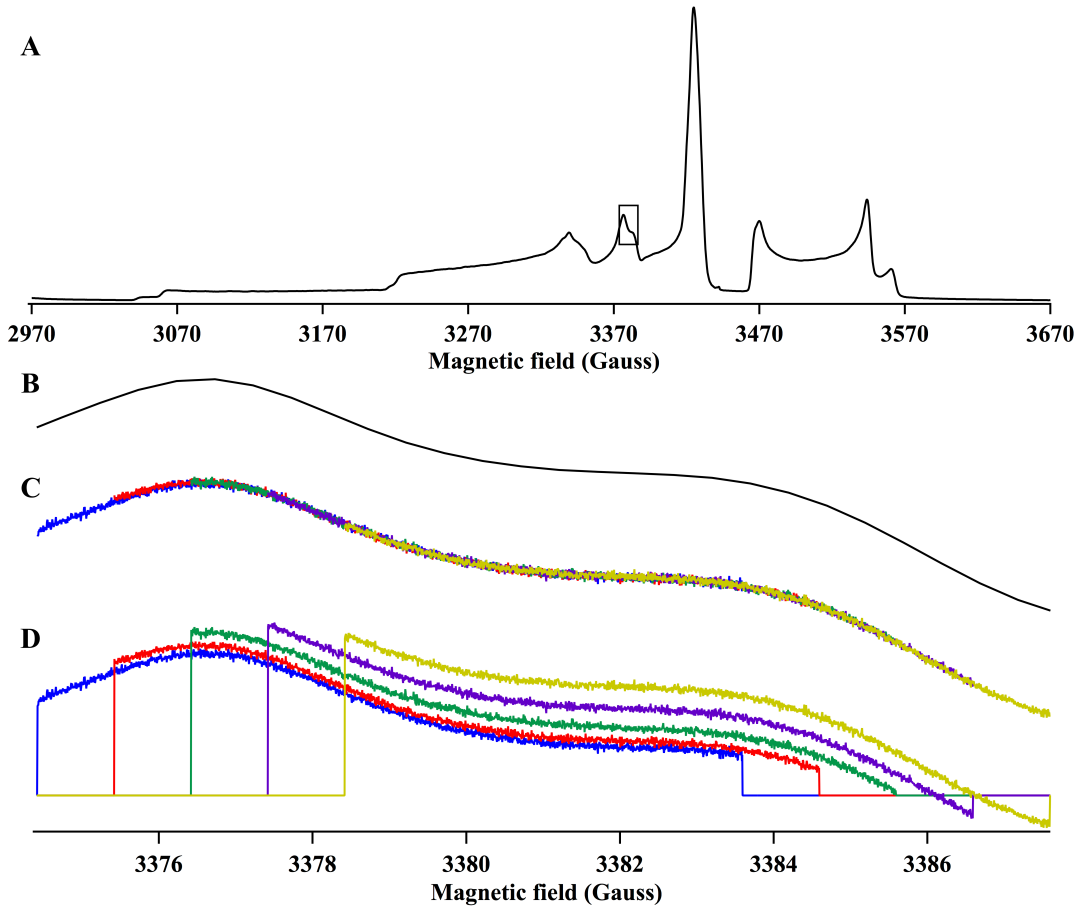

Fig. 4.4 Example of the DC offset correction. A) Spectrum of Cu^{2+} in $Ni(Et_2dtc)_2$ obtained by field-stepped direct detection in 701 steps over 700 G. The region that is expanded in parts B – D is marked with a box. B) Expansion of region between 3374.4 and 3387.6 G, obtained by averaging the segments that contribute in the region, after DC offset correction. C) Superposition of 5 successive segments that contribute to the spectrum between 3374.4 and 3387.6 G, after correction for DC offset. Each segment is shown in a different color. D) Five successive segments that contribute to the spectrum between 3374.4 and 3387.6 G, before correction for DC offset. The vertical lines denote the beginning and end of a particular segment. The y axis scales are the same for parts B to D. Spectra and data reproduced from the original journal article (Yu, Liu et al. 2015).

The rapidly-changing magnetic field induces a rapid-scan background signal (Eaton, Quine et al. 2014). For 11.5 G segments acquired with a scan frequency of 5.12 kHz and B_1 of 17.4 mG as was used to acquire the signals for most of the spectra in this report, the background signal is very small. The background signal increases with B_1. To demonstrate the potential impact of the rapid-scan background and DC offset correction, segments acquired with B_1 of 174 mG for an empty EPR tube are shown in Fig. 4.5.

Although prior studies have demonstrated that the background signal is dependent on the external magnetic field, the change between nearby segments is small (Fig. 4.5A). The amplitude of the DC component of the EPR signal, caused by RF reflected from the resonator is typically quite large compared to the detected EPR signal. The spectrometer has a low-pass filter to eliminate the high DC level of the recorded signal without impacting the EPR signal. Therefore, it is necessary to restore the relative DC level in each segment before combining them to obtain the complete spectrum. If no DC correction is applied, summation of the segments causes discontinuities at the beginning of each segment (Fig. 4.5B). Imperfections in the DC offset correction can leave residual discontinuities, which could potentially be removed by Fourier transformation and filtering to remove the frequencies that correspond to the reciprocal of the step interval (Hyde, Bennett et al. 2013). However, this procedure risks deletion of spectral components at this frequency. When the DC offset correction is applied before the segments are averaged, there are no discontinuities at the segment boundaries (Fig. 4.5C). The resulting baseline signal is a slowly varying monotonic function that is similar to the baseline functions that are commonly observed in CW spectra. Subtraction of a

linear fit function for this spectral range removes essentially all of the baseline (Fig. 4.5D). A more complicated polynomial fit might be needed for a wider scan. The baseline shown in Fig. 4.5C is for the absorption spectrum, and is barely noticeable after taking the first derivative.

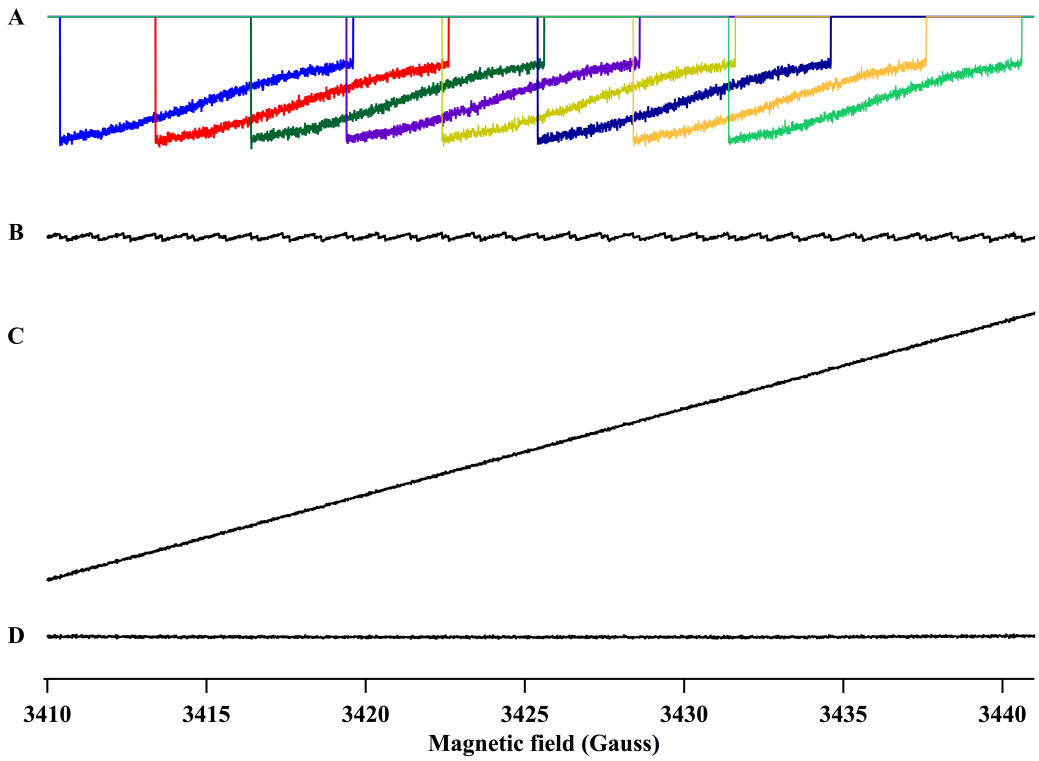

Fig. 4.5 Rapid scan background signals and DC offset correction for data acquired with a scan frequency of 5.12 kHz and B_1 = 174 mG. A) Sampling of 8 of the 22 segments that contribute in the region 3410 to 3441 G for an empty EPR tube. B) Signal obtained by summing all 22 segments without DC offset correction. C) Signal obtained by summing the 22 segments after DC offset correction. D) Signal obtained by subtraction of a linear fit to the data in part C. Spectra and data reproduced from the original journal article (Yu, Liu et al. 2015).

The field-stepped direct detected spectrum of Cu^{2+} in $Ni(Et_2dtc)_2$ (Fig. 4.4A) is compared with CW spectra of the same sample in Fig. 4.4. The spectra in Fig. 4.6 agree well with previously reported spectra for the same sample (Du, Eaton et al. 1995). In the region around 3430 G the resolution of the first derivative signal obtained by differentiation of the field-stepped spectrum (Fig. 4.6B) is slightly better than that for the CW spectrum (Fig. 4.6C) which is attributed to the large number of data points per gauss used in the stepped-field spectrum.

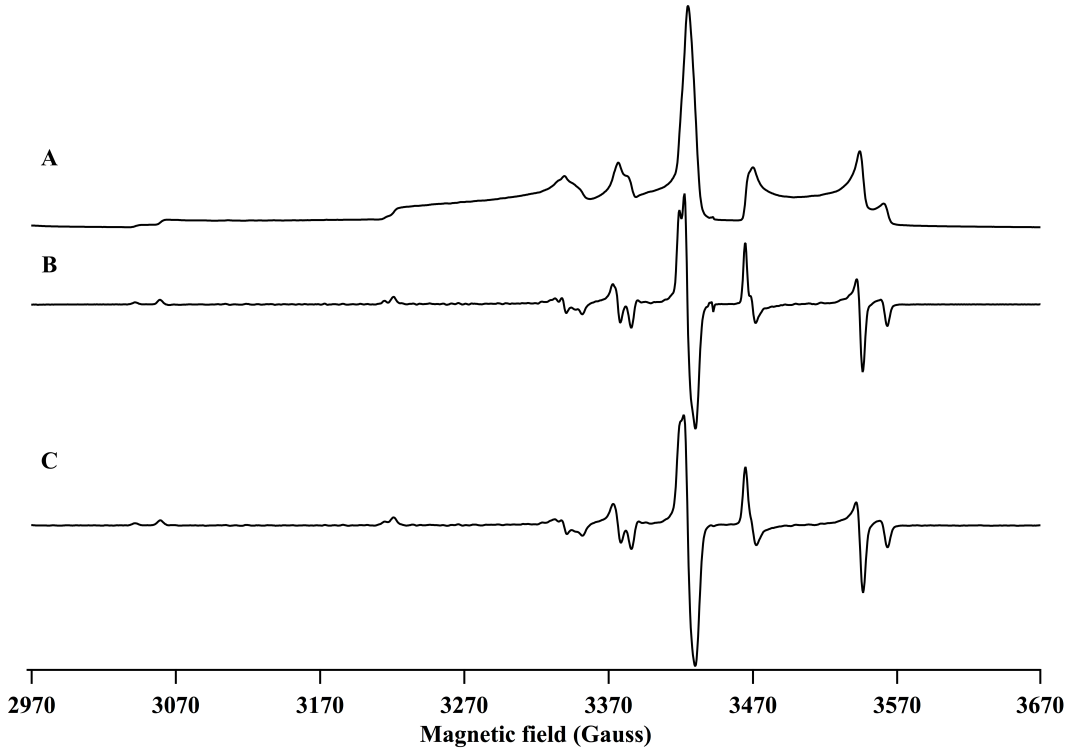

Fig. 4.6 A) Spectrum of Cu^{2+} in $Ni(Et_2dtc)_2$ obtained by field-stepped direct detection in 701 steps over 700 G. Each scan was 11.5 G wide and the linear scan frequency was 5.12 kHz, which corresponds to a scan rate of 118 kG/s. B) The first derivative of the spectrum in part A, and C) the CW spectrum obtained with a modulation amplitude of 1.5 G with 0.5 G field resolution. The B_1 was 17.4 mG for both spectra. Spectra and data reproduced from the original journal article (Yu, Liu et al. 2015).

Spectra of Cu^{2+} in Zn(TTP) (Fig. 4.7) exhibit extensive nitrogen hyperfine splitting in the perpendicular region (Du, Eaton et al. 1996). The field-stepped direct detection spectrum was obtained with 1201 steps over 1200 G (Fig. 4.7A). The first derivative of the field-stepped absorption spectrum (Fig. 4.7B) has well-resolved nitrogen hyperfine splitting that matches well with the CW spectrum (Fig. 4.7C). For the same data acquisition time the *S/N* in the field-stepped spectrum is better than that for the CW spectrum, which provides substantially better definition of nitrogen hyperfine splitting in the parallel region of the spectrum (Fig. 4.7B, 4.7C insets).

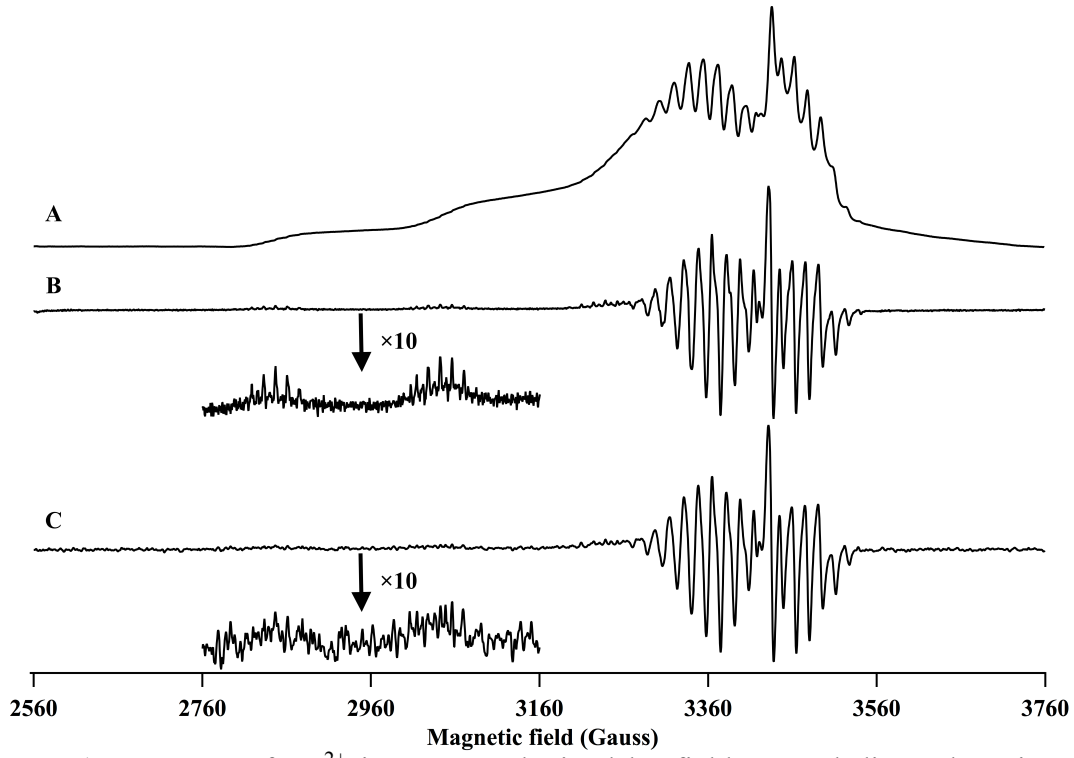

Fig. 4.7 A) Spectrum of Cu^{2+} in ZnTTP obtained by field-stepped direct detection in 1201 steps over 1200 G. Each scan was 11.5 G wide and the linear scan frequency was 5.12 kHz, which corresponds to a scan rate of 118 kG/s. B) The first derivative of the spectrum in part A, and C) the CW spectrum obtained with a modulation amplitude of 1.2 G with 0.5 G field resolution. The insets below traces B and C show the parallel regions of the spectra with the y axis scale expanded by a factor of 10. The B_1 was 17.4 mG for both field-stepped and CW spectra. Spectra and data reproduced from the original journal article (Yu, Liu et al. 2015).

Nitroxide radicals are widely used as probes in biophysical studies. Spectra of PDT immobilized in sucrose octaacetate are shown in Fig. 4.8. The field-stepped direct detection spectrum was obtained with 151 field steps over 150 G (Fig. 4.8A). The numerical derivative of the field-stepped spectrum (Fig. 4.8B) is in good agreement with the CW spectrum (Fig. 4.8C). The resolution of features in the vicinity of 3430 G matches well with previously reported spectra for the same sample (Yu, Tseitlin et al. 2015). This spectral width is small enough that it has been recorded previously in a sinusoidal rapid scan experiment in which the rapid scan encompassed the full spectral width (Yu, Quine et al. 2014). The acquisition of accurate lineshapes for this sample by field-stepped direct detection is a further example of the performance for features that are relatively broad compared with the width of the triangular scans.

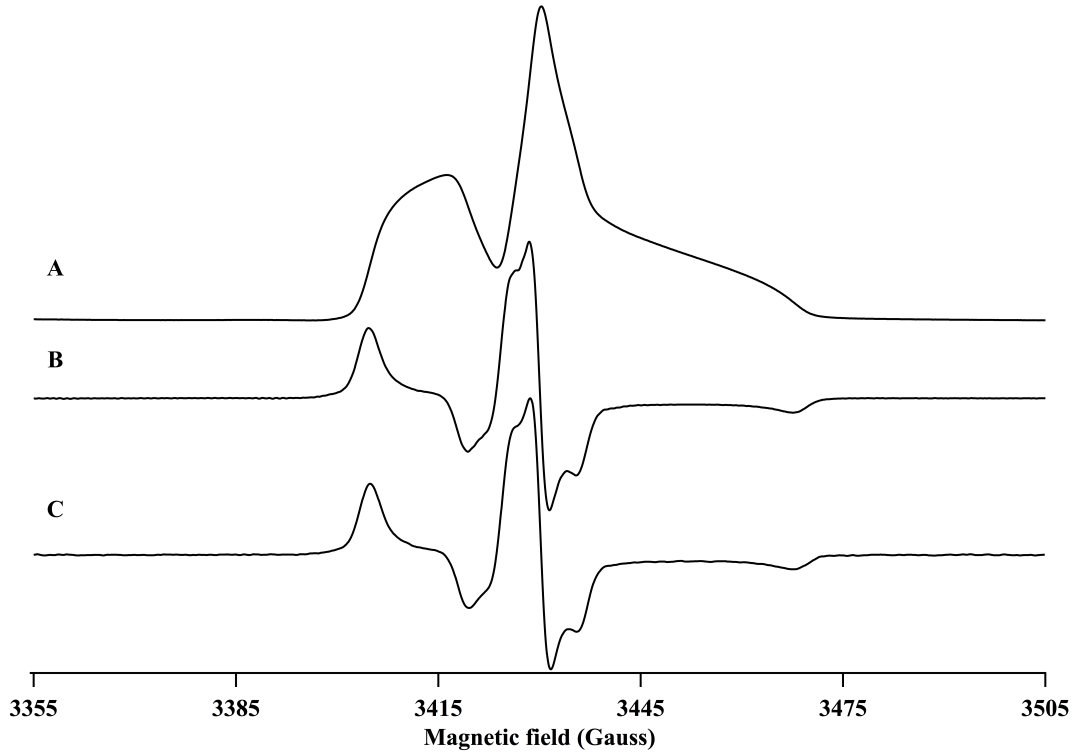

Fig. 4.8 A) Spectrum of nitroxide PDT in sucrose octaacetate obtained by field-stepped direct detection in 151 steps over 150 G. Each scan was 11.5 G wide and the linear scan frequency was 5.12 kHz, which corresponds to a scan rate of 118 kG/s. B) The first derivative of the spectrum in part A, and C) CW spectrum obtained with a modulation amplitude of 0.6 G and 0.1 G field resolution. The B_1 was 17.4 mG for both spectra. Spectra and data reproduced from the original journal article (Yu, Liu et al. 2015).

Spectra of VO^{2+} porphyrins have well-defined features for the hyperfine splitting along both the parallel and perpendicular axes (Du, More et al. 1992). The field-stepped direct detection spectrum was obtained with 1501 steps over 1500 G (Fig. 4.9A). The first derivative of the field-stepped spectrum (Fig. 4.9C) matches well with the CW spectrum (Fig. 4.9C).

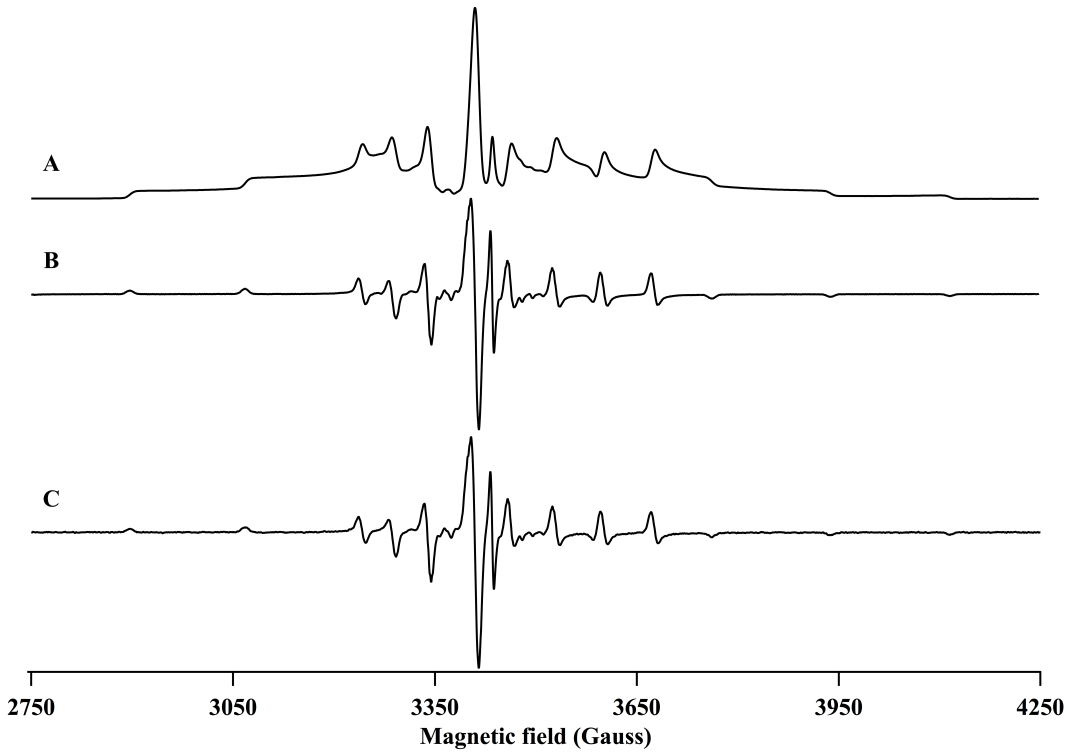

Fig. 4.9 A) Spectrum of VO^{2+} in Zn(TTP-COOH) obtained by field-stepped direct detection in 1501 steps over 1500 G. Each scan was 11.5 G wide and the linear scan frequency was 5.12 kHz, which corresponds to a scan rate of 118 kG/s. B) The first derivative of spectrum in part A, and C) the CW spectrum obtained with a modulation amplitude of 1.1 G with 0.5 G field resolution. The B_1 was 17.4 mG for both spectra. Spectra and data reproduced from the original journal article (Yu, Liu et al. 2015).

EPR spectra of Mn^{2+} are strongly dependent on the symmetry of the local environment and its impact on the zero-field splitting. Spectra of the Mn^{2+} impurity in CaO are shown in Fig. 4.10. Because this environment is close to octahedral, the zero field splitting is small and the powder spectrum consists of six lines due to nuclear hyperfine splitting. The field-stepped direct detection spectrum was obtained with 1201 steps over 600 G (Fig. 4.10A). The 0.5 G field increments were selected to give good definition of the six manganese hyperfine lines, which have 0.7 G peak-to-peak linewidths. A broad underlying signal with $g \sim 2$ is more clearly defined in the absorption spectrum than in the first derivative spectra (Fig. 4.10B, 4.10C). The first derivative of the field-stepped spectrum is in good agreement with the CW spectrum. The integral of the CW spectrum also shows the broad underlying feature. The difference between the first derivative and absorption spectra is a reminder of the extent to which the first-derivative display tends to emphasize sharp features at the expense of broader ones. A sharp low intensity peak at $g \sim 2$ from an organic impurity is observed in all of the spectra. The improved *S/N* for the field-stepped spectrum provides improved definition of the very weak forbidden transitions that fall between the stronger hyperfine lines (insets below trace B and above trace C).

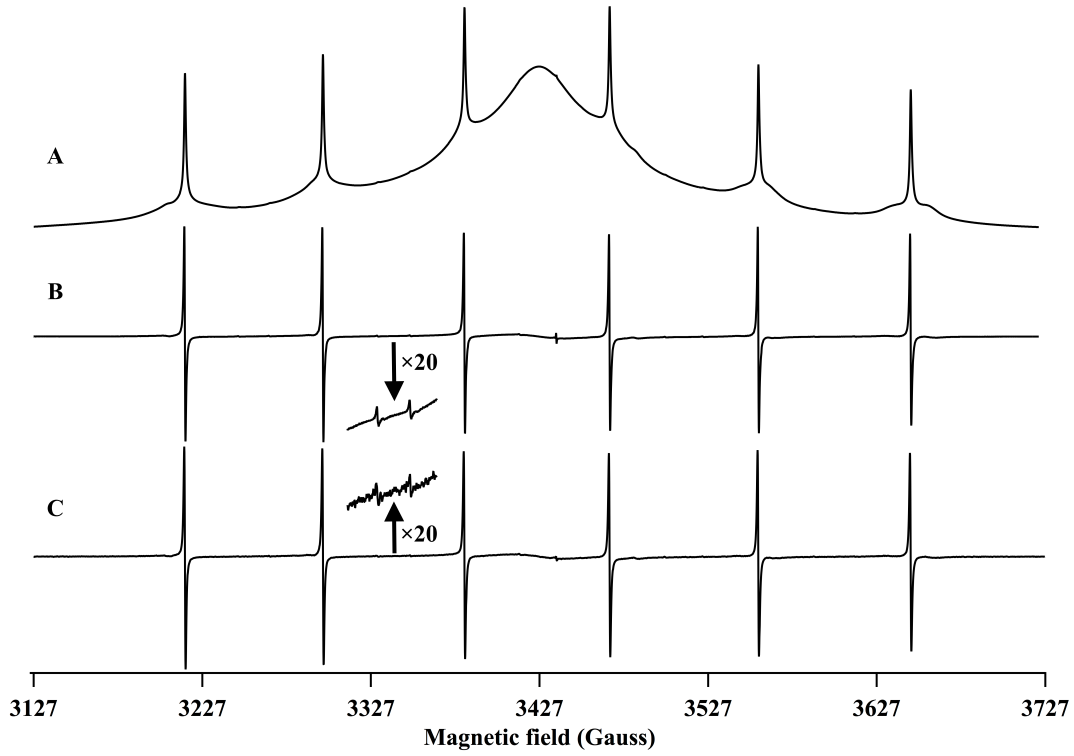

Fig. 4.10 A) Spectrum of Mn^{2+} in CaO obtained by field-stepped direct detection in 1201 steps over 600 G. Each scan was 11.5 G wide and the linear scan frequency was 5.12 kHz, which corresponds to a scan rate of 118 kG/s. B) The first derivative of the spectrum in part A, and C) the CW spectrum obtained with a modulation amplitude of 0.15 G and 0.1 G field resolution. The insets below trace B and above trace C show the forbidden transitions with y axis scales expanded by a factor of 20. The B_1 was 17.4 mG for both spectra. Spectra and data reproduced from the original journal article (Yu, Liu et al. 2015).

The spectrum of Mn^{2+} in a crystal of $Mg(acac)_2(H_2O)_2$ is especially challenging. The zero field splitting is large enough that the spectrum extends over more than 6000 G. The narrowest lines have peak-to-peak linewidths in the first derivative spectrum of about 5 G. The spectrum was strongly orientation dependent. Data obtained for the same orientation of the crystal by field-stepped direct detection or by CW are shown in Fig. 4.11. The field-stepped spectrum was obtained with 6201 steps over 6200 G. A broad feature at low field was well-defined in the field-stepped absorption spectrum.

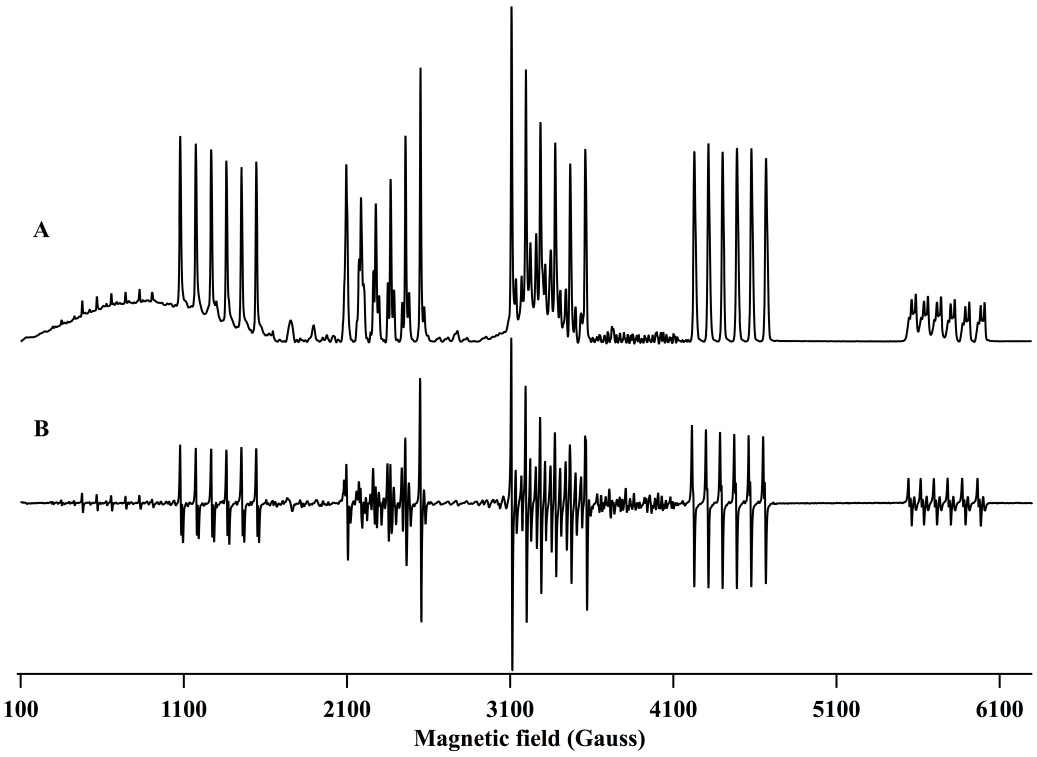

Fig. 4.11 A) Spectrum of an oriented crystal of Mn^{2+} in $Mg(acac)_2(H_2O)_2$ obtained by field-stepped direct detection in 6201 steps over 6200 G. B) CW spectrum obtained with a modulation amplitude of 1.1 G and field resolution of 1.0 G. The B_1 was 174 mG for both spectra. Spectra and data reproduced from the original journal article (Yu, Liu et al. 2015).

The *S/N* for spectra in Fig. 4.6 to 4.11 are summarized in Table 4.1. The samples for which spectra are reported in this chapter were selected to demonstrate the ability of the stepped-field method to accurately record complicated lineshapes. The experimental conditions were selected to give high enough *S/N* that lineshapes were well defined. For most of the spectra the *S/N* is so high that the noise is not well defined, and there is substantial uncertainty in the calculated values of *S/N*. However, the *S/N* advantage of stepped field scan relative to conventional CW is evident (Table 4.1).

Table 4.1 *S/N* Comparisons[a,b,c]

Sample	Figure	Field-Stepped Absorption	Field-Stepped First Derivative	CW
Cu^{2+} in $Ni(Et_2dtc)_2$	6	1.8	1.2	1.1
Cu^{2+} in ZnTTP	7	3.0	0.72	0.30
PDT in sucrose octaacetate	8	11	2.2	1.0
VO^{2+} in Zn(TTP-COOH)	9	13	2.6	1.1
Mn^{2+} in CaO	10	11	8.5	2.3
Mn^{2+} in $Mg(acac)_2(H_2O)_2$	11	11		2.0

[a] *S/N* for the absorption spectra is defined as signal amplitude divided by RMS noise in baseline regions of the spectrum. For the first derivative spectra the *S/N* is defined as the peak-to-peak amplitude divided by RMS noise in baseline regions of the spectrum.
[b] The *S/N* for many spectra is so high that it is difficult to define the RMS noise accurately.
[c] All values are reported in units of 10^3.

4.5 Discussion

The field-stepped direct detection spectra for samples with sweep widths ranging from 2 to 6200 G are in excellent agreement with CW spectra. The spectra include both lines that are narrow or broad relative to the sweep width. This method has several advantages relative to CW spectroscopy, several of which are similar to the advantages of rapid scan (Eaton, Quine et al. 2014). (i) In CW if the modulation amplitude is too large, the signal is broadened. In direct detection field modulation is not used. (ii) In CW the small modulation amplitude detects only a small fraction of the signal amplitude. In direct detection each scan detects a larger fraction of the signal, which improves the *S/N*. (iii) If the scan rate is fast enough to cause rapid scan oscillations, the slow scan spectrum can be recovered by deconvolution after the combination of segments. (iv) The data are acquired with quadrature detection, which permits phase correction in the post processing. (v) In the direct detection method the signal typically is oversampled in the field axis. The appropriate number of points to be averaged to achieve the desired field resolution is determined in post processing, which improves the *S/N*. For many of the spectra shown in the figures, about 100 points were averaged. Very wide triangular or sinusoidal scans lead to large background signals that are due to the effects of the scanning magnetic field (Eaton, Quine et al. 2014). In the direct detected scans the background signal is nearly sinusoidal at the scanning frequency. Additional advantages of the field swept direct detection method is that i) the background signal is much lower for the individual scans than for combined wide spectrum, and ii) the background signals for the individual scans are not coherent with the combined spectrum and tend to average

out similar to noise when repetitive signals are averaged. The residual absorption signal after DC offset correction is slowly varying and monotonic (Fig. 4.5D), similar to backgrounds in CW spectra. The selection of the number of scans and the field increment between scans determines the accuracy with which the field is defined at each point in the spectrum. Combining the signals from separate scans requires accurate alignment of field points from successive scans. This resolution can be improved by interpolation as was demonstrated for the LiPc data.

This method extends the advantages of rapid scan to much wider sweeps than are feasible for a single scan. The widest scans that have been reported for a single rapid scan was 155 G (Yu, Quine et al. 2014). The non-adiabatic rapid sweep method (NARS) of Hyde and co-workers also employs direct detection (Kittell, Camenisch et al. 2011, Kittell, Hustedt et al. 2012, Hyde, Bennett et al. 2013, Kittell and Hyde 2015). The widest scan obtained by that method had a sweep width of 850 G, which was obtained by combining 170 segments of 5 G each (Hyde, Bennett et al. 2013). The segments were combined by aligning only the ends of the segments and the use of a low-pass filter to remove discontinuities created by combing segments. A major advantage of the proposed field-stepped direct detection method is that there are extensive regions of overlap between successive scans, which results in minimum discontinuity between segments. In parallel with the work reported in this chapter, Kittell and Hyde (Kittell and Hyde 2015) reported using overlapping segments.

4.6 Summary

As the scan width increases, the voltage requirement across the resonating capacitor and scan coils increases dramatically and the background signal induced by the rapidly changing field increases. An alternate approach is needed to achieve wider scans. A field-stepped direct detection EPR method that is based on rapid-scan technology is now reported, and scan widths up to 6200 G have been demonstrated. A linear scan frequency of 5.12 kHz was generated with the scan driver described previously. The field was stepped at intervals of 0.01 to 1 G, depending on the linewidths in the spectra. At each field data for triangular scans with widths up to 11.5 G were acquired. Data from the triangular scans were combined by matching DC offsets for overlapping regions of successive scans. A degased lithium phthalocyanine sample was used to demonstrate that the linear deconvolution procedure could be employed with field-stepped direct detection EPR signals. Field-stepped direct detection EPR spectra were obtained for Cu^{2+} doped in Ni(diethyldithiocarbamate)$_2$, Cu^{2+} doped in Zn tetratolylporphyrin, perdeuterated tempone in sucrose octaacetate, vanadyl ion doped in a parasubstituted Zn tetratolylporphyrin, Mn^{2+} impurity in CaO, and an oriented crystal of Mn^{2+} doped in Mg(acetylacetonate)$_2$(H_2O)$_2$.

CHAPTER 5

DIGITALLY GENERATED EXCITATION AND NEAR-BASEBAND QUADRATURE DETECTION OF RAPID SCAN EPR SIGNALS

5.1 Introduction

Recent advances in AWG and fast digitizers make it possible to build EPR spectrometers with digital source and detection, which can provide greater flexibility in experimental design and operating frequency than current generation spectrometers. The transition from analog to digital was crucial to improving NMR (Hornung 2011), microwave spectroscopy (Brown, Dian et al. 2006, Brown, Dian et al. 2008, Neill, Douglass et al. 2011), and ion cyclotron resonance (Blakney, Hendrickson et al. 2011), and similar advantages await in EPR.

The work reported in this chapter was performed in close collaboration with Mark Tseitlin (Tseitlin, Yu et al. 2014). The theory was developed by Mark Tseitlin. Experiments were performed by this author. Data analysis was performed jointly.

CW EPR obtained by phase sensitive detection at a modulation frequency records only the first-derivative of the absorption spectrum. However, there are multiple advantages to capturing the signal in quadrature. (i) The dispersion signal can, in principle, be combined with the absorption to improve *S/N* of CW spectra. (ii) The dispersion signal saturates less readily than the absorption spectrum so it can be used to

record spectra of readily saturated spin systems (Gaffney and Silverstone 1993, DeRose and Hoffman 1995). (iii) In rapid-scan experiments the quadrature signal is used for removal of the periodic background signal and deconvolution (Tseitlin, Czechowski et al. 2009), and has been shown to improve *S/N* (Tseitlin, Quine et al. 2010). These applications of the quadrature signal work better if the phases in the two channels are strictly orthogonal and the relative intensities are matched. In an ideal quadrature EPR signal, real and imaginary components can be transformed to each other with the use of Kramers–Kronig relations. The digital system described permits reconstruction of an ideal quadrature signal.

The major challenge for signal digitization at an intermediate frequency (*IF)* is the presence of a reflected or transmitted non-EPR component at the excitation frequency, even if the resonator is carefully tuned. This component may be much stronger than the EPR signal. In the conventional baseband detection method, the non-EPR signal is removed by filtering, but to obtain a quadrature signal two detection channels are required, and it is difficult to obtain ideal orthogonality between the channels (Tseitlin, Quine et al. 2010). A general theory is described for detection at an intermediate frequency that is close to baseband and less than the scan or modulation frequency. This allows filtering out the non-EPR component, which otherwise would overwhelm the digitizer, without compromising the absorption and dispersion components of the EPR signal. The approach is general for CW, multiharmonic (Tseitlin, Eaton et al. 2011), and rapid scan EPR (Tseitlin, Czechowski et al. 2009, Tseitlin, Rinard et al. 2011, Eaton, Quine et al. 2014) because these all involve periodic signals. For conventional CW the

only frequency of interest is the modulation frequency, ω_{mod}, for which the amplitude would be found for each field position in the spectrum. For multi-harmonic spectroscopy, the Fourier coefficients of as many as 10–20 harmonics of ω_{mod} would be determined for each field position. Experimental results are reported for the rapid scan method at X-band, which requires a larger number of harmonics of the scan frequency, ω_{scan}, to obtain accurate spectral line shapes than is required for CW EPR. Unlike conventional CW EPR, phase sensitive detection at the modulation frequency is not used in rapid scan EPR.

5.2 Theory

The signal in an EPR spectrometer after the mixer and before analog filtering can be expressed mathematically as:

$$s(t) \propto [\{r_y + m_y(t)\} \sin(\omega_0 t) + \{r_x + m_x(t)\} \cos(\omega_0 t)] \cos(\omega_0 t + \omega_{IF} t + \varphi) \qquad (5.1)$$

where m_x and m_y are the rotating frame components of the net EPR magnetization in-phase and 90° out-of-phase with one circularly polarized component of B_1, r_x and r_y are the components of the non-EPR reflection or transmission signal, ω_0 is the excitation frequency, ω_{IF} is an intermediate frequency to which ω_0 is down-converted, and φ is an adjustable phase setting.

B_1 in the rotating frame is defined to be along the x axis. Multiplication by $\cos(\omega_0 t + \omega_{IF} t + \varphi)$ in Eq. 5.1 represents the analog mixing of the resonator output with a reference, which produces signals at $2\omega_0 + \omega_{IF}$ and at ω_{IF}.

Eq. 5.1 can be used to describe three types of signal detection: (i) baseband detection if $\omega_{IF} = 0$, as is conventionally used in EPR spectrometers; (ii) detection at the excitation frequency with post-processing in a computer, which can be represented with Eq. 5.1 by deletion of the $\cos(\omega_0 t + \omega_{IF} t + \varphi)$ term; or (iii) down-converting the signal to an intermediate frequency, ω_{IF}.

5.2.1 Conventional detection at baseband

The standard EPR bridge employs phase sensitive detection at baseband (method i). This is achieved by mixing with a reference at ω_0. The mixing produces signals at two frequencies, baseband and $2\omega_0$. The latter is filtered out by a low-pass filter. For example, substitution of $\omega_{IF} = 0$ and $\varphi = 0$ into Eq. 5.1 shows that the signal $\{r_y + m_y(t)\}$ is lost as the result of baseband detection and filtering:

$$\{r_y + m_y(t)\}\sin(\omega_0 t)\cos(\omega_0 t) \propto \{r_y + m_y(t)\}\sin(2\omega_0 t) \xrightarrow{\text{Low-Pass Filter}} 0. \quad (5.2)$$

The signal r_x becomes a DC offset that is removed by the high-pass filter. The removal of r_x is possible due to the separation of the lowest frequency component of the periodic EPR signal from DC in the frequency domain. In the standard CW experiment the only component is at ω_{mod}. In a rapid scan experiment the lowest frequency component of the signal is at ω_{scan}. Both ω_{scan} and ω_{mod} typically are in the kHz range.

In a conventional spectrometer either $m_x(t)$ or $m_y(t)$, or a mixture, is detected. To enable detection of the second component, the signal is split into two physically independent channels and the phase of the reference signal (φ) for one of the channels is

shifted 90°. This is equivalent to changing $\cos(\omega_0 t)$ to $\sin(\omega_0 t)$ in Eq. 5.1 (and using $\omega_{IF} = 0$). By analogy to Eq. 5.2, $\{r_x + m_x(t)\}$ is removed by baseband detection. Combination of the components from the two channels generates a complex quadrature signal:

$$c(t) = m_x(t) + j\lambda[m_x(t)\cos\varphi - m_y(t)\sin\varphi] \,, \tag{5.3}$$

where λ is a real number describing the difference in gain between the two physical channels that are nominally in quadrature. If the two channels are perfectly matched, λ = 1, $\varphi = -90^o$, and $c(t)$ is an ideal quadrature signal. For a real phase shifter, φ changes with frequency and for real hardware λ is not exactly 1.

5.2.2 Detection at ω_0

For detection at the excitation frequency (method ii) a mixer is not used (Tseitlin, Quine et al. 2011), and the $\cos(\omega_0 t + \omega_{IF} t + \varphi)$ term in Eq. 5.1 is omitted. This method has the advantage of reducing the number of components in the bridge, and produces undistorted quadrature signals. A single physical channel that carries $s(t)$ is digitized and separation of $m_x(t)$ from $m_y(t)$ is carried out in a computer by means of digital phase-sensitive detection. For CW, multiharmonic, or rapid scan experiments the RF or microwave power is on continuously and a very intense reflection:

$$r(t,\omega) = r_y \sin(\omega t) + r_x \cos(\omega t), \quad \omega = \omega_0 \,, \tag{5.4}$$

has to be digitized along with the EPR component (Ahmad, Som et al. 2010). Because of a very small separation in the frequency domain, ω_0 vs. $\omega_0+\omega_s$, filtering of the unwanted signal is not possible. For CW $\omega_s = \omega_{mod}$ and for rapid scan $\omega_s = \omega_{scan}$. These frequencies

typically are orders of magnitude smaller than ω_0. In addition, method (ii) requires a digitizer with sampling rate that is sufficient to avoid aliasing. The sampling rate can be reduced by time-locked sub-sampling (band-pass sampling) (Hyde, Camenisch et al. 2005), but the bandwidth of the digitizer still must exceed the signal bandwidth, which is of the order of $\omega_0/2\pi$. This method also requires processing very large amounts of data, which becomes less practical at high frequencies such as X-band.

5.2.3 Detection at ω_{IF} that exceeds signal bandwidth.

In method (iii) the microwave signal is translated to an intermediate frequency before detection. The sampling rate requirement for the digitizer can be reduced enough to just satisfy the Nyquist criterion for the signal after downconversion to the *IF*, which reduces the amount of data to be processed. Detection at an *IF* also has the advantage that the digitized signal can be processed to obtain both m_x and m_y signals. To permit quadrature detection, ω_{IF} traditionally is selected to be larger than all frequency components of the signal. As was noted for method (i), there are strong reflected signals $r(t,\omega_{IF})$ (Eq. 5.4), which may overwhelm the digitizer and limit the dynamic range available for the EPR signal. Because $r(t,\omega_{IF})$, $m_x(t)$ and $m_y(t)$ are very close in the frequency domain, the reflected signal cannot be removed by filtering.

5.2.4 Detection at near baseband ω_{IF}

A method is demonstrated to remove the strong reflected signals without compromising the EPR signal, which uses ω_{IF} that is small relative to the fundamental frequencies ω_{mod} or ω_{scan} (Eq. 5.5). Mixing with $\omega_0 + \omega_{IF}$ (Eq. 5.1), where ω_{IF} is near baseband,

$$0 < \omega_{IF} << \omega_s \quad , \quad \text{where } \omega_s \text{ is either } \omega_{scan} \text{ or } \omega_{\mathrm{mod}} \tag{5.5}$$

generates signals at $2\omega_0 + \omega_{IF}$ and at ω_{IF}. Low-pass filtering removes the components at $2\omega_0 + \omega_{IF}$. The non-EPR reflection $r(t,\omega_{IF})$ is now sufficiently well separated from the EPR signal in the frequency domain, that it can be removed by a high-pass filter before digitizing. This down-conversion to *IF* and analog filtering modifies the EPR signal described by Eq. 5.1, into one that is described by Eq. 5.6.

$$s(t) \propto -m_y(t)\ \sin(\omega_{IF}t) + m_x(t)\ \cos(\omega_{IF}t) \tag{5.6}$$

which preserves both $m_y(t)$ and $m_x(t)$, and therefore, can be post-processed to obtain $c(t)$ with $\lambda = 1$ and $\varphi = -90^{o}$ (Eq. 5.3). Transformation of real $s(t)$ into complex quadrature $c(t)$ (Eq. 5.3) is described in detail below.

To see the relationships between the coefficients in Eq. 5.6 and the coefficients after Fourier transformation, the sine and cosine functions can be replaced by complex exponents

$$\begin{cases} \cos(\omega_{IF}t) = \{\exp(j\omega_{IF}t) + \exp(-j\omega_{IF}t)\}/2, \\ \sin(\omega_{IF}t) = -j\{\exp(j\omega_{\mathrm{IF}}t) - \exp(-j\omega_{\mathrm{IF}}t)\}/2 \end{cases},$$

to give, after rearrangement,

$$s(t) \propto c(t)\ \exp(j\omega_{IF}t)\ +\ \bar{c}(t)\ \exp(-j\omega_{IF}t)\ , \tag{5.7}$$

where $\bar{c}(t)$ denotes the complex conjugate of $c(t)$. Fourier transformation of Eq. 5.6 or 5.7 gives:

$$S(\omega) \propto C(\omega + \omega_{IF}) + \overline{C}(-\omega - \omega_{IF}), \tag{5.8}$$

in the frequency domain, where $C(\omega)$ is the Fourier transform of $c(t)$. The $c(t)$ in Eq. 5.7 describes a periodic quadrature response to sinusoidal variation of the external magnetic field:

$$c(t) = m_x(t) + jm_y(t) = \sum_{n=-N}^{N} C_n \exp(jn\omega_s t)\ . \tag{5.9}$$

In Eq. 5.9 C_n are the complex Fourier coefficients and N is the number of detectable harmonics in the EPR signal. Using Eq. 5.9, Eq. 5.8 can be rewritten as follows:

$$S(\omega) \propto \sum_{n=-N}^{N} C_n \delta(\omega - n\omega_s - \omega_{IF}) + \sum_{n=-N}^{N} \overline{C}_n \delta(\omega + n\omega_s + \omega_{IF}), \tag{5.10}$$

where $\delta(\omega)$ is the delta-function. In Eq. 5.10 ω is a continuous variable because $S(\omega)$ is obtained by Fourier transformation of the continuous infinite signal $s(t)$. Periodic signals measured in an experiment are discretely digitized and have finite duration. Data processing requires Discrete Fourier transformation to give $S(\omega)$ in the discrete form $S(\omega_m)$. The range for the integer number m and the frequency increment depend on the sampling rate and signal period. When the periodic signal is measured at baseband, the period for averaging is the same as the scan period:

$$P_{aver} = P_s = 2\pi/\omega_s, \tag{5.11}$$

For detection with ω_{IF} near baseband, the selection of the averaging period is not arbitrary. Averaging only works if $s(t)$ is periodic. To ensure periodicity, and therefore to enable averaging, the following constraints must be imposed:

$$P_{aver} = kP_s = lP_{IF}. \tag{5.12}$$

In Eq. 5.12 P_{aver} is the period to be averaged, P_{IF} is the period of the intermediate frequency, k and l are positive integer numbers. To permit signal averaging without discontinuities, if down-conversion is done to a near baseband intermediate frequency (see Eq. 5.5), it is convenient to choose ω_s to be an integer multiple of ω_{IF}:

$$\omega_s = K\omega_{IF}. \tag{5.13}$$

In this case the averaged signal period becomes equal to the *IF* period, with $l = 1$ in Eq. 5.12:

$$P_{aver} = P_{IF} = KP_s \tag{5.14}$$

and the frequency increment for discrete $S(\omega_{\text{m}})$ is ω_{IF}. As a result, Eq. 5.10 can be transformed to:

$$S_m = S(m\omega_{IF}) \propto \sum_{n=-N}^{N} C_n \delta(m - nK - 1) + \sum_{n=-N}^{N} \overline{C}_n \delta(m + nK + 1) \tag{5.15}$$

In Eq. 5.15 the delta function was changed to a discrete unit function: $\delta(0) = 1$ and $\delta(m \neq 0) = 0$. Because $s(t)$ is a real function,

$$S_m = \overline{S}_{-m}, \tag{5.16}$$

which means that the coefficients for the positive and negative frequencies contain the same information.

Data analysis in the frequency domain can be done using only the non-negative frequencies:

$$S_m \propto \sum_{n=-N}^{N} C_n \delta(m - nK - 1) + \sum_{n=-N}^{N} \overline{C}_{-n} \delta(m - nK + 1), m \geq 0 \tag{5.17}$$

The summation order in the second term in Eq. 5.17 was reversed by changing the subscript on the coefficient to -n. If $K > 2$, Eq. 5.17 allows for separate determination of Fourier coefficients C_n for negative and positive frequencies:

$$\begin{cases} C_n = S_{nK+1} \\ C_{-n} = \overline{S}_{nK-1} \end{cases}, \quad n \geq 0 \tag{5.18}$$

When the coefficients C_n are found, inverse Fourier transformation gives the EPR signal in complex quadrature form $c(t)$. This is the signal for a single period that would have been obtained by detection at baseband with balanced quadrature channels. In Eq. 5.18 some points in S are not used to find C_n and C_{n-1}, but in the experimental data these points include only noise. For example, for $K = 8$ the points S_1, S_2, … S_6, and S_8 are not used. Omitting these points improves the *S/N* and is equivalent to averaging K cycles of P_s. Since the signal is periodic and the noise is not, the signal only contributes at $(nK \pm 1)\omega_{IF}$.

5.2.4.1 Rapid scan with f_{IF} = 5 kHz, K = 8.

To understand the steps in the data analysis it is useful to consider a specific case (Fig. 5.1). The following rapid scan example is given for f_{IF} = 5 kHz ($f = \omega/2\pi$), which is the frequency that was used for the experiments. For K = 8, f_{scan} = 40 kHz (Eq. 5.13). Fig. 5.1a is a graphical representation of the S coefficients in Eq. 5.18, in the linear frequency domain. The data consist of pairs of components with frequencies of 40 ± 5, 80 ±5 kHz, etc. For example with n = 1 (Eq. 5.18), $C_1 = S_9$, and for the example shown, C_9 is the Fourier coefficient at 9 times *IF*. Similarly the complex conjugate of C_{-1} is equal to S_7, at 7 times *IF* (Fig. 5.1a). The complex conjugates of S_{nK-1} are taken, and the results are moved to the corresponding negative frequencies (Fig. 5.1b). All frequencies are then shifted by one unit of *IF* (Fig. 5.1c) such that the data are now centered at 0. The signal-containing points are now positioned at nK, ($n \neq 0$). All other points contain noise. The subarray of signal-containing points is extracted to generate a new array that is $1/8^{th}$ as long. This array is Inverse Fourier transformed to produce one full cycle of the complex baseband rapid scan signal.

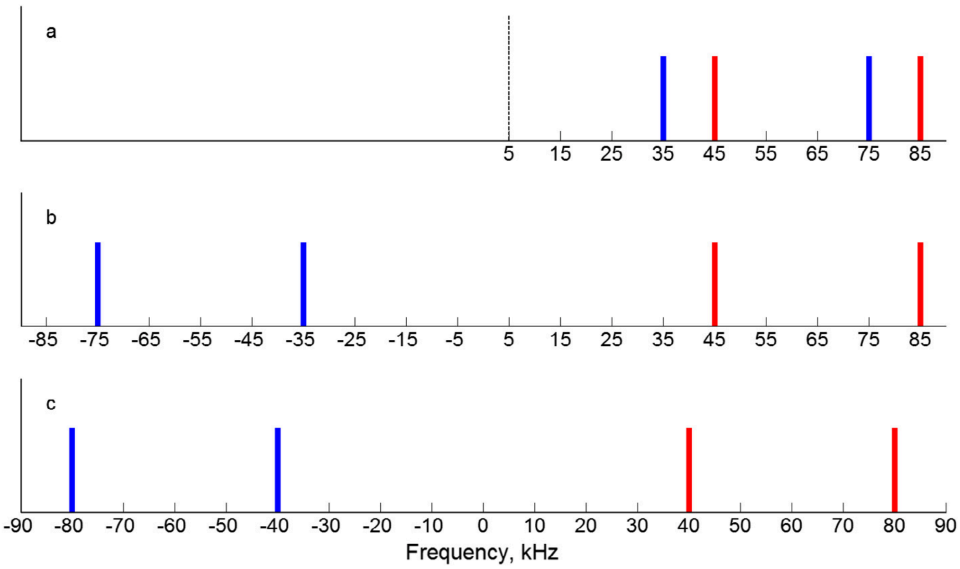

Fig. 5.1 Graphical description of the algorithm for f_{IF} = 5 kHz and K = 8 (Eq. 5.13), showing only the first two harmonics. (a) Fourier transform of the *IF* signal (Eq. 5.15). The Fourier coefficients for negative and positive frequencies are interdependent, so that only positive frequencies are used. Red and blue colored bars represent S_{nK+1} and S_{nK-1} coefficients in Eq. 5.17. The black dashed line denotes the position of the strong 5 kHz signal that was filtered out. (b) The complex conjugates of S_{nK-1} coefficients are taken and mirror-inverted into the negative half of the frequency domain. (c) All coefficients are shifted in the negative direction by 5 kHz. The result is the Fourier transform of the complex quadrature signal $c(t)$ (Eq. 5.9). Diagram reproduced from the original journal article (Tseitlin, Yu et al. 2014).

5.3. Experimental section

5.3.1 Samples

A small particle of 1,3-bisdiphenylene-2-phenylallyl (BDPA, Sigma-Aldrich, St. Louis, Missouri) in air in a capillary tube was supported in a 4 mm O.D. quartz tube. Tris[8-carboxyl-2,2,6,6-benzo(1,2-d:5-d)-bis(1,3)dithiole-4-yl] methyl sodium salt (trityl OX63) (Ardenkjaer-Larsen, Laursen et al. 1998) was provided by Professor Howard Halpern, University of Chicago.

A 0.2 mM aqueous solution of trityl OX63 in a 4 mm O.D. × 3 mm I.D. quartz tube had a height of 3 to 4 mm. The sample was purged with N_2 for 5 min and then flame sealed. The sample reduced the resonator Q to about 60.

Nitroxide ^{15}N-PDT was purchased from CDN isotopes (Quebec, Canada). A 6 mM solution of ^{15}N-PDT in water was mixed with superabsorbent polymer SAP (cross-linked polyacrylate sodium salt, Sigma-Aldrich #436364) in a 10:1 mass ratio. Super-absorbent polymers (SAP) consist of cross-linked polyacrylic acid or polyacrylate salts. These polymers can absorb a large amount of water relative to the volume of the polymers. When an aqueous solution is mixed with SAP, a gel is formed. The pH of the gel can be adjusted to pH ~5 by using a buffered solution. Samples in 1 mm capillary tubes were sealed in air with a torch and monitored by X-band EPR for more than 500 days. A capillary supported in 4 mm O.D. quartz tube reduced the resonator Q to about 225. The stability of these pH-controlled samples is good for long-term use.

^{15}N-mHTCPO was provided by Prof. Halpern, University of Chicago (Lin, Teicher et al. 1990). A 0.1 mM solution of ^{15}N-mHTCPO in 80/20 EtOH/H_2O in a 4 mm

O.D. × 3 mm I.D. quartz tube had a height of 3 mm, resulting in 3 × 3 mm cylindrical shape, which reduced the resonator Q to about 150 (Mitchell, Quine et al. 2012). The sample was degassed by six freeze–pump–thaw cycles and then flame sealed.

5.3.2 Hardware

The digital rapid scan EPR system is built around a Bruker E500T spectrometer with a Bruker X-band Flexline ER4118X-MD5 dielectric resonator (Mitchell, Quine et al. 2012, Mitchell, Tseitlin et al. 2013). For low-loss samples the resonator Q is about 9000 and the efficiency is 3.8 $G/W^{1/2}$ (Mitchell, Tseitlin et al. 2013). The resonator efficiency decreases approximately as $\sqrt{Q}$ (Mitchell, Tseitlin et al. 2013). The Xepr software controls the magnetic field, and data are digitized with a Bruker SpecJet II digitizer, which has a sampling rate up to 1 GHz. The sinusoidal scans are generated with the recently described scan driver (Quine, Mitchell et al. 2012). The scan coils are constructed from 200 turns of Litz wire (255 strands of AWG44 wire). The coils have about 7.6 cm average diameter and were placed about 4 cm apart. The coil constant is 37.7 G/A (Quine, Mitchell et al. 2012). Mounting the coils on the magnet, rather than on the resonator, reduces the oscillatory background signal induced by the rapid scans. The placement of highly conducting aluminum plates on the poles of the Bruker 10" magnet reduces resistive losses in the magnet pole faces that arise from induced currents. The dielectric resonator decreases eddy currents induced by the rapidly-changing magnetic fields relative to resonators with larger amounts of metal.

The block diagram of the system is shown in Fig. 5.2. The source is a Tektronix arbitrary waveform generator (AWG 70002A) with two 8-bit DAC outputs at 25 Gsamples/s, which permits generating waveforms with 2.5 samples/cycle at 10 GHz. Amplifiers in the signal path give a maximum microwave power of 235 mW. An adjustable attenuator (0 to 50 dB) controls the power to the resonator. The signal from the resonator, after amplification, is mixed with the amplified signal from the second AWG DAC channel. The frequency difference between the two synchronized microwave outputs from the AWG creates the approximately 5 kHz *IF*. A high pass filter at 25 kHz (-3dB) removes the non-EPR signal at the intermediate frequency, but preserves the spectral information that is in the harmonics. After an additional 20 dB gain and a 5 MHz low pass filter (Krohn-Hite 3955 LP Butterworth dual-channel filter) that is set to remove high frequency noise, the signal is detected in the Bruker SpecJet II digitizer. The timing of the data acquisition was synchronized by an external clock signal from the AWG. To generate the sinusoidal rapid scans a square-wave marker signal from the AWG was converted to a sine wave by a low pass filter (at 29 kHz). The period of the rapid scans was exactly 1/8 of the period for the *IF*. The scan coils are resonated with a capacitor (Quine, Mitchell et al. 2012). Timing of the excitation frequency, reference frequency, *IF*, and rapid scan cycles were selected to give integer numbers of cycles for each frequency. The timing diagram for the signals from the AWG is shown in Fig. 5.3 for a particular example.

The experimental signal was passed through a 4-pole high-pass Butterworth filter to remove the component at the *IF*, with minimum impact on higher frequencies that

contain EPR signal. The amplitudes of frequency components of the EPR signal were preserved, but the filter introduces frequency-dependent phase shifts. The Butterworth filter was designed with "Filter Lite" software from Nuhertz Technologies, Phoenix, AZ. The software outputs tabular data describing the impact of the filter on the phase and amplitude of the frequency components of the signal which was stored in the data reconstruction program. The corrections were read from the stored file and applied to the data, prior to the data reconstruction described in section 5.2.4.1.

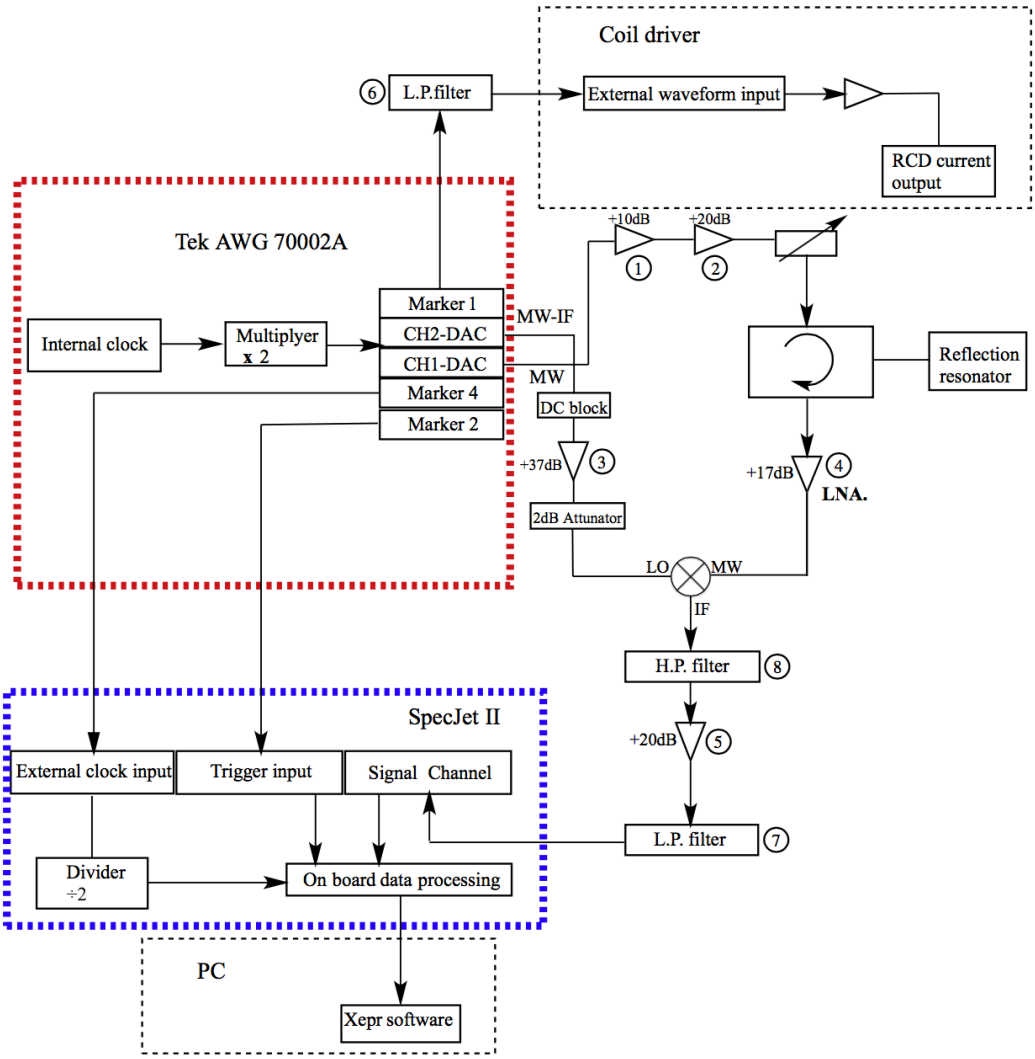

Fig. 5.2 Block diagram for digital EPR spectrometer. KH refers to a Krohn-Hite 3955 LP Butterworth dual-channel filter. (1) microwave power amplifier: Mini circuits ZX60-14012L-S+; (2) microwave power amplifier: Aydin AWA 8596B; (3) microwave power amplifier: MITEQ AMF 4s 9092-20; (4) low noise amplifier: HD27028, noise figure = 1.8 dB; (5) amplification in KH filter; (6) low pass filter with a cutoff frequency of 29 kHz; (7) low pass filter with a cutoff of 5 MHz; (8) 4 pole high pass Butterworth filter (~3 dB) at 25 kHz. This proof-of-principle experiment was conducted with available components. The design has not been optimized. Diagram reproduced from the original journal article (Tseitlin, Yu et al. 2014).

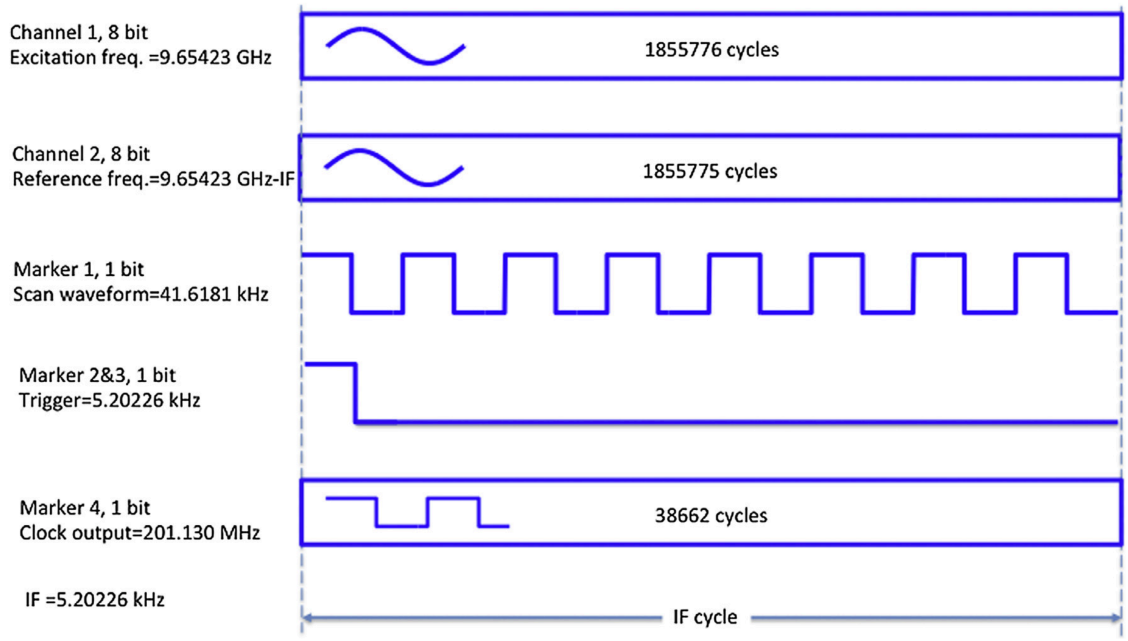

Fig. 5.3 Timing details for AWG outputs. The synchronization of the five outputs from the AWG is sketched for a sampling frequency of 24.135575 Gs/s. The timing is selected to have an integer number of cycles for each output. The lengths of the outputs from channels 1 and 2 differ by 1 cycle, which corresponds to the *IF*. The output from marker 1 is sent through a low-pass filter with a cutoff of 29 kHz frequency to convert the square wave into a sine wave that generates the sinusoidal rapid scan. The scan frequency is exactly 8 times *IF*. Marker 2 synchronizes the SpecJet II digitization, and marker 3 triggers the oscilloscope. The clock output provides the external clock signal for the Specjet II. For the examples shown in this chapter, the *IF* was about 5 kHz. The exact value of *IF* changes with resonator tuning because that changes the excitation frequency. Diagram reproduced from the original journal article (Tseitlin, Yu et al. 2014).

5.3.3 Resonator tuning and data acquisition

5.3.3.1 Resonator tuning

With the AWG 70002A a chirp pulse waveform from 9.6 to 9.7 GHz was generated in channel 1 DAC as the excitation and a continuous waveform at 9.6 GHz was generated in channel 2 DAC as the reference. The signal after the mixer is detected with a LeCroy 400 MHz digital scope (model 44Xi-A). In the scope, a Fourier transform was applied to convert the signal from time domain to frequency domain. The resonator reflection dip in the frequency domain was displayed on the scope, in essentially real time. The resonator was adjusted to critical coupling. The actual resonator frequency, relative to the reference, is read from the scope display and used to program the outputs from the AWG.

5.3.3.2 Data acquisition

The AWG is programmed to output continuous waveforms for the excitation and reference and an example of MATLAB program is shown in Appendix B. The waveforms were designed in MATLAB and transferred to the AWG. The excitation microwave frequency was matched with the resonator, with a clock rate that is 2.5 times the resonator frequency. For a frequency of about 9.6 GHz, a difference of exactly one cycle between the number of cycles for the excitation and the reference frequencies corresponds to a difference of about 5 kHz, which is then the *IF* (Fig. 5.3). The rapid scans were generated with a frequency that is exactly 8 times the *IF*. The trigger for the digitizer occurs once per *IF* period. The AWG also provides the clock signal at about

200 MHz for the SpecJet II. Within the SpecJet II the clock frequency is divided by two, so the digitization occurs at about 100 MHz. The frequencies are exactly synchronized by the AWG and all frequencies shift proportionately with the resonator frequency. Data were acquired on and off resonance.

5.3.4 Data analysis

The data analysis process is outlined in Fig. 5.4. The experimental signal is average with a time window equal to 1/*IF* (Fig 5.5a). The off-resonance signal that contains only unwanted information, including digital clutter, is subtracted from the on-resonance signal. The high pass filter introduces known phase shifts that can be corrected in post-processing using the known characteristics of the filter (section 5.3.2). The data are Fourier transformed into the frequency domain. Analysis as described in section 5.2.4.1 reconstructs the quadrature-detected rapid scan spectrum in the time domain (Fig. 5.5b). Deconvolution generates the absorption spectra in the field domain, from the quadrature rapid scan signal (Fig. 5.5c). The n = 0 term (Eq. 5.9) is the DC offset of the signal and is generated in the baseline correction procedure (Tseitlin, Mitchell et al. 2012). An example of the MATLAB program is shown in Appendix B.

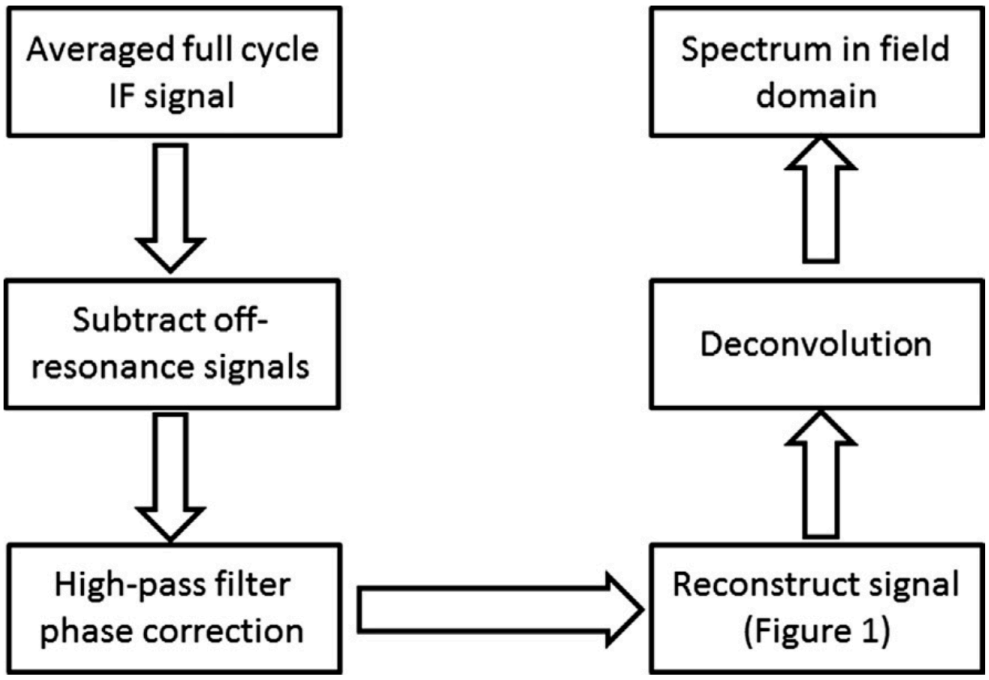

Fig. 5.4 Schematic sequence of data analysis as described in the text. Diagram reproduced from the original journal article (Tseitlin, Yu et al. 2014).

5.3.5 Spectroscopy

The performance of the digital spectrometer has been tested with four samples. Solid samples of BDPA in air have Lorentzian lineshapes with first derivative peak-to-peak widths of 0.4 to 0.8 G and $T_1 \sim T_2$ in the range of 80 to 160 ns (Mitchell, Quine et al. 2011). These relaxation times are sufficiently short that rapid-scan passage effects are not observed for the 40 kHz 10 G scans used in this study. Rapid scan data for the full 8 sinusoidal cycles at 40 kHz that occur within one *IF* period are shown in Fig. 5.5a.

The relative contributions of m_x and m_y change sinusoidally in the course of an *IF* cycle. These data contain both the real and imaginary signals, which are reconstructed by the data analysis algorithm. After reconstruction, a time-domain full cycle rapid scan signal including both the real and imaginary components is obtained as shown in Fig. 5.5b. Averaging up- and down-cycles and combining real and imaginary produces the absorption spectrum in the field domain, as shown in Fig. 5.5c. The full-width at half height of 1.3 G is in reasonable agreement with the expected linewidth (Mitchell, Quine et al. 2011). The signal-to-noise is excellent for this strong sample.

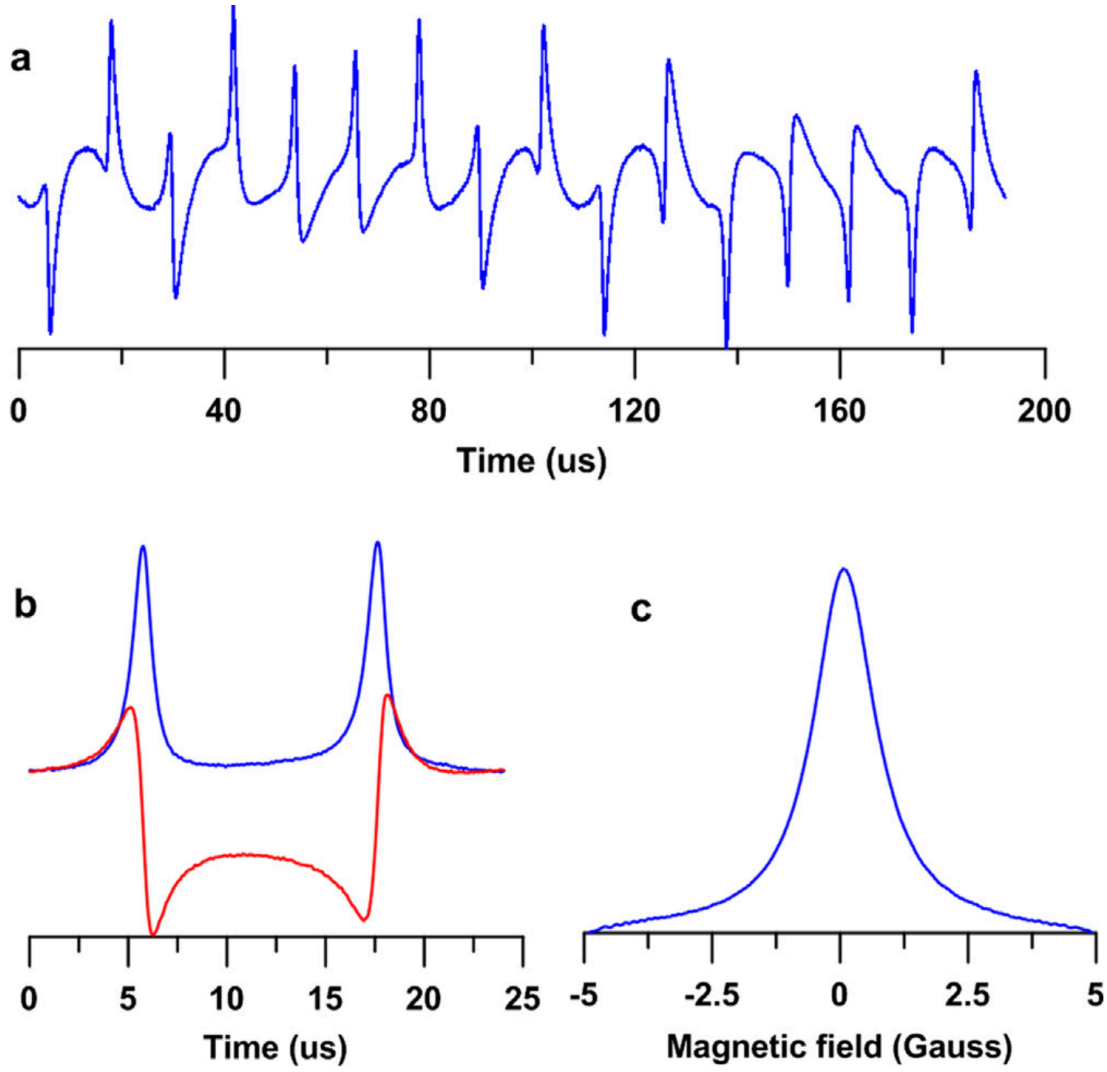

Fig. 5.5 X-band rapid-scan data for solid BDPA in air. (a) Experimental data for the time corresponding to one *IF* cycle obtained with power = 0.6 mW (B_1 ~ 90 mG) and 102400 scans, which required about 20 s. One *IF* cycle encompasses 16 passages through resonance, including both the up-field and down-field sinusoidal scans. (b) Reconstructed quadrature-detected rapid scan spectrum including both up and down scans – real (blue) and imaginary (red). (c) Deconvolved field-domain spectrum. Spectra and data reproduced from the original journal article (Tseitlin, Yu et al. 2014).

At X-band 0.2 mM trityl-OX63 in deoxygenated water has T_1 = 15 μs and T_2 = 5.4 μs (Owenius, Eaton et al. 2005). These relaxation times are long enough that the signal exhibits rapid-scan oscillations when a 40 kHz, 10 G scan width is used. These oscillations are captured accurately in the digital scans (Fig. 5.6a). In the deconvolved spectrum (Fig. 5.6b) the ^{13}C hyperfine lines with splittings of 2.4 and 3.4 G are visible, and in good agreement with the literature values of 2.3 and 3.3 G (Bowman, Mailer et al. 2004). The full width at half-height of the partially degassed trityl-OX63 signal is 0.22 G.

As an example of wider scans, a 40 G scan width was used to encompass both ^{15}N hyperfine lines of 6 mM ^{15}N-PDT in superabsorbent polymer (SAP). Although the macroscopic viscosity of the gel is high, the local microscopic viscosity is low. The X-band EPR signal was in the rapid tumbling regime. These experiments indicate that SAP can be used to prepare EPR samples in which small molecule solutes are tumbling freely, but the sample does not flow readily within the tube. The digital rapid scan spectrum (Fig. 5.7a) accurately reports the known nitrogen hyperfine splitting of 22.4 G.

To check the resolution of the spectra, a sample of 0.1 mM mHCTPO in 80:20 ethanol:water was obtained. The 0.47 G partially-resolved proton hyperfine splitting is well defined (Lin, Teicher et al. 1990), as shown in the Fig. 5.7b.

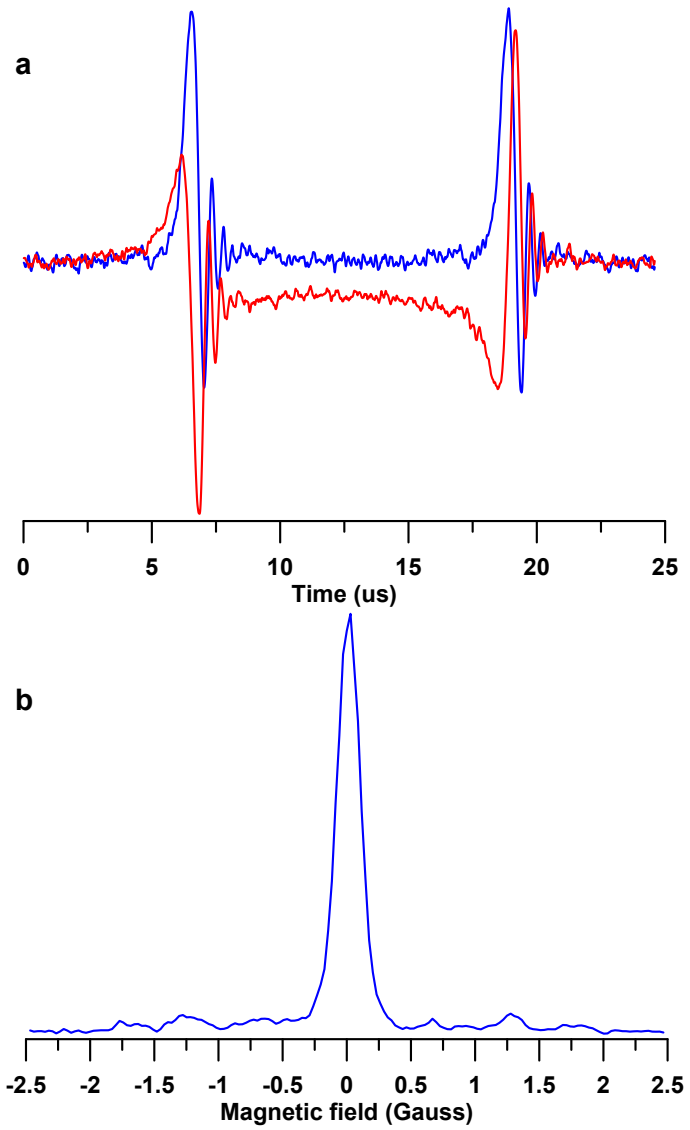

Fig. 5.6 X-band rapid-scan data for 0.2 mM OX63 in water with 0.6 mW power (B_1 ~ 7 mG) and 1024000 scans which required 200 s. (a) Reconstructed quadrature-detected rapid scan spectrum including both up and down scans---real (blue) and imaginary (red), including the rapid-scan oscillations. (b) Deconvolved spectrum. Spectra and data reproduced from the original journal article (Tseitlin, Yu et al. 2014).

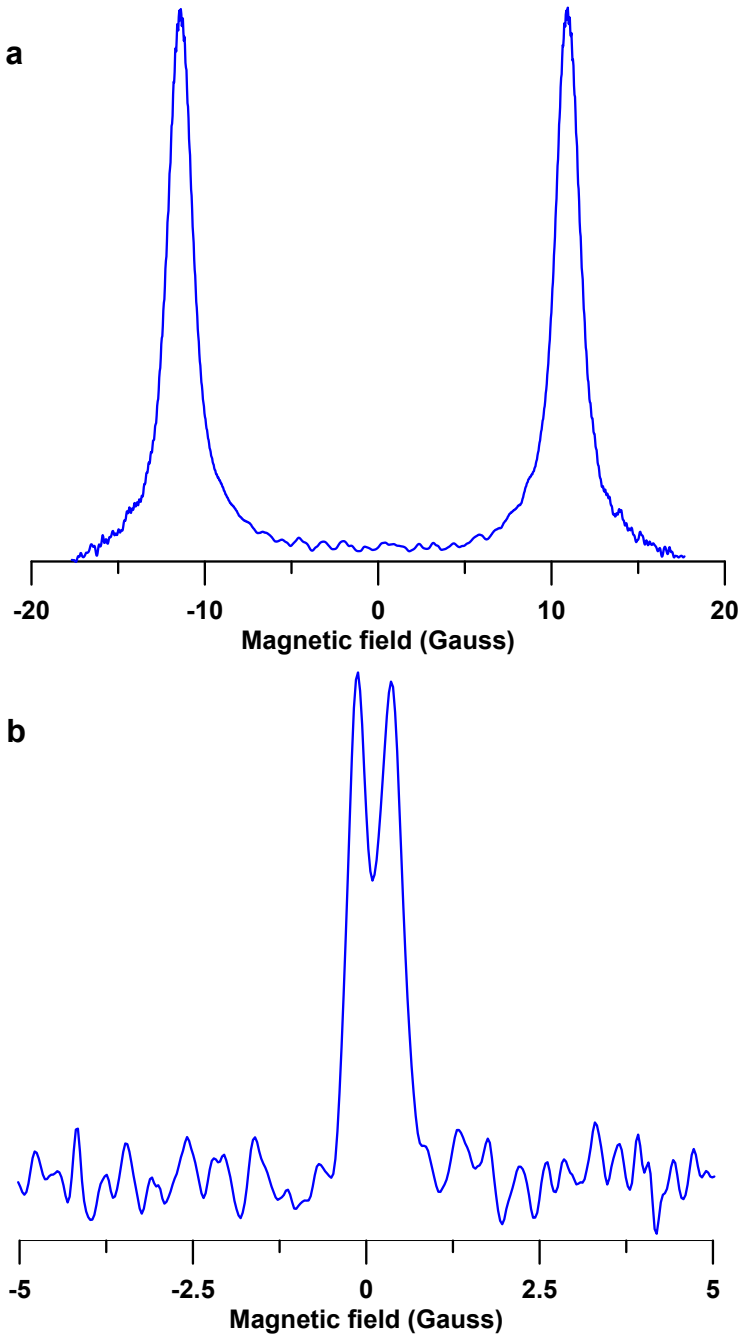

Fig. 5.7 X-band rapid scans. (a) Spectrum of 6 mM ^{15}N-PDT in superabsorbent polymer obtained with 0.6 mW power (B_1 ~ 15 mG) and 102400 scans, which required 20 s. (b) Spectrum of 0.1 mM mHCTPO in 80:20 ethanol:water obtained with 0.6 mW power (B_1 ~10 mG) and 2048000 scans, which required 400 s. Spectra and data reproduced from the original journal article (Tseitlin, Yu et al. 2014).

5.4. Discussion

There has been a continuing evolution of the use of digital technology in EPR since the early days of signal digitization. X-band pulsed EPR has recently been performed using microwaves generated with an AWG (Tseitlin, Quine et al. 2011, Kaufmann, Keller et al. 2013). One other lab, in parallel with our efforts, has digitally generated the incident RF and directly digitized the CW EPR signal at 300 MHz (Pursley, Salem et al. 2005, Pursley, Salem et al. 2006). The current work makes the major step to CW at X-band, which was not feasible until the latest developments in digital technology. Down-conversion and subsampling techniques, which are also extensively used in NMR (Hornung 2011) and MRI, have been used by the Hyde lab for recording multiharmonic X-band CW EPR (Hyde, Mchaourab et al. 1998, Froncisz, Camenisch et al. 2001, Hyde, Camenisch et al. 2005, Hyde, Strangeway et al. 2010)), by the Ohio State lab for L-band CW EPR (Ahmad, Som et al. 2010), and by the NCI lab to digitize an FID (Pursley, Salem et al. 2006). An AWG was used to control pulse timing in a 26.5-40 GHz pulsed EPR spectrometer (Astashkin, Enemark et al. 2006). These experiments have all used a traditional EPR spectrometer with substitution of the normal detection system by newer digital detection components. The programmability of an AWG permits direct synthesis of the excitation and reference frequencies, which removes the need for up- and down-conversion and thereby simplifies the spectrometer. Detection at an *IF* near baseband permits removal of the reflected signal at f_0. The experimental data demonstrate the performance of the algorithm using detection at $\omega_{IF} < \omega_s$ for rapid scan EPR and samples with linewidths as narrow as 0.22 G and scan widths up to 40 G.

The experiments are designed with exactly integer numbers of cycles for excitation, reference, and scan frequencies. This ensures that the signal is fully periodic with no discontinuities. In the example f_{scan} is denoted as 40 kHz. This number is not exact and scales with the actual resonator frequency. If the *IF* is changed substantially, a different high-pass filter would be needed and the resonating capacitor in the coil driver circuit would need to be changed. All other aspects of the digital system can be varied over a wide range of frequencies.

A major advantage of this method is the removal of the non-EPR component of the signal at ω_{IF}, prior to digitization. For a reflection resonator this is reflected source power and leakage through the circulator. For a cross-loop resonator it is leakage through the resonator. This component may be orders of magnitude larger than the EPR signal. If this unwanted component is not removed, it may require low sensitivity settings for the digitizer, which would limit the vertical resolution that is available for the EPR component. Detection at $\omega_{IF} < \omega_s$ and removal of the component at ω_{IF}, as demonstrated for rapid scan, is valid for any periodic signal.

These experiments were designed as a proof of principle for AWG excitation and detection at near baseband ω_{IF}. Thus a comparison of signal-to-noise with conventional detection was not attempted. Even so, it is valuable to consider sources of noise in the digital instrumentation. There are digital clutter signals, which were cleanly removed by subtraction of off-resonance signals. The time jitter of the AWG is stated by the vendor to be too small to measure, and the experimental results obtained are consistent with that assertion. The phase noise for the current model of the AWG is stated to be about -100

dBc at 100 kHz offset at 9-10 GHz, which is significantly poorer than conventional CW sources that have phase noise about -140 dBc at 100 kHz offset. The AWG manufacturer has suggested that the phase noise could be reduced by using a low phase noise external clock generator, which can be implemented in future work. In addition, phase noise in the detected signal could be substantially decreased by use of a bimodal resonator. Thus it seems reasonable to propose that system optimization will result in signal-to-noise performance with AWG and digital signal processing comparable to conventional spectrometer, but with greatly enhanced flexibility for experimental design based on software rather than hardware changes.

5.5 Summary

The use of multiple synchronized outputs from an AWG provides the opportunity to perform EPR experiments differently than by conventional EPR. A method is reported for reconstructing the quadrature EPR spectrum from periodic signals that are generated with sinusoidal magnetic field modulation such as CW, multiharmonic, or rapid scan experiments. The signal is down-converted to an *IF* that is less than the field scan or field modulation frequency and then digitized in a single channel. This method permits use of a high-pass analog filter before digitization to remove the strong non-EPR signal at the *IF*, that might otherwise overwhelm the digitizer. The *IF* is the difference between two synchronized X-band outputs from a Tektronix AWG 70002A, one of which is for excitation and the other is the reference for down-conversion. To permit signal averaging, timing was selected to give an exact integer number of full cycles for each frequency. In

the experiments reported here the IF was 5 kHz and the scan frequency was 40 kHz. To produce sinusoidal rapid scans with a scan frequency eight times *IF*, a third synchronized output generated a square wave that was converted to a sine wave. The timing of the data acquisition with a Bruker SpecJet II was synchronized by an external clock signal from the AWG. The baseband quadrature signal in the frequency domain was reconstructed. This approach has the advantages that (i) the non-EPR response at the carrier frequency is eliminated, (ii) both real and imaginary EPR signals are reconstructed from a single physical channel to produce an ideal quadrature signal, and (iii) signal bandwidth does not increase relative to baseband detection. Spectra were obtained by deconvolution of the reconstructed signals for solid BDPA in air, 0.2 mM trityl OX63 in water, ^{15}N perdeuterated tempone, and a nitroxide with a 0.5 G partially resolved proton hyperfine splitting.

CHAPTER 6

MULTIHARMONIC EPR FOR EXTENDED SAMPLES WITH BOTH NARROW AND BROAD LINES

6.1 Introduction

In conventional CW EPR the magnetic field is modulated, often at 100 kHz, and the first-derivative of the absorption spectrum is acquired by phase-sensitive detection at the modulation frequency at a series of magnetic fields. In conventional spectroscopy if the ratio of the modulation amplitude to the peak-to-peak linewidth is greater than about 0.25, the spectrum is broadened (Eaton, Eaton et al. 2010). Combining information from multiple harmonics of the field modulation frequency has been shown to give the first-derivative spectrum with minimal broadening up to modulation amplitudes that are several times the linewidths (Tseitlin and Tseitlin 2009). The amplitude at the fundamental and at higher harmonics can be obtained by digital phase-sensitive detection of the signal at the modulation frequency and at its integer multiples (Tseitlin, Eaton et al. 2011). As the modulation amplitude is increased, the intensities at the higher harmonics of the modulation frequency increase, which can be used to improve the *S/N* of the spectrum for modulation amplitudes up to about 1.2 times linewidths, provided that sufficient harmonics are included in the data analysis (Tseitlin, Eaton et al. 2011). Accurate reconstruction of the spectrum from the higher harmonics requires that the

modulated magnetic field is uniform over the sample. In previously published reports thesamples were very small because the magnetic field uniformity that could be obtained with commercial modulation coils was adequate for multiharmonic spectroscopy only over a small region of space and with limited modulation amplitudes (Tseitlin and Tseitlin 2009, Tseitlin, Eaton et al. 2011). The larger scan coils that have been developed for rapid scan EPR improve the magnetic field homogeneity over larger samples (Yu, Quine et al. 2014) relative to what can be achieved with conventional modulation coils. In addition, the rapid scan coil driver can generate larger modulation amplitudes (Quine, Mitchell et al. 2012) than conventional modulation coil drivers. In previously published reports (Tseitlin and Tseitlin 2009, Tseitlin, Eaton et al. 2011) the multiharmonic reconstruction method was applied to samples with single relatively narrow linewidths that could be over-modulated with modest modulation amplitudes. The samples selected for study in this chapter of the dissertation have more complicated lineshapes that include both narrow and broad lines and require larger modulation amplitudes to achieve overmodulation. These lineshapes are more representative of real-world samples than the previous examples. (i) One sample was composed of ultramarine blue (ΔB_{pp} = 17 G) and BDPA (ΔB_{pp} = 0.85 G). (ii) The second sample was a nitroxide immobilized in sucrose octaacetate for which the narrowest feature has $\Delta B_{pp} \sim 3$ G, but the spectrum extends over about 150 G. The sample heights were about 5 mm.

The work reported in this chapter was done in close collaboration with Mark Tseitlin. The author of the dissertation did all of the experiments and most of the data analysis. Results described are published in the reference (Yu, Tseitlin et al. 2015).

6.2. Experimental section

6.2.1 Sample preparation

Nitroxide ^{14}N-PDT was purchased from CDN isotopes (Quebec, Canada). Solid ^{14}N-PDT and sucrose octaacetate were mixed in a ratio that would result in a 2.50 mM solution. The solids were ground gently in a mortar and pestle to mix the two components. The solid mixture was placed in a 4 mm O.D. quartz EPR tube, evacuated overnight to remove oxygen, heated gently above the melting point of sucrose octaacetate, and cooled to form a glass. The tube was flame sealed. The concentration of PDT in the sample was determined by comparison of the double integrated intensity with that for a standard sample of 0.56 mM tempone in toluene. The number of spins in the sealed sample was $4x10^{16}$. The concentration is lower than in the initial mixture due to loss of the volatile nitroxide during the evacuation and melting steps.

Ultramarine blue (UMB) was purchased from Pfaltz and Bauer (Waterbury, CT). α,γ-Bisdiphenylene-β-phenylallyl free radical (BDPA) complex with benzene (1:1), was purchased from Sigma Aldrich (batch #00226KM). Solid UMB and BDPA were each mixed with solid KCl and gently ground to prepare uniform samples with relatively low radical concentrations. The diluted UMB and BDPA samples were placed in separate capillary tubes that were supported in a 4 mm O.D. quartz EPR tube. The numbers of BDPA and UMB spins in the sample were about $6.6 x10^{15}$ and $2.2 x10^{16}$, respectively.

6.2.2 EPR spectroscopy

Conventional and multiharmonic field-modulated X-band spectra were recorded on a Bruker E500T using a Bruker Flexline ER4118X-MD5 dielectric resonator, and the Xepr software. The resonator Q is ~ 9000 for these nonlossy samples and has an efficiency of 3.8 G/√W (Mitchell, Tseitlin et al. 2013). For conventional spectra the 100 kHz modulation amplitude was 20% of ΔB_{pp}, and the modulated field was generated with the coils that are built into the resonator. The CW signal was digitized with a Bruker signal processing unit (SPU).

The multiharmonic spectra were obtained using the transient mode of the E500T. In this mode there is a low-noise microwave amplifier prior to the mixer, which is not present in the CW signal path. For the multiharmonic spectra, the field modulation was generated with a resonated scan driver (Quine, Mitchell et al. 2012). The scan frequency of about 41 kHz was measured with a Phillips PM680 counter. The scan coils have 200 turns of Litz wire (255 strands of AWG44 wire). The coil constant is 37.7 G/Amp. The modulation ratio, the ratio of the modulation amplitude h_{m} to ΔB_{pp} for the narrowest line in the spectrum, was varied from 0.2 to 10 for the sample containing UMB and BDPA and from 0.2 to 5.0 for the immobilized nitroxide. The input to the digitizer was filtered with a 4th order low-pass Butterworth filter (Krohn-Hite 3955). The cut-off frequency was 5 MHz, to ensure that all harmonics of interest could be measured. The signal was over-sampled at a rate of 50 MS/s (20 ns timebase). The field-modulated EPR signal was collected in a 2D experiment with 10 magnetic field points per gauss. At each magnetic field position the EPR signal intensity was digitized in quadrature with a Bruker SpecJet

II for multiple cycles of the modulation frequency. Data were acquired in a 2-D experiment in the standard Xepr software. The data acquisition time was calculated as the product of number of cycles, the period of a scan, the number of scans, and the number of field positions. This calculation does not include the overhead in the software, which has not been optimized for these experiments. Data at each magnetic field were transferred to a PC.

6.2.3 Data Processing Approach

The data analysis for multiharmonic EPR is described in (Tseitlin, Iyudin et al. 2009, Tseitlin and Tseitlin 2009, Tseitlin, Eaton et al. 2011). This method does not require prior knowledge of the signal lineshape. At each field position the periodic response of the spin system to field modulation is recorded. For modulation ratios substantially less than 1 the signal is a sinusoid, the amplitude of which is proportional to the first derivative at this field point. For higher modulation ratios the signal is the sum of n sinusoids with frequencies at the modulation frequency and its harmonics. The frequency at $n = 1$ is the scan frequency, which is also designated as the fundamental. The frequency at $n = 2$ is the second harmonic. With digital phase-sensitive detection the amplitudes at each of these frequencies can be determined. By sweeping the field and doing phase-sensitive detection at each field position, one obtains a set of n EPR spectra, $s_n(B)$ where $n = 1$ to N_H and N_H is the number of harmonics. The spectrum $s_1(B)$ is the conventional CW spectrum, which has the accurate first-derivative lineshape only if the modulation amplitude is substantially less than the linewidth of the narrowest line. The

multiharmonic reconstruction provides the accurate first-derivative lineshape, even if the modulation amplitude is large relative to the linewidth. For the multiharmonic analysis, all of the $s_n(B)$ harmonics were Fourier transformed into the conjugate domain, u.

$$S_n(u) = \int_{-\infty}^{\infty} e^{-juB} s_n(B) dB \tag{6.1}$$

Reconstruction is done in the Fourier domain in which *F(u)* is the Fourier transform of the first-derivative EPR spectrum;

$$F(u) = \frac{\sum_{n=1}^{n=N_H} D_n^*(u) S_n(u)}{\sum_{n=1}^{n=N_H} D_n^*(u) D_n(u)} LPF(u) \tag{6.2}$$

where

$$D_n(u) = \left(\frac{h_m}{4n}\right) j^{(n-1)} \left[J_{n-1}\left(\frac{h_m u}{2}\right) + J_{n+1}\left(\frac{h_m u}{2}\right)\right], \quad n > 0 \tag{6.3}$$

J(x) in Eq. 6.3 is the Bessel function of the first kind, h_m is the peak-to-peak modulation amplitude, and *LPF(u)* is a low-pass filter. To provide an equation that is convenient for the calculations, Eq. 6.2 was derived by rearrangement of the equations in the previous report (Tseitlin, Eaton et al. 2011), with the assumption that noise is sufficiently similar for all harmonics that differential weightings are not required. The details of the rearrangement are given in the following paragraphs and Eq. 6.4-6.8.

The equations in (Tseitlin, Eaton et al. 2011) were presented for the general case in which the standard deviations of the noise are different for different harmonics. In our experimental data we do not observe differences in noise levels so the analysis of the data can be simplified by assuming that the standard deviation of the noise is the same for all

harmonics. We have also observed that for the B_1 and modulation amplitudes used in this study, the noise levels are independent of modulation amplitude. Eq. 6.4 describes the relationship between experimental multi-harmonic spectra S, unknown first-derivative spectrum F, and noise-related Error:

$$S = \sum_{n=1}^{N_H} \alpha_n S_n = F\, D + \text{Error} \quad \text{and } D = \sum_{n=1}^{N_H} \alpha_n D_n \tag{6.4}$$

where α_n are complex weighting factors and D_n are the functions described in Eq. 6.3. Here (and in subsequent equations) the argument u of the functions S, D, and α_n is omitted. Solution of Eq. 6.5 to find α_n that minimize the error term leads to

$$\alpha_n D_n = |\alpha_n D_n|, \tag{6.5}$$

If the standard deviation of the noise level is the same for all harmonics and the arbitrary multiplier C that is mentioned in Tseitlin, Eaton et al. 2011 is set to 1, the absolute value of α_n is given by Eq. 6.6:

$$\gamma_n = |\alpha_n| = |D_n|. \tag{6.6}$$

Eqs. 6.5 and 6.6 give Eq. 6.7

$$\alpha_n = D_n^* \tag{6.7}$$

The expression for F from Eq. 6.2 can be into rewritten as

$$F \approx \sum_{n=1}^{N_H} \alpha_n S_n / \sum_{n=1}^{N_H} \alpha_n D_n \tag{6.8}$$

Substitution of Eq. 6.7 into Eq. 6.8 gives Eq. 6.9, which is Eq. 6.2.

$$F \approx \sum_{n=1}^{N_H} D_n^* S_n / \sum_{n=1}^{N_H} D_n^* D_n \qquad (6.9)$$

The '≈' indicates the uncertainty caused by noise contributions from all harmonics. The criterion in Eq. 6.4 ensures that the uncertainty is minimized.

Inverse Fourier transformation of *F(u)* gives the reconstructed first-derivative spectrum. The *S/N* of the reconstructed spectrum is dependent on the parameters of the low-pass filter (Tseitlin, Eaton et al. 2011), which is applied prior to inverse Fourier transformation. The *LPF(u)* was a convolution of Gaussian function with a square profile with amplitude equal to one between plus and minus the cutoff frequency and zero otherwise. The role of the Gaussian is to smooth the transition in the vicinity of the cutoff and avoid discontinuities in the product function, Eq. 6.2. The width of the Gaussian as well as the cutoff frequency is optimized for a given spectrum, with tradeoffs between *S/N* and line broadening. Selection of filter parameters depends on the linewidths in the spectrum and not on the modulation amplitude.

6.2.4 Processing experimental data

A block diagram for the data processing procedure is shown in Fig. 6.1. At each magnetic field, the output from the quadrature mixer of the spectrometer is digitized by the SpecJet II, producing real arrays $I(t,B)$ and $Q(t,B)$. From the original 8192 data points in the time dimension at each magnetic field, segments corresponding to exactly 6 scan cycles were selected. From these segments of $I(t,B)$ and $Q(t,B)$, the amplitudes for each sinusoidal harmonic up to n = 100 were obtained by digital phase-sensitive detection

(Tseitlin, Eaton et al. 2011) and stored in complex arrays $p_n(B)$ and $p_n'(B)$, respectively. An automatic routine selects the modulation phase by maximizing the amplitude of the real components and minimizing the imaginary components for $n = 1$. For $n = 1$ the phase correction is ϕ and for higher harmonics it is n times ϕ. The phase-corrected results are stored in complex arrays $s_n(B)$ and $s_n'(B)$. If the phase correction is greater than about $\pm 90^o$, a 180^o correction is applied manually prior to iteration. Arrays $s_n(B)$ and $s_n'(B)$ are Fourier transformed as described in Eq. 6.1, producing $S_n(u)$ and $S_n'(u)$. Reconstruction of $F(u)$ and $F'(u)$ is performed as described by Eq. 6.2, which includes a low-pass filter. The low-pass filter removes high frequency noise, and was set to a value that depends on the bandwidth of the signal. Setting the value too high in the u domain leaves excess noise in the spectrum. If the cutoff is too low in the u domain, it improves *S/N* but rejects some high frequency components and may result in signal broadening. After inverse Fourier transformation of complex arrays *F(u)* and *F'(u)*, the imaginary parts are negligible because of the prior modulation phase correction. The real parts of the inverse Fourier transforms of *F(u)* and *F'(u)*, respectively, become the real and imaginary parts of *f(B)*. The microwave phase is then set by taking the appropriate combination of the two complex components of *f(B)*. The emphasis in the following discussion is on the absorption signal, although the dispersion is available for other applications.

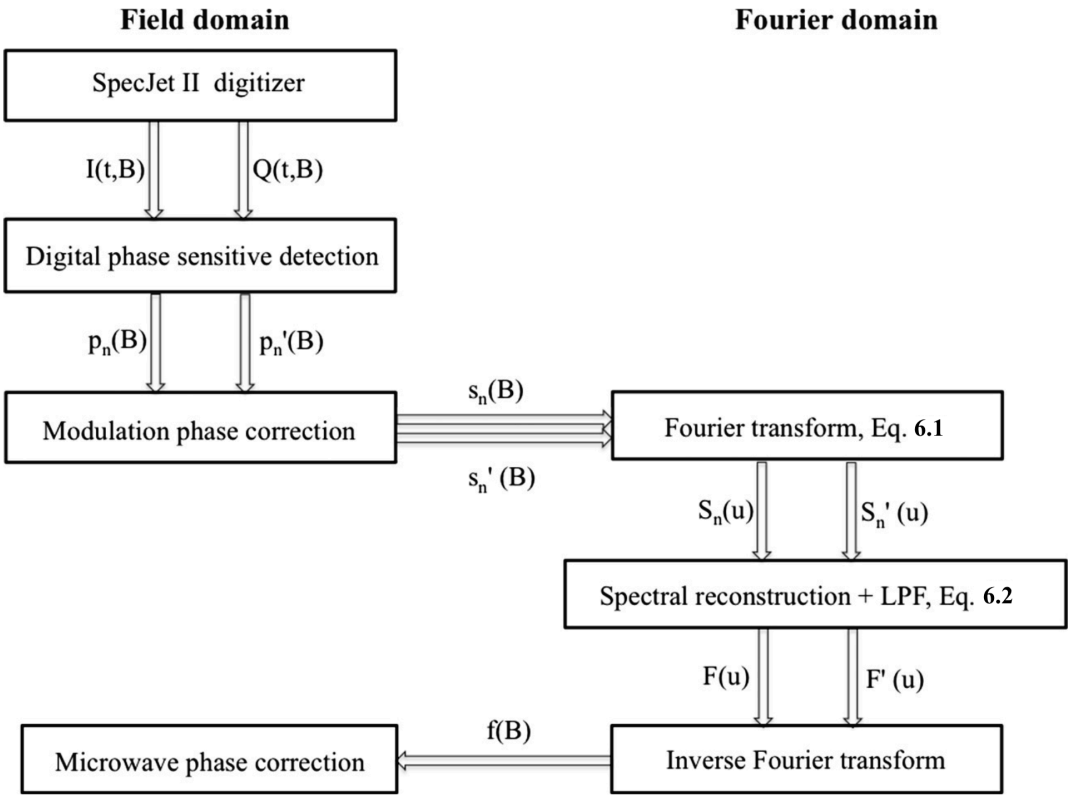

Fig. 6.1 Data processing procedure. For each magnetic field step in the spectrum, digital phase-sensitive detection is applied to both quadrature channels from the digitizer, which produces complex arrays $p_n(B)$ and $p_n'(B)$. The modulation phase is adjusted to null the imaginary component of each array. Fourier transformation of both arrays produces $S_n(u)$ and $S_n'(u)$. Reconstruction of the Fourier transform of the spectrum (Eq. 6.2) and low pass filtering produces $F(u)$ and $F'(u)$. Inverse Fourier transformation gives the complex spectrum $f(B)$. Microwave phase correction produces absorption and dispersion spectra. Diagram reproduced from the original journal article (Yu, Tseitlin et al. 2015).

6.3 Results

It could be argued that the appropriate way to evaluate the performance of the multiharmonic reconstruction algorithm would be comparison of conventional CW and multiharmonic spectra obtained from the same spectrometer. However, that comparison is complicated by differences in signal path and data processing between the conventional CW path of the E500T and the transient path that was used for the multiharmonic reconstruction. In the conventional CW signal path the EPR signal is digitized with a Bruker SPU. The user has the option of applying a post-processing smoothing filter. The low-pass filter in the Fourier domain that was used for the multiharmonic reconstruction may impact noise differently than the smoothing option of the SPU. In the transient path there is a low-noise amplifier that is not present in the conventional CW path. At the low microwave B_1s that were used to acquire the data for the multiharmonic reconstruction, the low noise amplifier can significantly improve the *S/N*. The impact of these factors on signals recorded at low modulation amplitudes is addressed by the comparisons in Fig. 6.2 for the UMB and BDPA sample.

Spectra for the sample of UMB and BDPA obtained with the same data acquisition time, B_1, and modulation amplitude, but with different data acquisition pathways and signal processing are shown in Fig. 6.2. The data were acquired with 0.17 G modulation amplitude (a modulation ratio of 0.2), which was selected to be conservative and not broaden the signal obtained using only phase-sensitive detection at the modulation frequency as is done in conventional CW spectroscopy. The spectrum acquired through the conventional signal path and processed with a 3-point smooth is

shown in Fig.6.2A. A 5-point smoothing gives *S/N* = 28. Since there were only 10 points in the field domain across the BDPA signal, the use of more than 5 points for the smoothing, which corresponds to about half of ΔB_{pp}, improves the *S/N*, but broadens the BDPA signal. The multiharmonic reconstruction uses a Fourier domain filter with different adjustable parameters than the smoothing function in the Xepr software. Fourier transformation and application of the same low-pass filter in the Fourier domain as was used for the multiharmonic data processing for the UMB and BDPA sample, produces the spectrum shown in Fig. 6.2B. This post-acquisition data processing had little impact on *S/N*, which demonstrates that the choice of the filter function is not a major contributor to the *S/N* difference between conventional CW and multiharmonic spectra on the E500T. The $s_1(B)$ spectrum from the multiharmonic data set (Fig. 6.2C) is the conventional first-derivative spectrum and accurately reflects the first-derivative spectral lineshape. The improvement in *S/N* by about a factor of 2.5 between either Fig. 6.2A or 6.2B and 6.2C reflects the differences in the signal detection pathways, which is attributed primarily to the low noise amplifier. A key issue related to multiharmonic reconstruction is whether inclusion of higher harmonics degrades the *S/N* if there is little intensity at the higher harmonics. At the low modulation amplitude of 0.17 G the lineshape in the spectrum $f(B)$ obtained by multiharmonic reconstruction with $N_H = 100$ (Fig. 6.2D) is essentially the same as in the $s_1(B)$ spectrum (Fig. 6.2C), because there is little or no intensity in the higher harmonics at this low modulation ratio. The *S/N* is about the same for Fig. 6.2C and Fig. 6.2D which shows that including higher harmonics does not degrade the *S/N* of the spectrum, and means that large numbers of

harmonics can routinely be included in the reconstruction independent of whether these harmonics have significant signal intensity.

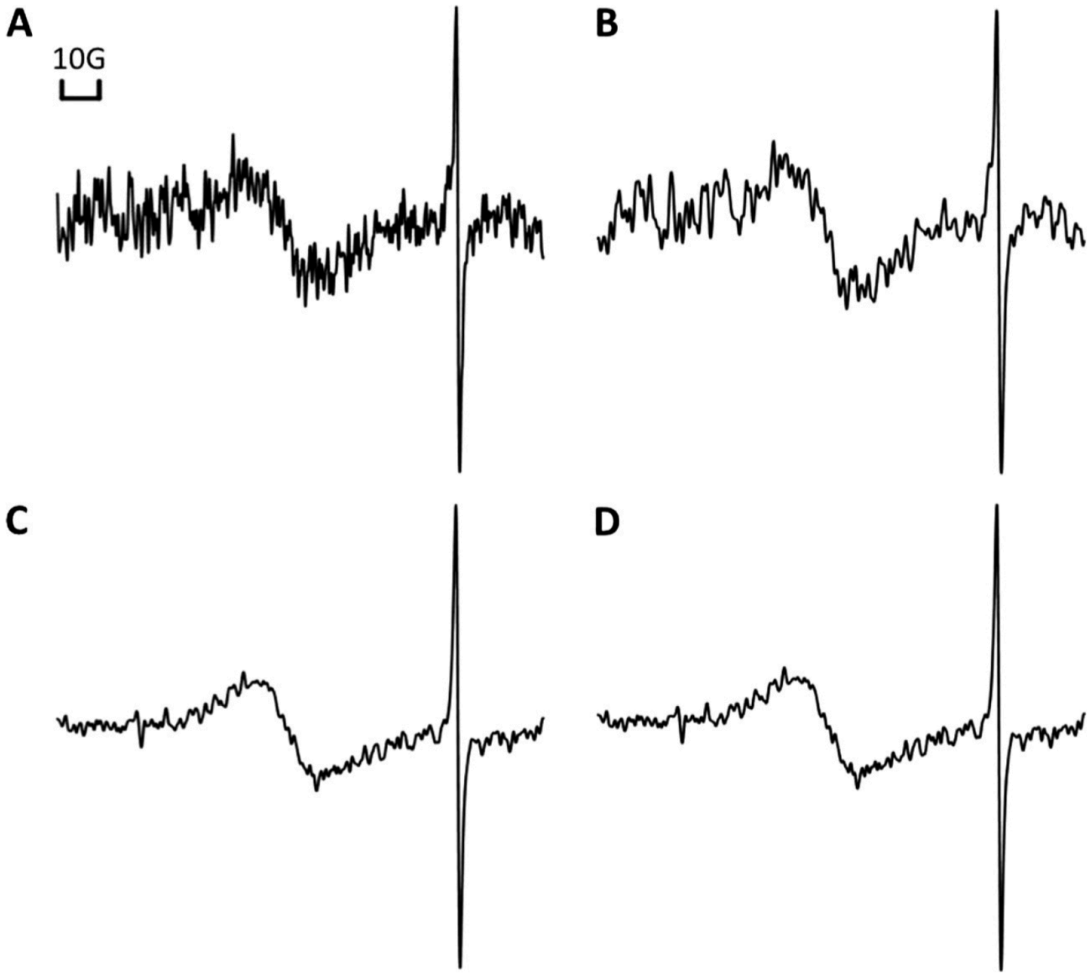

Fig. 6.2 130 gauss scans of the X-band spectra of the sample containing UMB and BDPA acquired with modulation amplitude of 0.17 G, B_1 of 2.5 mG, and the same 130 s data acquisition time. A) Signal acquired through the SPU, followed by 3-point smoothing, S/N = 27, B) Signal in A after Fourier filtering with the same cutoff as used for multiharmonic reconstruction, S/N = 30, C) $s_1(B)$ from the multiharmonic data set, S/N = 80, and D) f(B) obtained by multiharmonic reconstruction with N_H = 100, S/N = 80. Spectra and data reproduced from the original journal article (Yu, Tseitlin et al. 2015).

To evaluate the performance of the multiharmonic reconstruction method, independent of signal detection pathway or selection of digital filter, spectra are shown in Fig. 6.3 and 6.4 for n = 1 and multiharmonic reconstruction from the same data sets, using the same filter parameters. The data processing for n = 1 and for multiharmonic reconstruction are the same (Fig. 6.1) except that the multiplication by the Bessel functions in Eq. 6.2 is omitted for n = 1. The amplitudes of the multiharmonic spectra calculated using Eq. 6.2 are normalized by dividing by modulation amplitude. For comparison, the amplitudes of the n = 1 data in Fig. 6.3 and 6.4 also are normalized by dividing by modulation amplitude.

As shown in Eq. 6.2, a low pass filter $LPF(u)$ is applied to the Fourier transform of the spectrum in the u-domain, which can be represented as

$$F(u) = F'(u)LPF(u) \tag{6.10}$$

where $F'(u)$ is $F(u)$, prior to application of the filter. The conservative filter parameters were selected to preserve high frequency components of the signal that are important for accurate lineshapes, while cutting off the high frequency noise. Plots of the filter function overlaid on Fourier transforms of the reconstructed spectra for BDPA + UMB and for immobilized nitroxide are shown in Fig. 6.5 and 6.6.

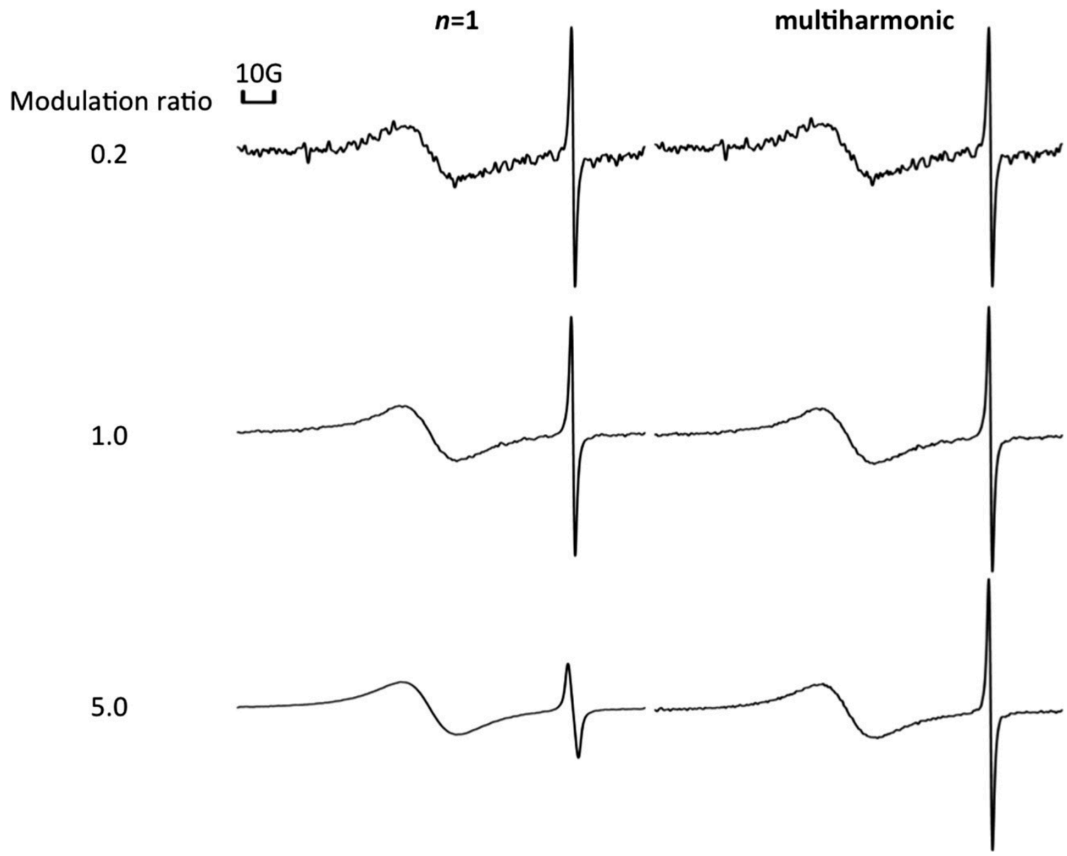

Fig. 6.3 Comparison of 130 gauss scans of the X-band spectra of the sample containing BDPA and UMB obtained with B_1 = 2.5 mG and 130 s data acquisition times, reconstructed with n = 1 and multiharmonic analysis for modulation ratios of 0.2, 1.0, and 5.0, respectively. Spectral amplitudes were normalized for modulation amplitude and y-axis scales are the same for all portions of the figure. Spectra and data reproduced from the original journal article (Yu, Tseitlin et al. 2015).

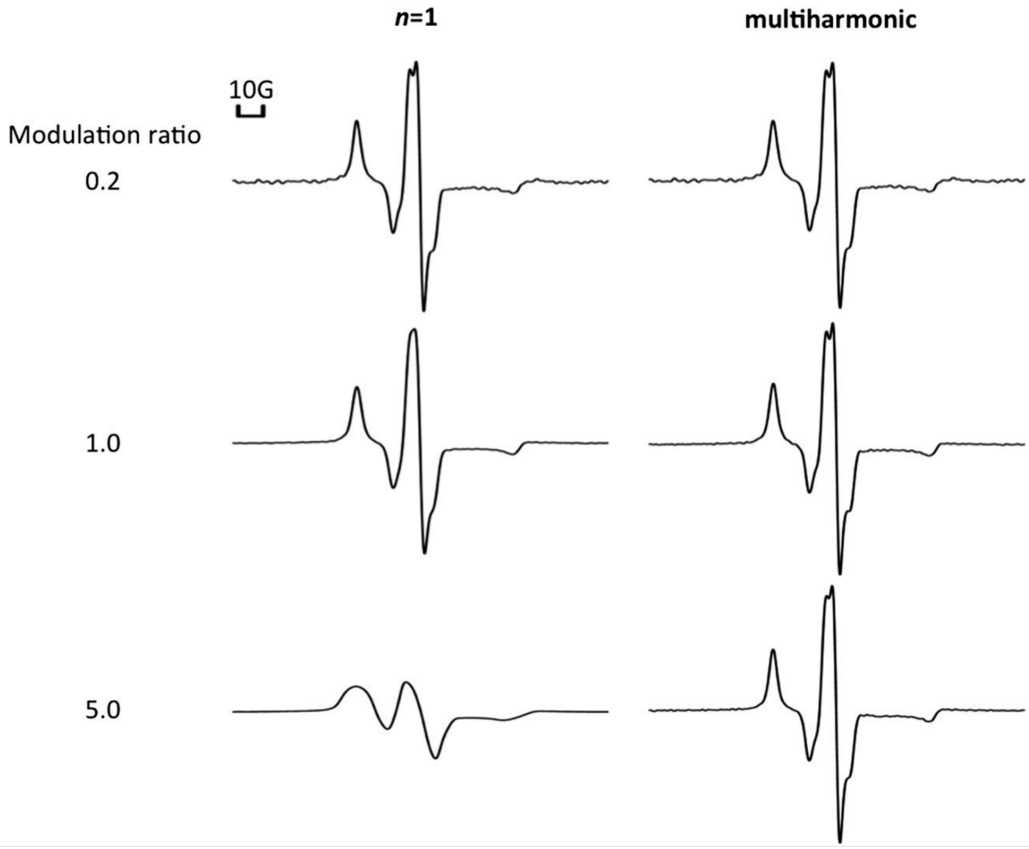

Fig. 6.4 Comparison of 150 gauss scans of X-band spectra of ^{14}N-PDT in sucrose octaacetate obtained with B_1 = 2.5 mG and 90 s data acquisition time, reconstructed with n = 1 and multiharmonic analysis for modulation ratios of 0.2, 1.0, and 5.0, respectively. Spectral amplitudes were normalized for modulation amplitude and y-axis scales are the same for all portions of the figure. Spectra and data reproduced from the original journal article (Yu, Tseitlin et al. 2015).

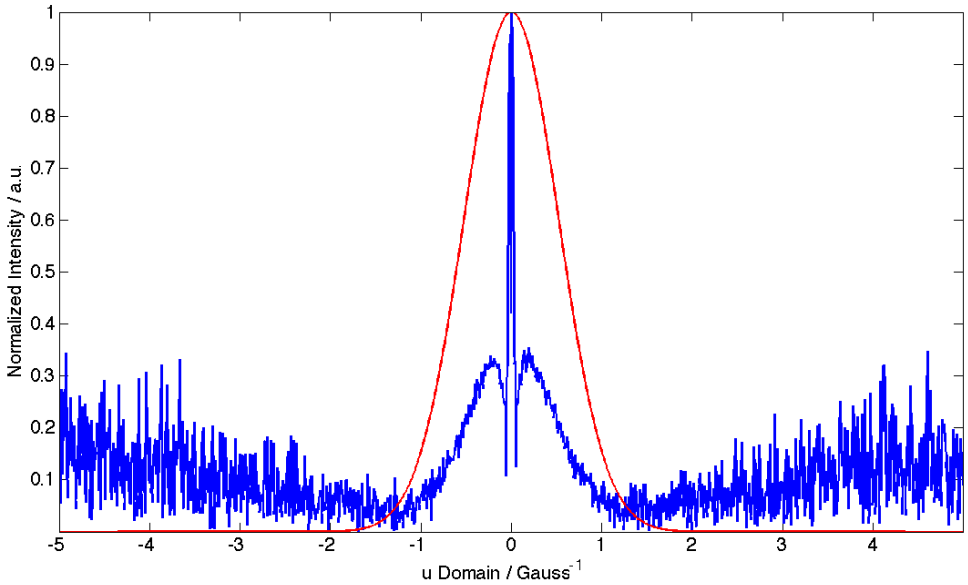

Fig. 6.5 The blue trace is $F'(u)$ for UMB and BDPA obtained with a modulation ratio of 1. The red trace is $LPF(u)$. Spectra and data reproduced from the original journal article (Yu, Tseitlin et al. 2015).

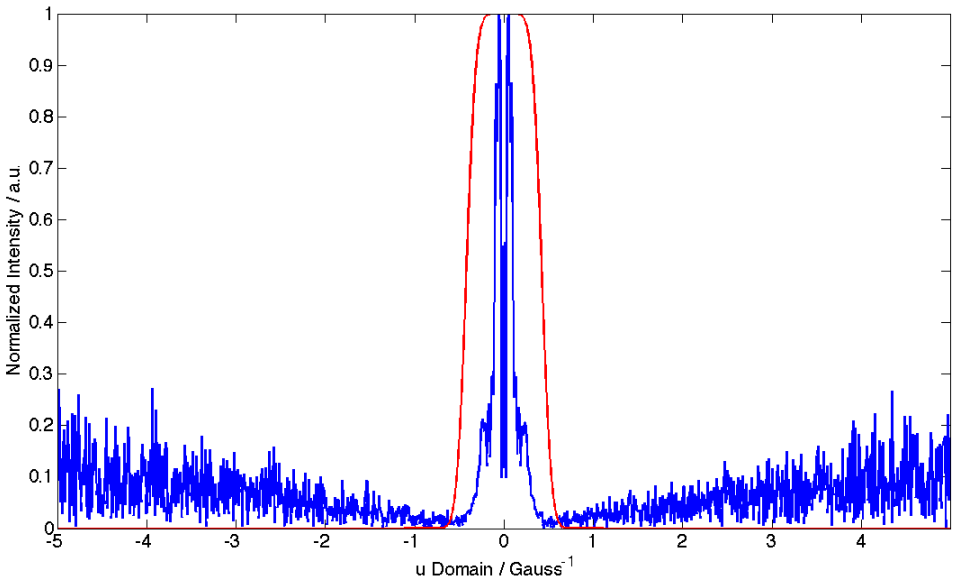

Fig. 6.6 The blue trace is $F'(u)$ for immobilized nitroxide obtained with a modulation ratio of 1. The red trace is $LPF(u)$. Spectra and data reproduced from the original journal article (Yu, Tseitlin et al. 2015).

Spectra of the sample of UMB and BPDA as a function of modulation ratio are shown in Fig. 6.3 for n = 1 and multiharmonic reconstruction. The modulation ratios listed in the figures and in Table 6.1 are relative to the BDPA linewidth. Since the linewidth for the UMB peak is about 20 times larger than for BDPA, the modulation ratios relative to the UMB peak are all less than 1. The data for modulation ratio = 0.2 are the same as shown in Fig. 6.2. All spectra were obtained with 10 magnetic field points per gauss, which limits the accuracy to which the linewidth of the BDPA signal can be measured to about ±0.1 G. Linewidths and *S/N* for the BDPA peak are summarized in Table 6.1. For spectra obtained with only n = 1 the linewidth of the BDPA signal broadens as the modulation ratio is increased above 0.2, as expected for conventional CW spectroscopy. The *S/N* for the BDPA peak in the multiharmonic spectrum improves from modulation ratio 0.2 to 1.0, but plateaus at a modulation ratio about 1, as reported previously (Tseitlin, Eaton et al. 2011). At higher modulation ratios the broadening of the BDPA signal is very modest compared with the broadening observed for only n = 1. Analysis of spectral parameters can be more strongly dependent on accurate lineshapes than on *S/N* (Tseitlin, Eaton et al. 2012), so the accurate lineshapes obtained from multiharmonic reconstruction can improve parameter precision in simulations. For spectra obtained with n = 1 the *S/N* for the UMB peak continues to increase at modulation ratios that are so high that the BDPA peak is severely broadened. The sample of UMB and BDPA was selected for this analysis because the lineshape changes for the two signals could be readily distinguished. For a sample with well resolved broad and sharp lines the *S/N* for the separate features could be optimized by

recording conventional CW spectra at high and low modulation amplitudes. For the more general case, as demonstrated in Fig. 6.4, broad and sharp features are superimposed. A major advantage of the multiharmonic method is that data can be acquired at relatively high modulation amplitude and decisions made in post-processing that optimize parameters for differing portions of the spectrum.

Table 6.1 Comparison of linewidths and *S/N* for n = 1 and multiharmonic reconstruction of spectrum for BDPA and UMB. Table and data reproduced from the original journal article (Yu, Tseitlin et al. 2015).

BDPA and UMB	fundamental, n=1			multiharmonic reconstruction		
modulation ratio[a]	ΔB_{pp} of BDPA [b]	*S/N* of BDPA[c]	*S/N* of UMB[c]	ΔB_{pp} of BDPA [b]	*S/N* of BDPA[c]	*S/N* of UMB[c]
0.2	0.9	80	20	0.9	80	20
1.0	1.1	3.6×10^2	85	0.9	3.2×10^2	65
2.0	1.3	5.6×10^2	1.6×10^2	0.9	3.8×10^2	75
5.0	3.3	7.1×10^2	3.9×10^2	0.9	3.7×10^2	75
10	7.3	6.3×10^2	7.9×10^2	1.1	3.3×10^2	75

[a] Modulation ratio is based on the linewidth of the BDPA signal
[b] The peak-to-peak linewidth is in Gauss. The uncertainty for the BDPA linewidth is ±0.1 G due to data acquisition with 10 points/gauss.
[c] Uncertainty in *S/N* is about 10%.

As the modulation ratio is increased, the number of harmonics with signal intensity greater than noise increases (Table 6.2). The number of harmonics included in the multiharmonic reconstruction was varied and the linewidth of the BDPA peak was monitored. Including higher harmonics improves the accuracy of the lineshape.

Provided that the cutoff frequency in the low pass filter was selected appropriately, inclusion of additional harmonics does not degrade the *S/N*. Therefore comparisons were based on reconstructions with an arbitrarily large value of $N_H = 100$.

Spectra for the immobilized nitroxide sample as a function of modulation ratio are shown in Fig. 6.4 for $n = 1$ and multiharmonic reconstruction. The spectrum contains overlapping broad and narrow features, which is more realistic for real-world samples. The linewidths shown in Table 6.3 are apparent values measured from the spectra, which are useful monitors of spectral broadening. At low modulation ratio the lineshape for the multiharmonic spectrum matches well with that obtained with $n = 1$. For $n = 1$ the narrowest lines broaden as expected as the modulation ratio is increased to 1.0 or 5.0 (Table 6.3). For the multiharmonic reconstruction the lineshape is preserved as the modulation ratio is increased from 0.2 to 1.0 and the narrowest feature is broadened by only about 10% as the modulation ratio is increased further to 5. The *S/N* improves from modulation ratio 0.2 to 1.0 but then declines slightly at 5.0 due to broadening of the spectrum. Higher modulation ratios increase the scan rate through the spectrum, which could result in rapid scan conditions for ratios larger than 5 (Eaton, Quine et al. 2014). Since the reconstruction algorithm does not apply in the rapid scan regime, modulation ratios higher than 5 were not used for the nitroxide sample.

Table 6.2 Number of harmonics with signal amplitude greater than noise for spectra of BDPA and UMB with various modulation ratios. Table and data reproduced from the original journal article (Yu, Tseitlin et al. 2015).

modulation ratio[a]	number of harmonics[b]
0.2	3
1.0	6
2.0	12
5.0	25
10	45

[a] Modulation ratio is based on the linewidth of the BDPA signal.
[b] The number includes the fundamental of the sweep frequency.

Table 6.3 Comparison of *S/N* for n = 1 and multiharmonic reconstruction for immobilized nitroxide spectrum. Table and data reproduced from the original journal article (Yu, Tseitlin et al. 2015).

^{14}N-PDT in sucrose octaacetate	fundamental n = 1		multiharmonic reconstruction	
modulation ratio[a]	*S/N* [b]	ΔB_{pp} [d]	*S/N* [b]	ΔB_{pp} [d]
0.2	3.1×10^2	3.1	3.1×10^2	3.1
1.0	~1.5×10^3 [c]	4.0	9.6×10^2	3.1
5.0	~2.5×10^3 [c]	12.5	8.6×10^2	3.2

[a] Modulation ratio is based on the linewidth of the narrowest line
[b] *S/N* is based on the narrowest line.
[c] *S/N* is too large to measure accurately.
[d] Apparent peak-to-peak linewidth (G) for central feature.

6.4. Discussion

The multiharmonic reconstruction method permits use of substantially higher modulation ratios than conventional CW spectroscopy without substantial line broadening, which improves *S/N* (Tseitlin and Tseitlin 2009, Tseitlin, Eaton et al. 2011). Uncertainty analysis has shown that *S/N* is not the only criterion for the quality of spectra (Tseitlin, Eaton et al. 2012). The accurate lineshapes obtained by multiharmonic reconstruction are important for extraction of parameters by simulations. The multiharmonic method was applied to samples with lineshapes that include both narrow and broad lines, thereby demonstrating the generality of the method. The ability to use modulation amplitudes larger than linewidths without substantially broadening the lines is especially useful for these composite lineshapes. This methodology also means that the selection of the modulation amplitude that can be used without spectral distortion is no longer tightly tied to the linewidth of the narrowest line. Multiharmonic reconstruction may be especially important in obtaining accurate projections for EPR imaging because overmodulation can be used to improve the *S/N* without losing resolution in the projection and the resulting image. The coil driver and Litz wire coils developed for rapid scan EPR (Quine, Mitchell et al. 2012, Yu, Quine et al. 2014) produce wider scans with a uniform field over a longer sample than is possible with the standard commercial modulation fields. The modulation field uniformity permits the extension of the previously described multiharmonic method to samples with lengths of about 5 mm, which is close to optimal for the B_1 distribution in the Bruker dielectric resonator that was used for the experiments.

When data are acquired digitally the user has options for how to process the information. The user can select multiharmonic reconstruction, which maintains the most accurate lineshape. Alternatively, since the $n = 1$ spectrum from the multiharmonic data set is equivalent to the conventional field modulated signal, the user can decide to work with the $n = 1$ spectrum if that has higher *S/N* for broad features in the spectrum. For either approach the filter parameters are selected in post-processing and can be adjusted as desired, instead of requiring reacquisition of data as in conventional CW spectrometers. As digital systems become increasingly common, multiharmonic EPR is likely to become more generally available as a tool to improve *S/N* and to simplify the selection of the modulation amplitude parameter.

6.5 Summary

Multiharmonic electron paramagnetic resonance spectroscopy was demonstrated for two samples with both narrow and broad lines: (i) BDPA with ΔB_{pp} of 0.85 G plus ultramarine blue with ΔB_{pp} of 17 G, and (ii) a nitroxide radical immobilized in sucrose octaacetate. Modulation amplitudes up to 17 G at 41 kHz were generated with a rapid scan coil driver and Litz wire coils that provide uniform magnetic field sweeps over samples with heights of 5 mm. Data were acquired with a 2-D experiment in the Xepr software through the transient signal path of a Bruker E500T and digitized in quadrature with a Bruker SpecJet II. Signals at the modulation frequency and its harmonics were calculated by digital phase-sensitive detection. The number of harmonics with signal intensity greater than noise increases as the ratio of the modulation amplitude to the

narrowest peak increases. Spectra reconstructed by the multiharmonic method from data obtained with modulation amplitudes up to five times the peak-to-peak linewidths of the narrowest features have linewidths that are broadened by up to only about 10% relative to linewidths in spectra obtained at low modulation amplitudes. The signal-to-noise improves with increasing modulation amplitude up to the point where the modulation amplitude is slightly larger than the linewidth of the narrowest features. If this high a modulation amplitude had been used in conventional methodology the linewidth of the narrowest features would have been severely broadened. The multiharmonic reconstruction methodology means that the selection of the modulation amplitude that can be used without spectral distortion is no longer tightly tied to the linewidth of the narrowest line.

CHAPTER 7

DEVELOPMENT OF DIGITAL SATURATION RECOVERY SPECTROMETER

7.1 Introduction

Saturation recovery is an EPR method to directly measure the spin lattice relaxation time, T_1 (Huisjen and Hyde 1974, Percival and Hyde 1975, Quine, Eaton et al. 1992, Eaton, Eaton et al. 2005). With a long microwave pump pulse, the transition between spin states is saturated and the population of spins in the ground and excited states are equalized. After the long microwave pulse, a weaker B_1 is used to detect the recovery of the EPR signal from saturation. The recovery curve is fitted with an exponential function to calculate T_1.

7.2 Hardware development

With help from Richard Quine and Tengzhi Liu, the digital saturation recovery spectrometer was constructed in June 2015 and preliminary tests were performed in July. The block diagram is shown in Fig. 7.1. The author and Richard Quine designed this spectrometer. The logic outputs from the AWG are only 1.4 V, which are not enough to drive SP3T pin diode switches, item (5) in Fig. 7.1. A TTL level convertor is needed to convert the logic outputs in the AWG from 1.4 V to 5 V. The TTL (Transistor–transistor logic) level convertor and video amplifier were designed and constructed by Richard

Quine. A Burker E500T spectrometer was used to control the magnetic field and the SpecJet II digitizer was used for data detection. A LeCroy 44Xi-A Waverunner oscilloscope was used for resonator frequency tuning.

The maximum output power form the AWG is 350 μW so a 2-Watts power amplifier was used to create sufficient power for the pump pulse. The output power is control with 8-bit DAC (digital-analog convertor). To get sufficient range of observation power, there are two detection pathways, which have different amplifications for microwaves.

The waveforms generated by the AWG for frequency tuning, signal excitation, signal observation, reference, and switch controls are shown in the program in appendix C. The marker signals from AWG Channel 1 are used to control the SP3T pin diode switches, item (5) in Fig. 7.1, for switching between the excitation microwave and observation microwave. The switches select between these paths. The path that includes the 2 Watts power amplifier, item (2) in Fig. 7.1, is used to provide the excitation microwave power. There are two options for the observe power. The path with the low noise amplifier (LNA) provides an option for higher observe power than in the third path.

Since the isolation of SP3T switch between excitation path and observation path is not good enough for this application, a pin diode switch, which is controlled by the same marker signal as for excitation path, was added to isolate the 2 Watts microwave power amplifier in the excitation path during the signal observation. The sequencer in the Tektronix AWG 70002A was used to sequentially and periodically generate excitation microwaves or observation microwaves for signal detection and averaging.

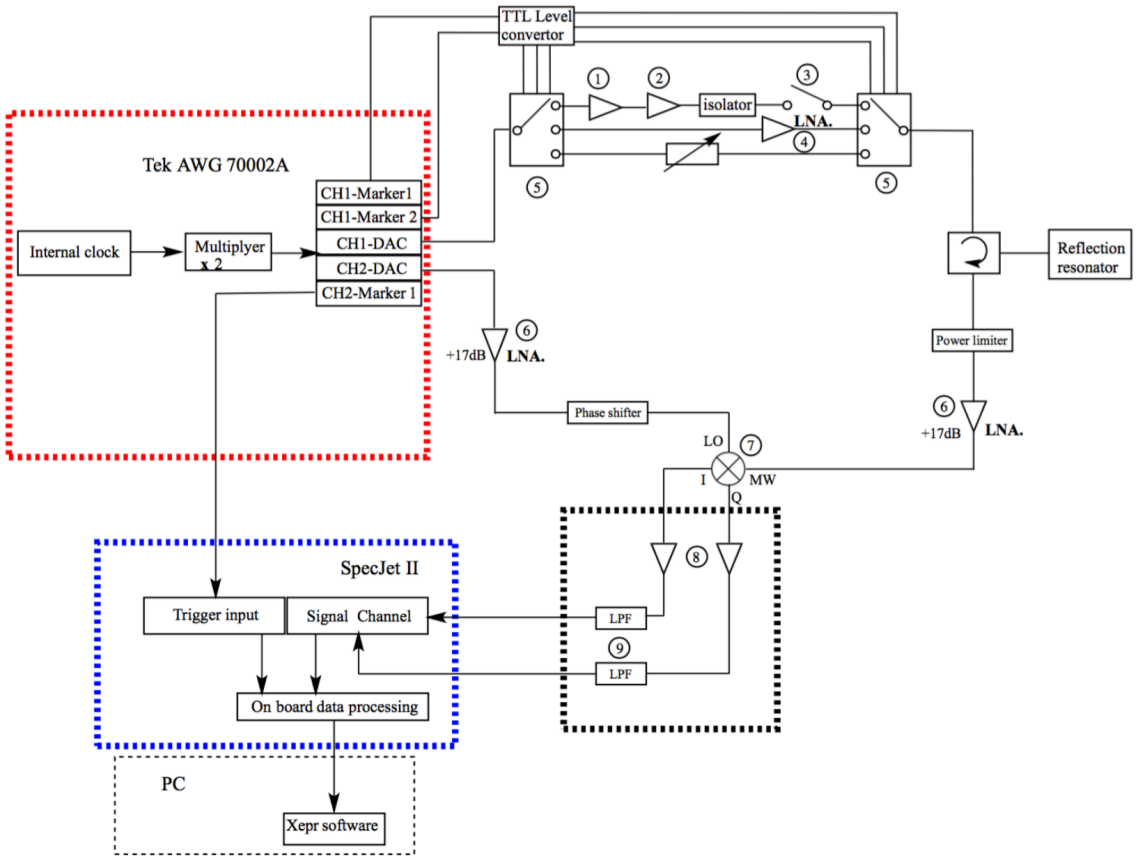

Fig. 7.1 The block diagram of digital saturation recovery system using sequencer function in Tektronix arbitrary waveform generator 70002A. The circled numbers in the diagram denote the following components. (1) microwave power amplifier: Mini circuits ZX60- 14012L-S+; (2) microwave power amplifier: PE15A4001, 2 watts power amplifier ; (3) pin diode switch: General Microwave DM864BH; (4) low noise amplifier: RLNA0812G25, noise figure = 1.6 dB; (5) SP3T PIN diode Switches: 3 ports pin diode switch, RFSP3TR0612G; (6) low noise amplifiers: HD27028, noise figure = 1.8 dB; (7) I/Q mixer: MLIQ-0218L; (8) home-built variable gain video amplifiers; (9) home-built low pass filters. (Unpublished work)

7.3 Preliminary results

The saturation recovery signal from a radiation-induced E' center in a fused quartz rod that was irradiated to 244 kGy by ^{60}Co gamma radiation in Cobe Labs (Eaton and Eaton 1993), is shown in Fig. 7.2.

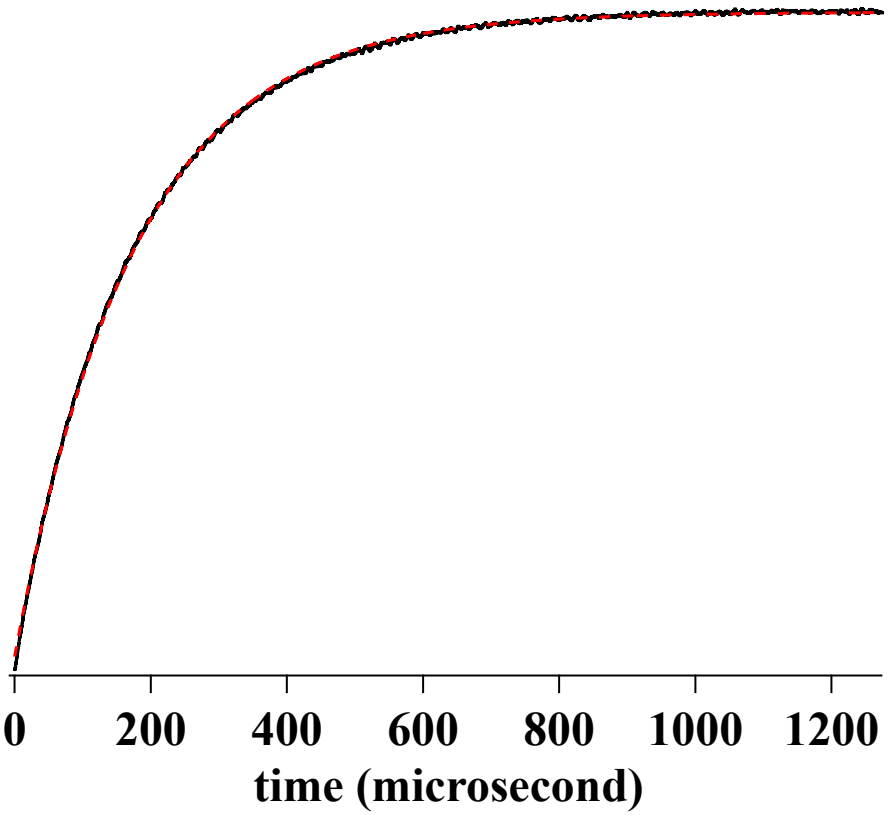

Fig. 7.2 The saturation recovery spectrum of an irradiated quartz rod (244 kGy). The black solid line is the saturation recovery spectrum after a 100 kHz low pass filter with 20480 averages. The red dashed line is the exponential fitting results from the Bruker Xepr software. The calculated T_1 of this spectrum is 176 us. (Unpublished work)

The magnetic field dependence of T_1 of the irradiated quartz rod is shown in Fig. 7.3. The result is in a good agreement with the published values (Eaton and Eaton 1993).

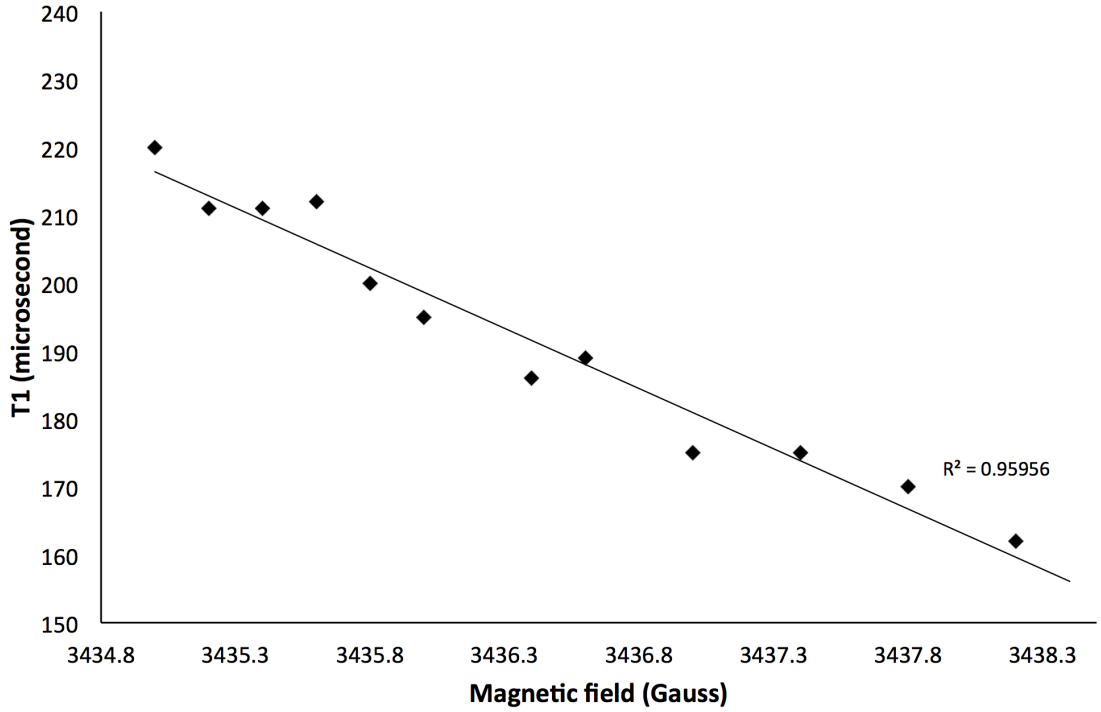

Fig. 7.3 The magnetic field dependence of T_1 of irradiated fused quartz at room temperature. (Unpublished work)

7.4 Summary

The digital saturation recovery spectrometer is still under the development and the performance of the spectrometer needs to be compared with the traditional analog saturation recovery spectrometer (Quine, Eaton et al. 1992). More samples with various T_1 need to be tested on the digital saturation recovery spectrometer.

CHAPTER 8

SUMMARY AND COMMENTS ON FUTURE WORK

8.1 Summary of this dissertation

Through this dissertation, the extended applications of rapid scan EPR and the development of digital EPR were demonstrated.

In Chapter 2 and 3, the application of rapid scan EPR in immobilized nitroxides, spin-labeled protein, irradiated tooth enamel and fingernails showed the capability of rapid scan for broad signals of significance in biomedical research. The *S/N* improvements from rapid scan will help to detect low concentrations of spins and to improve the performance of EPR for in vivo biomedical applications. In Chapter 4, field-stepped direct detection EPR showed a great potential to replace traditional CW EPR. With field-stepped direct detection, the advantage of rapid scan has been extended to much wider scans, which provides a better methodology for research on transition metal complexes in many systems including biological ones. The digital rapid scan EPR was demonstrated in Chapter 5. By taking the advantage of the advances of digital electronics, a digital EPR spectrometer with fully digital excitation and detection could become the driving force of an EPR revolution. In Chapter 6, multiharmonic methodology showed the advantages of data post-processing, which simplify the parameter selections of conventional EPR experiments.

8.2 Comments on future work

Since the rapid scan method has been applied to immobilized nitroxides and spin-labeled proteins at room temperature (Yu, Quine et al. 2014), a spectrometer, for measurement of low temperature rapid scan of the spin-labeled proteins in frozen solutions, may be attractive for protein research. At low temperature, the spin relaxation times are longer than at room temperature. One study (Mitchell, Tseitlin et al. 2013) showed that the rapid scan would be a better methodology than CW EPR when the relaxation times of the samples are relatively long.

The application of rapid scan EPR in tooth dosimetry showed a great improvement relative to CW EPR (Yu, Romanyukha et al. 2015). With the increased *S/N*, the in vivo tooth dosimetry application of rapid scan can achieve more precise estimation of dose level and use less time for data acquisition, which speeds up the diagnosis procedure.

The field-stepped direct detection has shown great potential to replace the traditional CW EPR. Some low spin concentration samples are needed to test the performance and the reliability of this method. Since the field-stepped direct detection method can be used for studying the transition metal complex (Yu, Liu et al. 2015), the study of metal centers in photo system in plants is a potential application of this method. Since the Bruker Xepr is not well designed for a 2D experiment with more than 1000 field steps, better software is needed for field-stepped direct detection to reduce the overhead during the data acquisition. The utilization of FPGA (field-programmable gate

array) in the digitizer, which works as a on-board data processing unit, may be the solution to make the field-stepped direct detection widely accepted.

With the advances of digital electronics, fully digital excitation and observation in EPR (Tseitlin, Yu et al. 2014), fewer components are needed in an EPR spectrometer and the cost of the spectrometer will be reduced. A multifunction and multifrequency EPR spectrometer can be constructed based on a digital EPR system.

BIBLIOGRAPHY

(2009). American National Standard for Dosimetry. Personnel dosimetry performance. Criteria for testing. ANSI. HPS. McLean, VA. **N13.11-2009;**.

Ahmad, R., S. Som, E. Kesselring, P. Kuppusamy, J. L. Zweier and L. C. Potter (2010). "Digital detection and processing of multiple quadrature harmonics for EPR spectroscopy." J. Magn. Reson. **207**: 322-331.

Alexander, G. A., H. M. Swartz, S. A. Amundson, W. F. Blakely, B. Buddemeier, B. Gallez, N. Dainiak, R. E. Goans, R. B. Hayes and P. C. Lowry (2007). "BiodosEPR-2006 Meeting: Acute dosimetry consensus committee recommendations on biodosimetry applications in events involving uses of radiation by terrorists and radiation accidents." Radiat. Meas. **42**: 972 - 996.

Ardenkjaer-Larsen, J. H., I. Laursen, I. Leunbach, G. Ehnholm, L.-G. Wistrand, J. S. Petersson and K. Golman (1998). "EPR and DNP properties of certain novel single electron contrast agents intended for oximetric imaging." J. Magn. Reson. **133**: 1-12.

Astashkin, A. V., J. H. Enemark and A. Raitsimring (2006). "26.5 - 40 GHz K_a-Band pulsed EPR spectrometer." Conc. Magn. Reson. B (Magn. Reson. Engin.) **29B**: 125 - 136.

Beeler, R., D. Roux, G. Bene and R. Extermann (1955). "Observation de battements en resonance magnetique electronique." Comptes Rendus Acad. Sci. France: 472 - 473.

Beeler, R., D. Roux, G. Bene and R. Extermann (1956). "Rapid-passage effects in electron spin resonance." Phys. Rev. **102**: 296.

Biller, J. R., M. Tseitlin, D. G. Mitchell, J. Yu, L. A. Buchanan, H. Elajaili, G. M. Rosen, J. P. Y. Kao, S. S. Eaton and G. R. Eaton (2015). "Improved Sensitivity for Imaging Spin Trapped Hydroxy Radical at 250 MHz." ChemPhysChem. **16**: 528 - 531.

Biller, J. R., M. Tseitlin, R. W. Quine, G. A. Rinard, H. A. Weismiller, H. Elajaili, G. M. Rosen, J. P. Kao, S. S. Eaton and G. R. Eaton (2014). "Imaging of Nitroxides at 250 MHz using Rapid-Scan Electron Paramagnetic Resonance." J. Magn. Reson. **242**: 162 – 168.

Blakney, G. T., C. L. Hendrickson and A. G. Marshall (2011). "Predator data station: a fast data acquisition system for advanced FT-ICR MS experiments." Int. J. Mass. Spectros. **306**: 246-252.

Bloembergen, N., E. M. Purcell and R. V. Pound (1948). "Relaxation Effects in Nuclear Resonance Absorption." Phys. Rev. **73**: 679-712.

Bowman, M. K., C. Mailer and H. J. Halpern (2004). "The solution conformation of triarylmethyl radicals." J. Magn. Reson. **172**: 254 - 267.

Brown, G. C., B. C. Dian, K. O. Douglass, S. M. Geyer and B. H. Pate (2006). "The rotational spectrum of epifluorohydrin measured by chirped-pulse Fourier transform microwave spectroscopy." J. Mol. Spect. **238**: 200-212.

Brown, G. G., B. C. Dian, K. O. Douglass and S. M. Geyer (2008). "A broadband Fourier transform microwave spectrometer based on chirp pulse excitation." Rev. Sci. Instrum. **79**: 053103-053101/053113.

Bugay, O., V. Bartchuk, S. Kolesnik and V. Maksimenko (1999). "EPR Spectroscopy of Radiation-Induced Centers in Tooth Enamel and its Application for Retrospective Dosimetry in Chernobyl Case." Appl. Magn. Reson. **16**: 317 - 323.

Cassata, J. R., M. Moscovitch, J. E. Rotunda and K. J. Velbeck (2002). "A new paradigm in personal dosimetry using LiF:Mg,Cu,P." Radiat. Protect. Dosimetry **101**: 27 - 42.

Charles, R. G., S. N. Holter and W. C. Fernelius (1960). "Manganese(II) Acetylacetonate." in Inorganic Synthesis. E. G. Rockow. Hoboken, N. J. , John Wiley & Sons, Inc. **6:** 164 - 166.

Dadok, J. and R. F. Sprecher (1974). "Correlation NMR spectroscopy." J. Magn. Reson. **13**: 243-248.

DeRose, V. J. and B. M. Hoffman (1995). "Protein structure and mechanism studied by electron nuclear double resonance spectroscopy." Meth. Enzymol. **246**: 554-589.

Du, J.-L., G. R. Eaton and S. S. Eaton (1995). "Temperature and orientation dependence of electron-spin relaxation rates for bis(diethyldithiocarbamato)copper(II)." J. Magn. Reson. A **117**: 67-72.

Du, J.-L., G. R. Eaton and S. S. Eaton (1996). "Electron spin relaxation in vanadyl, copper(II), and silver(II) porphyrins in glassy solvents and doped solids." J. Magn. Reson. A **119**: 240-246.

Du, J. L., K. M. More, S. S. Eaton and G. R. Eaton (1992). "Orientation dependence of electron spin phase memory relaxation times in copper(II) and vanadyl complexes in frozen solution." Israel J. Chem. **32**: 351-355.

Eaton, G. R., S. S. Eaton, D. P. Barr and R. T. Weber (2010). Quantitative EPR. New York, Springer-Verlag/Wein.

Eaton, S. S. and G. R. Eaton (1993). "Irradiated fused-quartz standard sample for time-domain EPR." J. Magn. Reson. **102**(3): 354-356.

Eaton, S. S., G. R. Eaton and L. J. Berliner, Eds. (2005). Biomedical EPR - Part B: Methodology, Instrumentation, and Dynamics. Biol. Magn. Reson. **24**, New York, Kluwer Academic/Plenum Press.

Eaton, S. S., R. W. Quine, M. Tseitlin, D. G. Mitchell, G. A. Rinard and G. R. Eaton (2014). Rapid Scan Electron Paramagnetic Resonance Multifrequency Electron Paramagnetic Resonance: Data and Techniques. S. K. Misra, Wiley, 3 - 67.

Fattibene, P. and F. Callens (2010). "EPR dosimetry with tooth enamel: A review." Appl. Radiat. Isotop. **68**: 2033 - 2116.

Freed, J. H. (1976). Theory of slow tumbling ESR spectra of nitroxides. Spin Labeling: Theory and Applications. L. J. Berliner. New York, Academic Press**:** 53-132.

Froncisz, W., T. G. Camenisch, J. J. Ratke and J. S. Hyde (2001). "Pulse saturation recovery, pulse ELDOR, and free induction decay electron paramagnetic resonance detection using time-locked subsampling." Rev. Sci. Instrum. **72**: 1837-1842.

Gaffney, B. J. and H. J. Silverstone (1993). "Simulation of the EMR spectra of high-spin iron in proteins." Biol. Magn. Reson. **13**: 1-57.

Grinberg, V. O., A. I. Smirnov, O. Y. Grinberg, S. A. Grinberg, J. A. O'Hara and H. M. Swartz (2005). "Practical conditions and limitations for high spatial resolution of multi-site EPR oximetry." Appl. Magn. Reson. **28**: 69-78.

Gupta, R. K., J. A. Ferretti and E. D. Becker (1974). "Rapid scan Fourier transform NMR spectroscopy." J. Magn. Reson. **13**: 275-290.

Hornung, P. A. (2011). Digital NMR Signal Processing Systems and Methods. U. P. Office. USA. **US 20110109310A1**.

Huisjen, J. and J. S. Hyde (1974). "A pulsed EPR spectrometer." Rev. Sci. Instrum. **45**: 669-675.

Hustedt, E. J. and A. H. Beth (2000). Structural information from CW-EPR spectra of dipolar coupled nitroxide spin labels. Biol. Magn. Reson. Ed., L. J. Berliner, G. R. Eaton and S. S. Eaton, Kluwer Academic. **19:** 155-184.

Hyde, J. S., B. Bennett, A. W. Kittell, J. M. Kowalski and J. W. Sidabras (2013). "Moving difference (MDIFF) non-adiabatic rapid sweep (NARS) EPR of copper(II)." J. Magn. Reson. **236**: 15 - 25.

Hyde, J. S., T. G. Camenisch, J. J. Ratke, R. A. Strangeway and W. Froncisz (2005). "Digital Detection by Time-Locked Sampling in EPR." Biol. Magn. Reson. **24**: 199-222.

Hyde, J. S., H. S. Mchaourab, T. G. Camenisch, J. J. Ratke, R. W. Cox and W. Froncisz (1998). "Electron paramagnetic resonance detection by time-locked subsampling." Rev. Sci. Instrum. **69**: 2622-2628.

Hyde, J. S., R. A. Strangeway, T. G. Camenisch, J. J. Ratke and W. Froncisz (2010). "W-Band Frequency-Swept EPR." J. Magn. Reson. **205**: 93 -101.

Ignatiev, E. A., A. Romanyukha, A. A. Koshta and A. Wieser (1996). "Selective saturation method for EPR dosimetry with tooth enamel." Appl. Radiat. Isotop. **47**: 333-337.

Joshi, J. P., J. R. Ballard, G. A. Rinard, R. W. Quine, S. S. Eaton and G. R. Eaton (2005). "Rapid-Scan EPR with Triangular Scans and Fourier Deconvolution to Recover the Slow-Scan Spectrum." J. Magn. Reson. **175**: 44-51.

Joshi, J. P., G. R. Eaton and S. S. Eaton (2005). "Impact of Resonator on Direct-Detected Rapid-Scan EPR at 9.8 GHz." Appl. Magn. Reson. **28**: 239-249.

Kaufmann, T., T. J. Keller, J. M. Franck, R. P. Barnes, S. J. Glaser, J. M. Martinis and S. Han (2013). "DAC-board based X-band EPR Spectrometer with Arbitrary Waveform Control." J. Magn. Reson. **235**: 95 - 108.

Kittell, A. W., T. G. Camenisch, J. J. Ratke, J. W. Sidabras and J. S. Hyde (2011). "Detection of undistorted continuous wave (CW) electron paramagnetic resonance (EPR) spectra with non-adiabatic rapid sweep (NARS) of the magnetic field." J. Magn. Reson. **211**: 228-233.

Kittell, A. W., E. J. Hustedt and J. S. Hyde (2012). "Inter-spin distance determination using L-band (1-2 GHz) non-adiabatic rapid sweep paramagnetic resonance (NARS EPR)." J. Magn. Reson. **221**: 51 - 56

Kittell, A. W. and J. S. Hyde (2015). "Spin-label CW microwave power saturation and rapid passage with triangular non-adiabatic rapid sweep (NARS) and adiabatic passage (ARP) EPR spectroscopy " J. Magn. Reson. **255**: 68 - 76.

Lin, Y. J., B. A. Teicher and H. J. Halpern (1990). "Synthesis of 4-protio-3-carbamoyl-2,2,5,5-tetraperdeuteromethyl-3-pyrrolin-1-yloxy (mHCTPO): a selectively isotopically labeled compound for use in T_2 spin label oxymetry." J. Labelled Compds Radiopharm. **28**(6): 621-631.

Meyer, V., M. A. Swanson, L. Clouston, P. J. Boratyński, R. Stein, H. Mchaourab, A. Rajca, S. S. Eaton and G. R. Eaton (2015). "Room-Temperature Distance Measurements of Immobilized Spin-Labeled Protein by DEER/PELDOR." Biophys. J. **108**: 1213-1219.

Mitchell, D. G., R. W. Quine, M. Tseitlin, S. S. Eaton and G. R. Eaton (2012). "X-band Rapid-Scan EPR of Nitroxyl Radicals." J. Magn. Reson. **214**: 221-226

Mitchell, D. G., R. W. Quine, M. Tseitlin, V. Meyer, S. S. Eaton and G. R. Eaton (2011). "Comparison of Continuous Wave, Spin Echo, and Rapid Scan EPR of Irradiated Fused Quartz." Radiat. Meas. **46**: 993-996.

Mitchell, D. G., R. W. Quine, M. Tseitlin, R. T. Weber, V. Meyer, A. Avery, S. S. Eaton and G. R. Eaton (2011). "Electron Spin Relaxation and Heterogeneity of the 1:1 α,γ-Bisdiphenylene-β-phenylallyl (BDPA) : Benzene Complex." J. Phys. Chem. B **115**: 7986-7990.

Mitchell, D. G., G. M. Rosen, M. Tseitlin, B. Symmes, S. S. Eaton and G. R. Eaton (2013). "Use of Rapid-Scan EPR to Improve Detection Sensitivity for Spin-Trapped Radicals." Biophys. J. **105**: 338 - 342.

Mitchell, D. G., M. Tseitlin, R. W. Quine, V. Meyer, M. E. Newton, A. Schnegg, B. George, S. S. Eaton and G. R. Eaton (2013). "X-Band Rapid-scan EPR of Samples with Long Electron Relaxation Times: A Comparison of Continuous Wave, Pulse, and Rapid-scan EPR." Mol. Phys. **111**: 2664 - 2673.

Neill, J. L., K. O. Douglass, B. H. Pate and D. W. Pratt (2011). "Next generation techniques in the high resolution spectroscopy of biologically relevant molecules." Phys. Chem. Chem. Phys. **13**: 7253-7262.

Owenius, R., G. R. Eaton and S. S. Eaton (2005). "Frequency (250 MHz to 9.2 GHz) and Viscosity Dependence of Electron Spin Relaxation of Triarylmethyl Radicals at Room Temperature." J. Magn. Reson. **172**: 168-175.

Percival, P. W. and J. S. Hyde (1975). "Pulsed EPR spectrometer II." Rev. Sci. Instrum. **46**: 1522-1529.

Pursley, R. H., G. Salem, N. Devasahayam, S. Subramanian, J. Koscielniak, M. C. Krishna and T. J. Pohida (2006). "Integration of digital signal processing technologies with pulsed electron paramagnetic resonance imaging." J. Magn. Res. **178**: 220-227.

Pursley, R. H., G. Salem, T. J. Pohida, N. Devasahayam, S. Subramanian and M. C. Krishna (2005). "Direct detection and time-locked subsampling applied to pulsed electron paramagnetic resonance imaging." Rev. Sci. Instrum. **76**: 53709-53715.

Quine, R. W. (2008). "Rapid Scan Control Parameters.", unpublished manual

Quine, R. W., T. Czechowski and G. R. Eaton (2009). "A Linear Magnetic Field Scan Driver." Conc. Magn. Reson. B (Magn. Reson. Engin.) **35B**: 44-58.

Quine, R. W., S. S. Eaton and G. R. Eaton (1992). "Saturation recovery electron paramagnetic resonance spectrometer." Rev. Sci. Instrum. **63**(10): 4251-4262.

Quine, R. W., D. G. Mitchell, S. S. Eaton and G. R. Eaton (2012). "A Resonated Coil Driver for Rapid Scan EPR." Conc. Magn. Reson., Magn. Reson. Engineer **41B**: 95 - 110.

Quine, R. W., G. A. Rinard, S. S. Eaton and G. R. Eaton (2010). "Quantitative Rapid Scan EPR Spectroscopy at 258 MHz." J. Magn. Reson. **205**: 23-27.

Rajca, A., V. Kathirvelu, S. K. Roy, M. Pink, S. Rajca, S. Sarkar, S. S. Eaton and G. R. Eaton (2010). "A spirocyclohexyl nitroxide amino acid spin label for pulsed EPR spectroscopy distance measurements." Chem. Eur. J. **16**: 5778 - 5782.

Reyes, R. A. (2008). Study of Electron Paramagnetic Resonance (EPR)/Electron Spin Resonance (ESR) Dosimetry in Fingernails as a Method for Assessing Dose of Victims of Radiological Accidents/Incidents. PhD, Uniformed Services University of the Health Sciences.

Rinard, G. A., R. A. Quine, J. R. Biller and G. R. Eaton (2010). "A Wire Crossed-Loop-Resonator for Rapid Scan EPR." Concepts Magn. Reson. B, Magn. Reson. Engineer **37B**: 86-91.

Romanyukha, A., D. L. King and L. K. Kennemur (2012). "Impact of Fukushima nuclear accident on background radiation doses measured by control dosimeters in Japan." Health Phys. **102**: 535 - 541.

Romanyukha, A. and F. Trompier (2011). Electron Paramagnetic Resonance Retrospective Dosimetry. Concepts and Trends in Medical Radiation Dosimetry, Proceedings of the 4th Summer School on Solid State Dosimetry, Wollongong, Australia. A. Rosenfeld, T. Kron, F. d'Errico and M. Moscovitch. Melville, NY, AIP Conference Proceedings. **1345:** 120 - 128.

Romanyukha, A., F. Trompier, R. Reyes, D. Christensen, C. Iddins and S. Sugarman (2014). "Electron paramagnetic resonance radiation dose assessment in fingernails of the victim exposed to high dose as result of an accident." Radiat. Environ. Biophys. **53**: 755–762.

Sato, H., B. A. Filas, S. S. Eaton, G. R. Eaton, A. A. Romanyukha, R. Hayes and A. M. Rossi (2007). "Electron Spin Relaxation of Radicals in Irradiated Tooth Enamel and Synthetic Hydroxyapatite." Radiation Measurements **42**: 997-1004.

Sato, H., V. Kathirvelu, A. J. Fielding, S. E. Bottle, J. P. Blinco, A. S. Micallef, S. S. Eaton and G. R. Eaton (2007). "Impact of molecular size on electron spin relaxation rates of nitroxyl radicals in glassy solvents between 100 and 300 K." Mol. Phys. **105**: 2137-2151.

Schweiger, A. and G. Jeschke (2001). Principles of Pulse Electron Paramagnetic Resonance. Oxford, Oxford University Press.

Simon, S. L., I. Bailiff, A. Bouville, P. Fattibene, R. A. Kleinerman, D. C. Lloyd, S. W. S. McKeever, A. Romanyukha, A. V. Sevan'kaev, J. D. Tucker and A. Wieser (2007). "BiodosEPR-2006 Consensus Committee Report on Biodosimetric Methods to Evaluate Radiation Doses at Long Times After Exposure." Radiat. Meas. **42**: 948 - 971.

Stoll, S. and A. Schweiger (2006). "EasySpin, a comprehensive software package for spectral simulation and analysis in EPR." J. Magn. Reson. **178**: 42-55.

Stoner, J. W., D. Szymanski, S. S. Eaton, R. W. Quine, G. A. Rinard and G. R. Eaton (2004). "Direct-detected rapid-scan EPR at 250 MHz." J. Magn. Res. **170**: 127-135.

Such, K. P. and G. Lehmann (1987). "E. P. R. of Mn2+ in acetylacetonates." Mol. Phys. **60**: 553 - 560

Swartz, H. M., G. Burke, M. Coey, E. Demidenko, R. Dong, O. Grinberg, J. Hilton, A. Iwasaki, P. Lesniewski, M. Kmiec, K.-M. Lo, R. J. Nicolalde, A. Ruuge, Y. Sakata, A. Sucheta, T. Walczak, B. B. Williams, C. A. Mitchell, A. Romanyukha and D. A. Schauer (2007). "In vivo EPR for dosimetry." Radiat. Meas. **42**: 1075 - 1084.

Trompier, F., A. Romanyukha, R. Reyes, H. Vezin, F. Queinnec and D. Gourier (2014). "State of the art in nail dosimetry: free radicals identification and reaction mechanisms." Radiat. Environ. Biophys. **53**: 291–303.

Tseitlin, M., T. Czechowski, R. W. Quine, S. S. Eaton and G. R. Eaton (2009). "Background Removal Procedure for Rapid Scan EPR." J. Magn. Reson. **196**: 48-53.

Tseitlin, M., G. R. Eaton and E. S. S. (2013). "Computationally Efficient Steady-State Solution of the Bloch Equations for Rapid Sinusoidal Scans Based on Fourier Expansion in Harmonics of the Scan Frequency." Appl. Magn. Reson. **44**: 1373 – 1397.

Tseitlin, M., S. S. Eaton and G. R. Eaton (2011). "Reconstruction of the first derivative EPR spectrum from multiple harmonics of the field-modulated CW signal " J. Magn. Reson. **209**: 277-281.

Tseitlin, M., S. S. Eaton and G. R. Eaton (2012). "Uncertainty analysis for absorption and first-derivative EPR spectra." Conc. Magn. Reson. **40A**: 295 - 305

Tseitlin, M., V. S. Iyudin and O. A. Tseitlin (2009). "Advantages of Digital Phase-Sensitive Detection for Upgrading an Obsolete CW EPR Spectrometer." Appl. Magn. Reson. **35**: 569-580.

Tseitlin, M., D. G. Mitchell, S. S. Eaton and G. R. Eaton (2012). "Corrections for sinusoidal background and non-orthogonality of signal channels in sinusoidal rapid magnetic field scans." J. Magn. Reson. **223**: 80 - 84.

Tseitlin, M., R. W. Quine, G. A. Rinard, S. S. Eaton and G. R. Eaton (2010). "Combining Absorption and Dispersion Signals to Improve Signal-to-noise for Rapid Scan EPR Imaging." J. Magn. Reson. **203**: 305-310.

Tseitlin, M., R. W. Quine, G. A. Rinard, S. S. Eaton and G. R. Eaton (2011). "Digital EPR with an arbitrary waveform generator and direct detection at the carrier frequency." J. Magn. Reson. **213**: 119-125.

Tseitlin, M., G. A. Rinard, R. W. Quine, S. S. Eaton and G. R. Eaton (2011). "Deconvolution of Sinusoidal Rapid EPR Scans." J. Magn. Reson **208**: 279-283.

Tseitlin, M., Z. Yu, R. W. Quine, G. A. Rinard, S. S. Eaton and G. R. Eaton (2014). "Digitally generated excitation and near-baseband quadrature detection of rapid scan EPR signals." J. Magn. Reson. **249**: 126 - 134.

Tseitlin, M. P. and O. A. Tseitlin (2009). "Using of digital demodulation of multiharmonic overmodulated EPR signals to improve EPR oximetry reliability" Appl. Magn. Reson. **36**: 25-34.

Turek, P., J. J. Andre, A. Giraudeau and J. Simon (1987). "Preparation and study of a lithium phthalocyanine radical: optical and magnetic properties." Chem. Phys. Lett. **134**: 471-476.

Weger, M. (1960). "Passage Effects in Paramagnetic Resonance Experiments." Bell System Technical J. **39**: 1013-1112.

Weil, J. A. and J. R. Bolton (2007). Electron Paramagnetic Resonance: Elementary Theory and Practical Applications. Hoboken, New Jersey, John Wiley

Yu, Z., T. Liu, H. Elajaili, G. A. Rinard, S. S. Eaton and G. R. Eaton (2015). "Field-Stepped Direct Detection Electron Paramagnetic Resonance." J. Magn. Reson., accepted for publication

Yu, Z., R. W. Quine, G. A. Rinard, M. Tseitlin, H. Elajaili, V. Kathirvelu, L. J. Clouston, P. J. Boratyński, A. Rajca, R. Stein, H. Mchaourab, S. S. Eaton and G. R. Eaton (2014). "Rapid-Scan EPR of Immobilized Nitroxides." J. Magn. Reson. **247** 67 - 71.

Yu, Z., A. Romanyukha, S. S. Eaton and G. R. Eaton (2015). "X-band Rapid Scan Electron Paramagnetic Resonance of Radiation Induced Defects in Tooth Enamel." Radiation Research, **184**, (2015), in press.

Yu, Z., M. Tseitlin, S. S. Eaton and G. R. Eaton (2015). "Multiharmonic Electron Paramagnetic Resonance for Extended Samples with both Narrow and Broad Lines." J. Magn. Reson. **254**: 86 - 92.

Zavoisky, E. (1944). "The paramagnetic absorption of a solution in parallel fields." J. Phys.- USSR **8**: 377-380.

Zavoisky, E. (1946). "Paramagnetic Absorption in Some Salts in Perpendicular Magnetic Fields." Zhurnal Eksperimentalnoi Teor. Fiz. **16**: 603-606.

APPENDICES

Appendix A: MATLAB Program for Field-stepped Direct Detection

1. An example of MATLAB program for the data analysis of field-stepped direct detection EPR

```
%% Mn in CaO sample stepwise RS spectral reconstruction
%  February-12-2015 by Zhelin Yu, revised: March-22-2015
%  Comments and questions to: Zhelin.Yu@du.edu
clear all;
clc;

%% Data loading
load('jy118140'); % load data collected from 2D experiment
in Xepr
B0=3127:3727;
[h_cw spc_cw]=eprload('jy118139');

%% Experimental parameters
sf=5.122676e3; % scan frequency / Hz
rs_width=0.666*17.32; % scan width / Gauss
sw=600; % Sweep width / Gauss
cf=3427; % Center field / Gauss
step_wise=1; % field resolution / Gauss
tb=(t(2)-t(1))/1e9; %  time base / second
field_res=0.1; % field resolution after filtering / Gauss
sH=100; % Gaussian filter parameter / mG

%% Signal channels balance and orthogonality correction
```

```
Acorr=0.93;
Ph_corr_Ortho=7;
Ph_exp_Ortho=exp(1i*Ph_corr_Ortho/180*pi);
rs_corr_Ortho=Acorr*real(rs*Ph_exp_Ortho)+1i*imag(rs);

%% MW phase correction
Ph_corr=-60;
Ph_exp=exp(1i*Ph_corr/180*pi);
rs_phc=(rs_corr_Ortho*Ph_exp);

%% Other parameters
start_fp=cf-sw/2-rs_width*0.8/2; % start field position
end_fp=cf+sw/2+rs_width*0.8/2;
Nc=round(1/(tb*sf)); % number of points per cycle
NC_hc=round(Nc/2); % number of points per half cycle
first_p=146+NC_hc; % first point of the cycle
rs_width_per_ti=rs_width/NC_hc; % rs scan width per point
nop_left=round(NC_hc*0.1);
nop_right=round(NC_hc*0.9);
rs_phc_im=imag(rs_phc); % only use the data in imag channel
rs_phc_im_hc=rs_phc_im(first_p:first_p+NC_hc,:);

%% Multiple cycles combination / up and down scan
combination
for k=2:floor((t(end)/1e9)/(1/sf))
    rs_phc_im_hc=rs_phc_im_hc+rs_phc_im((first_p+(k-
1)*Nc):(first_p+NC_hc+(k-1)*Nc),:);
end;
for k=1:floor((t(end)/1e9)/(1/sf))
    rs_phc_im_hc=rs_phc_im_hc+flipud(rs_phc_im((first_p+(k-
1)*Nc-NC_hc):(first_p+(k-1)*Nc),:));
```

```
end;
a=rs_phc_im_hc(nop_left:nop_right,1);
rs_cor(:,1)=a;
shift_p=round(step_wise/rs_width_per_ti);

%% Spectral reconstruction
for k=2:length(B0) % Baseline correction with linear
regression
     b=rs_phc_im_hc(nop_left:nop_right,k);
    sq=0;
    for m=shift_p+1:(length(b))
        sq=(a(m)-b(m-shift_p))+sq;
    end;
    dif(:,k)=sq/(length(b)-shift_p);
    b=b+dif(:,k);
    a=b;
    rs_cor(:,k)=b;
end

rs_cor_zero=zeros((length(B0)-
1)*shift_p+length(b),length(B0)); % create zeros matrix for
data averaging

for k=1:length(B0) % Data reconstruction with linear
regression
    bb=rs_cor(:,k);
    startP=(shift_p+1)*(k-1)+1;
    rs_cor_zero(startP:length(bb)+startP-1,k)=bb;
end

for k=1:length(rs_cor_zero) % data averaging
```

```
sum_rs(k,:)=sum(rs_cor_zero(k,:))/length(nonzeros(rs_cor_ze
ro(k,:)));
end

B0_sum=start_fp:(end_fp-start_fp)/(length(sum_rs)-
1):end_fp;
num_ave=round(field_res/((B0_sum(end)-
B0_sum(1))/length(B0_sum)));

for k=1:((B0_sum(end)-B0_sum(1))/field_res) % filtering
    B0_sum_ave(k)=mean(B0_sum((1+num_ave*(k-
1)):(num_ave++num_ave*(k-1))));
    sum_rs_ave(k)=mean(sum_rs((1+num_ave*(k-
1)):(num_ave++num_ave*(k-1))));
end;

%% Filter for first derivative spectrum
x=xForInterp(B0_sum_ave(end-1)-
B0_sum_ave(1),length(gradient(sum_rs_ave)));
filterH=mygaussian(x,sH/1000); % Gaussian filter
filtered_first_deriv=conv(gradient(sum_rs_ave),filterH,'sam
e');

%% CW
x=xForInterp(h_cw(end)-h_cw(1),length(spc_cw));
filterH=mygaussian(x,sH/1000); % Gaussian filter
spc_cw_fil=conv(spc_cw,filterH,'same');

%% Background removal
% n=B0_sum_ave;
```

```
% y=sum_rs_ave;
% [z,a,it,ord,s,fct] = backcor(n,y,1,0.005,'atq');
%
% if ~isempty(z),
%     % Sort the data
%     [n,i] = sort(n);
%     y = y(i);
%
%     z = z(i);
%
%     % Plot the results
%     figure;
%     subplot(2,1,1);
%     plot(n,y,'b',n,z,'r');
%     xlabel('n');
%     legend('Simulated spectrum','Background estimation');
%     title(['Estimation with function ''' fct ''', order =
' num2str(ord) ' and threshold = ' num2str(s)]);
%     subplot(2,1,2);
%     plot(n,y'-z,'r');
%     rs_ave_final=y'-z;
%     rs_ave_final=rs_ave_final/max(rs_ave_final);
%     xlabel('n');
%     legend('Estimated corrected spectrum');
% end;
% break

%% Plot spectra
subplot(3,1,1);
plot(B0_sum_ave,sum_rs_ave,'linewidth',2);
axis tight;
```

```
xlabel('Magnetic field / Gauss');
title('Stepwise RS spectrum of Mn in CaO');

subplot(3,1,2);
plot(B0_sum_ave,filtered_first_deriv/max(filtered_first_der
iv),h_cw-0.3,spc_cw_fil/max(spc_cw_fil),'linewidth',2);
axis tight;
xlabel('Magnetic field / Gauss');
title('First derivative spectrum of stepwise RS spectrum of
Mn in CaO');
rs_fil_deriv=filtered_first_deriv'/max(filtered_first_deriv
);
cw_deriv=spc_cw_fil/max(spc_cw_fil);
h_cw=h_cw-0.3;

subplot(3,1,3);
plot(h_cw,spc_cw/max(spc_cw),'linewidth',2);
axis tight;
xlabel('Magnetic field / Gauss');
title('CW spectrum of stepwise RS spectrum of Mn in CaO');
```

Appendix B: MATLAB Program for Digital Rapid Scan EPR

1. An example of MATLAB program in data analysis of BDPA obtained by digital rapid scan

```
clc;
clear all;

clock=24.135575e9;
ppc_SF = 579930;
ppc_IF = 4639440;
ppc_EC =  120;
ph_corr=110;
ph_corr1=ph_corr;

Nc=8;

sampling_rate=clock/ppc_EC/2;
IF=clock/ppc_IF;
dt=1/sampling_rate;

Np=ppc_IF/ppc_EC;

%% Read data
[x Y p]=eprload('061114/jy111763');

x1=x{1};
t=(0:(length(x1)-1))*dt;
cf=x{2}(2);

Period=1/IF;
Np=round(Period/t(2))

%% BG out
bg1=Y(:,1);
k=2;
rs=Y(:,k);
rs=rs-bg1;
plot(t,rs);

%% Full IF cycle
in=1:Np;
rs=rs(in+0);
t=t(in);
subplot(1,1,1);
```

```
t0=t;
rs0=rs;
plot(t,rs);
rs_fig=rs;
t_fig=t;

%%   Anti-HPF-filter
% read table
T=load('HPF_for_Matlab_headless.txt','-ascii');
v=T(:,1);
I=T(:,2);
[vv jn]=sort([-v; v]);
plot(vv,jn)
ph=T(:,3)/180*pi;
pph=[ph; -ph];
II=[I; I];
II=II(jn);
Ph=pph(jn);
plot(vv,Ph);

%% interpolation
[v_rs RS]=fftM(t,rs);

Ph_i=interp1(vv,Ph,v_rs);
Ph_i(isnan(Ph_i))=0;
FR_i=exp(1i*Ph_i); % freq response
RS_i=RS.*transpose(FR_i);
[t1 rs_i]=ifftM(v_rs,RS_i);
plot(t1,rs_i);

%% Fourier Analysis
[A in0]=min(abs(v_rs)); % index for zeros frequency
a=(Nc-1);
b=(Nc+1);
v_minus=v_rs(in0+a:8:end);
RS_minus=RS_i(in0+a:8:end);
v_plus=v_rs(in0+b:8:end);
RS_plus=RS_i(in0+b:8:end);
subplot(2,1,1);
plot(v_rs/1e3,abs(RS_i),'-
x',v_minus/1e3,abs(RS_minus),'o',v_plus/1e3,abs(RS_plus),'d
');
xlim(0.1*[-0.01 1]*1e3)

dv=v_plus(2)-v_plus(1);
v_0=-v_plus(1)+dv;
```

```
RS_minus=transpose(RS_minus);
RS_plus=transpose(RS_plus);

v_=[fliplr(-v_minus) v_0  v_plus];
RS_=[conj(fliplr(RS_minus))*exp(1i*ph_corr/180*pi) 0
RS_plus*exp(1i*ph_corr1/180*pi)];
subplot(2,1,2);
plot(v_/1e3,abs(RS_),'-x');
xlim(3*[-1 1]*1e3)
grid

% in time-domain
[t_ rs_]=ifftM(v_,RS_);
rs_=rs_.*exp(-1i*2*pi*v_0*t_);  % IF corrections
pltc(rs_);
rs_=smooth(rs_,4);

subplot(2,1,1);
set(gca,'FontSize',16)
plot(t0,real(rs0),'linewidth',2); axis tight;
xlabel 'Time, s'
title ' IF RS signal'

subplot(2,1,2);
set(gca,'FontSize',16)
plot(t_,real(rs_),t_,imag(rs_),'linewidth',2); axis tight;
xlabel 'Time, s'
title 'HPF Phase correction & IF digital quadrature
detection'

%% Parameter
t_=t_+abs(t_(1));
tb=abs(t_(2)-t(1));
gamma=1.7608e7;
up=-1;
Fm=IF*8;
Hm=37.7*0.261;
Nc=length(rs_);
fp=0.018;
rs_=zeroLine(rs_,0.05);

%% first point
shift=round(fp*Nc);   % Circular shift to find 1st point
t=(0:(length(rs_)-1))*tb;                          % Time
vector
rs=circshift(rs_',shift)';
```

```
plot(t,imag(rs),t,real(rs));

%%
[v RS]=fftM(t,rs);

if up>0
    in=v>0;
    a=ifft(ifftshift(RS.*in)); % up scan
    pltc(a);
    jn=v<0;
    b=ifft(ifftshift(RS.*jn)); % up scan
    aa=a(1:Nc/2);
    bb=b(Nc/2+1:Nc);
    bga=a(Nc/2+1:Nc);
    bgb=b(1:Nc/2);
else
    in=v<0;
    a=ifft(ifftshift(RS.*in)); % up scan
    jn=v>0;
    b=ifft(ifftshift(RS.*jn)); % up scan
    aa=a(1:Nc/2);
    bb=b(Nc/2+1:Nc);
    bga=a(Nc/2+1:Nc);
    bgb=b(1:Nc/2);
end
t1=t(1:Nc/2);
t2=t(Nc/2+1:Nc);
subplot(2,1,1)
pltc(aa);
subplot(2,1,2)
pltc(bb)

%% Driving function
WF=-up*cos(2*pi*Fm*t_);
W=gamma*Hm/2*WF;              % waverform
dr=exp(-1i*cumsum(W)*tb); % driving function for 1 cycle
plot(t_,WF);
aaa=aa;
bbb=bb;
fwhm=1.2;
show=1;
%% Deco for A
drA=dr(1:Nc/2);
pltc(drA);

aaaa=aaa.*drA;
```

```
[v A]=fftM(t,aaaa);
[v D]=fftM(t,drA);
subplot(2,1,1)
pltc(A);
subplot(2,1,2)
pltc(D);
A=A./(D);
pltc(A)

%% Deco for B
drB=dr(Nc/2+1:Nc);
bbbb=bbb.*drB;
[v B]=fftM(t,bbbb);
[v D]=fftM(t,drB);
B=B./(D);
h=v*2*pi/gamma;
in=abs(h)<Hm/2;
A=A(in);
B=B(in);
h=h(in);

pltc(A);

%% Post -filtering
filter=mygaussian(h,0.05*fwhm);
sm=sum(filter);
if sm>0
    filter=filter/sum(filter);
    A=conv(A,filter,'same');
    B=conv(B,filter,'same');
else
    disp('Gausian post-filter is ignored')
end

plot(h,A,h,B)

A=zeroLine(A,0.05);
B=zeroLine(B,0.05);
plot(h,A,h,B)

%% Show Figures
if show
    subplot(3,1,2);
    set(gca,'FontSize',16);
    rss=rs_;
    tt=(1:length(rss))*tb;
```

```
    plot(tt*1E6,real(rss),tt*1E6,imag(rss));
    tt_t=tt'*1e6;
    real_rss=real(rss)';
    imag_rss=imag(rss)';
    xlabel 'Time, us'
    axis tight;
    title('reconstruction')

    subplot(3,1,3)
    set(gca,'FontSize',16);
    plot(h,A,h,B,h,A-B); %hold on;
    plot(h,(A+B))
    h=h';
    AA_BB=real(A+B)';
    axis tight;
    xlabel 'Magnetic Field, G'
    title 'RS absorption spectrum '

    subplot(3,1,1)
    set(gca,'FontSize',16);
    plot(t_fig*1e6,rs_fig);
    t_figg=t_fig'*1e6;
    axis tight
    xlabel 'Time, us'
    title 'Raw data'
end
```

2. An example of MATLAB program for excitation and reference waveform in digital rapid scan

```
clc; clear all;
% Create Sinusoid
res_freq  = 9.65e9;        % resonance frequncy
ext_clock = 200e6;
ppc_clock = 2.5;       % points per cycle for major clock ;
Scan_Freq = 41600;
Nc=8;
IF=Scan_Freq/Nc;
clock=res_freq*ppc_clock;          %
dt=1/clock;

K=round(clock/ext_clock/2)*2   % ratio
ext_clock=clock/K
%%
Np=round((1/IF)/(1/clock)/K)*K        % N of total points
```

```
Period=Np*dt;
IF=1/Period
Scan_Freq=Nc*IF

ppc_SF=round(clock/Scan_Freq);     % points per cycle for
scan freq
ppc_IF=Nc*ppc_SF;
ppc_EC=K
disp(ext_clock/1e6)
Np_SJ=round(ext_clock/IF)
%%
clc
ppc_SF     % points per cycle for scan freq
ppc_IF     %  points  per cycle IF
ppc_EC     % Ext clock

%% Exctiation Waveform
x=(0:(Np-1));
WF_wm=2*pi/ppc_clock;
WF_excitation=sin(WF_wm*x+180/180*pi);
plot(x,WF_excitation,'-o');
xlim([0  100]);

%% Scan Freq waveform
T=zeros(2*Np/ppc_SF, ppc_SF/2);
T(1:2:end,:)=1;
T=T';
WF_ScanFreq=T(:);
plot(x,WF_ScanFreq)

%% Ext clock
T=zeros(2*Np/ppc_EC, ppc_EC/2);
T(1:2:end,:)=1;
T=T';
WF_ExtClock=T(:);
plot(x,WF_ExtClock,'-o',x,WF_excitation); xlim([-1  323]);

%%  REF
WF_ref=WF_wm*(1-IF/res_freq);
WF_ref=WF_wm; % RF-IF
WF_ref=sin(WF_ref*x);

%% Trigger
Trigger=WF_ref*0;
Ntr=round(10e-6/dt);
Trigger(1:Ntr)=1;
```

```
plot(x, Trigger);

%% Create Waveform 1 (Double)

Waveform_Name_1 = 'ppc=2.5 ppc DC';
Waveform_Data_1 = WF_excitation; %already a double array
Waveform_M1_1 = uint8(Trigger); %already uint8 array
Waveform_M2_1 = uint8(WF_ExtClock);

Waveform_Name_2 = 'ref for 2.5 ppc DC 180 degree off';
Waveform_Data_2 = WF_ref; %already a double array
Waveform_M1_2 = uint8(Trigger); %already uint8 array
Waveform_M2_2 = uint8(WF_ScanFreq);
save('X band 2x5 ppc DC 6_16_2014', 'Wave*', '-v7.3'); %
MAT 7.3 Can save > 2GB
```

Appendix C: MATLAB Program for Digital Saturation Recovery EPR

1. MATLAB program for excitation waveform in AWG for digital saturation recovery spectrometer

```
clc; clear all;
% Create Sinusoid
res_freq  = 9.65e9;        % resonance frequncy
ext_clock = 200e6;
ppc_clock = 2.5;                  % points per cycle for
major clock ;
clock=res_freq*ppc_clock

dt=1/clock;

K=round(clock/ext_clock/2)*2   % ratio
ext_clock=clock/K
%%
t_pump=2e-6;
Np=round(t_pump/(1/clock))
if mod(Np,5)==0
    display('good to go');
else
    display('change t_pump');
end

%% Exctiation Waveform
x=(0:(Np-1));
WF_wm=2*pi/ppc_clock;
WF_excitation=0.5*sin(WF_wm*x);
plot(x,WF_excitation,'-o');
xlim([0  100]);
marker_1=WF_excitation*0;
marker_1(1:length(marker_1))=1;
marker_0=WF_excitation*0;

%%  REF
WF_ref_wm=WF_wm;
WF_ref=sin(WF_ref_wm*x);
plot(x,WF_ref);

Waveform_Name_1 = 'pump_waveform_070615';
Waveform_Data_1 = WF_excitation; %already a double array
```

```
Waveform_M1_1 = uint8(marker_0); %already uint8 array
Waveform_M2_1 = uint8(marker_1);

Waveform_Name_2 = 'ref pump_waveform_070615';
Waveform_Data_2 = WF_ref; %already a double array

save('X band pump_waveform_070615', 'Wave*', '-v7.3'); %
MAT 7.3 Can save > 2GB
```

2. MATLAB program for observation waveform in AWG for digital saturation recovery spectrometer

```
clc; clear all;
% Create Sinusoid
res_freq  = 9.65e9;        % resonance frequncy
ext_clock = 200e6;
ppc_clock = 2.5;       % points per cycle for major clock ;
clock=res_freq*ppc_clock
dt=1/clock;
K=round(clock/ext_clock/2)*2   % ratio
ext_clock=clock/K

%% time
t_pump=2000e-6;
Np=round(t_pump/(1/clock))
if mod(Np,5)==0
    display('good to go');
else
    display('change t_pump');
end

%% Exctiation Waveform
x=(0:(Np-1));
WF_wm=2*pi/ppc_clock;
WF_excitation=sin(WF_wm*x);
plot(x,WF_excitation,'-o');
xlim([0  100]);
marker_1=WF_excitation*0;
marker_1(1:length(marker_1))=1;
marker_0=WF_excitation*0;

%%  REF
WF_ref_wm=WF_wm;
```

```
WF_ref=sin(WF_ref_wm*x);
plot(x,WF_ref);

%% Trigger
Trigger=WF_ref*0;
Ntr=round(10e-6/dt);
Trigger(1:Ntr)=1;
plot(x, Trigger);

%% Create Waveform 1 (Double)

Waveform_Name_1 = 'observe_waveform_070615_weak';
Waveform_Data_1 = WF_excitation; %already a double array
Waveform_M1_1 = uint8(marker_1); %already uint8 array
Waveform_M2_1 = uint8(marker_0);

Waveform_Name_2 = 'ref observe_waveform_070615_weak';
Waveform_Data_2 = WF_ref; %already a double array
Waveform_M1_2 = uint8(Trigger); %already uint8 array

save('X band observe_waveform_070615_weak', 'Wave*', '-
v7.3'); % MAT 7.3 Can save > 2GB
```

3. MATLAB program for tuning waveform in AWG for digital saturation recovery spectrometer

```
clc; clear all;
% Create Sinusoid
fs=25e9;      % Max Sampling rate
f1=10e9;      % Carrier freq
df=5e6;
f2=f1-df;

ppc=fs/f1;    % Points per cycle
Nc=1000000;      % Number of cycles
Np = Nc*ppc   % Number of points
Nc2=Nc*f2/f1

i=0:(Np-1);
dt=1/fs;      % time increment
t=i*dt;      % time vector
length(t)
F_scan=20900;
AWG_Period=t(end)*1e6   % ms
```

```
Scan_Period=1/F_scan*1e6;
N_of_cycles=AWG_Period/Scan_Period
tb=4e-3 % SpecJetII
SJ_Period=65000*tb

%% Waveform
N_mrk=round(2e-6/dt)
WF1 = sin(2*pi*f1*t); % Generate Sine Wave
WF2 = sin(2*pi*f2*t); % Generate Sine Wave
marker1=WF1*0;
marker1(1:length(marker1))=1;
marker2=WF1*0;
marker3=WF1*0;
marker3(1:N_mrk)=1;
plot(t,WF1,t,WF2,t,marker1,t,marker2)

%% Check
[v Y]=fftM(t,WF1);
plot(v,abs(Y))
xlim([7 11]*1e9)
a=1e12;
f_start=9.61e9;
chirp=sin(2*pi*f_start*t+2*pi*a*t.^2/2);
chirp(Np-Np/16:Np)=0;
chirp(1:Np/16)=0;
plot(chirp)

chirp_ref=sin(2*pi*f_start*t);
[v Y]=fftM(t,chirp);
[v Yr]=fftM(t,chirp_ref);
plot(v,abs(Y),v,abs(Yr)/100,'linewidth',3)
xlim([9.6 9.7]*1e9)

%% Create CW Waveform
Waveform_Name_3 = 'chirp 9.61-9.71 GHz_OPL';
Waveform_Data_3 = chirp; %already a double array
Waveform_M1_3 = uint8(marker1); %already uint8 array
Waveform_M2_3 = uint8(marker2);

Waveform_Name_4 = 'chirp ref 9.61GHz_OPL';
Waveform_Data_4 = chirp_ref; %already a double array
Waveform_M1_4 = uint8(marker3); %already uint8 array
Waveform_M2_4 = uint8(marker3);

save('Xband_CW_500T_chirp_OPL', 'Wave*', '-v7.3'); % MAT
7.3 Can save > 2GB
```

Appendix D: List of Publications

1. **Zhelin Yu**, Richard W. Quine, George A. Rinard, Mark Tseitlin, Hanan Elajaili, Velavan Kathirvelu, Laura J. Clouston, Przemysław J. Boratyński, Andrzej Rajca, Richard Stein, Hassane Mchaourab, Sandra S. Eaton, and Gareth R. Eaton, Rapid-Scan EPR of Immobilized Nitroxides, *Journal of Magnetic Resonance*, 247, (2014), 67-71.

2. Mark Tseitlin,* **Zhelin Yu**,* Richard W. Quine, George A. Rinard, Sandra S. Eaton, and Gareth R. Eaton, Digitally generated excitation and near-baseband quadrature detection of rapid scan EPR signals, *Journal of Magnetic Resonance*, 249, (2014), 126-134.

3. **Zhelin Yu**,* Mark Tseytlin,* Sandra S. Eaton, and Gareth R. Eaton. Multiharmonic Electron Paramagnetic Resonance for Extended Samples with both Narrow and Broad Lines, *Journal of Magnetic Resonance*, 254, (2015), 86-92.

4. Joshua R. Biller, Mark Tseitlin, Deborah G. Mitchell, **Zhelin Yu**, Laura A. Buchanan, Hanan Elajaili, Gerald M. Rosen, Joseph P. Y. Kao, Sandra S. Eaton, and Gareth R. Eaton, Improved Sensitivity for Imaging Spin Trapped Hydroxyl Radical at 250 MHz, *ChemPhysChem,* 16, (2015), 528-531.

5. **Zhelin Yu,** Alexander Romanyukha, Sandra S. Eaton, and Gareth R. Eaton, X-band Rapid Scan ElectronParamagnetic Resonance of Radiation Induced Defects in Tooth Enamel, *Radiation Research,* 184, (2015), in press.

6. **Zhelin Yu,** Tengzhi Liu, Hanan Elajaili, George A. Rinard, Sandra S. Eaton, and Gareth R. Eaton, Field-Stepped Direct Detection Electron Paramagnetic Resonance, *Journal of Magnetic Resonance*, accepted for publication.

7. Hanan Elajaili, George A. Rinard, **Zhelin Yu**, Deborah Mitchell, Richard W. Quine, Sandra S. Eaton, and Gareth R. Eaton, Spin Coherence Signals in X-Band Rapid-Scan EPR of Semiquinones, *Journal of Magnetic Resonance*, under review.

* Two authors contributed equally